

Bayerische Julius-Maximilians-Universität Würzburg
Fakultät für Physik und Astronomie



Master Thesis

Phenomenology of the *Three Site Higgsless Model* at the ATLAS detector of the LHC

Fabian Bach

Oktober 2009

Gutachter: Prof. Dr. Thorsten Ohl
Prof. Dr. Thomas Trefzger

Abstract

Im sogenannten „Three Site Higgsless Model“ [1], das eine Erweiterung des Standardmodells darstellt, wird die elektroschwache Symmetrie nicht durch ein fundamentales Skalarfeld wie das Higgsfeld, sondern durch eine erweiterte elektroschwache Eichgruppe $SU(2) \times SU(2) \times U(1)$ im Sinne einer kompaktifizierten und auf drei *Sites* dekonstruierten fünften Raumzeitdimension gebrochen. Das Teilchenspektrum wird dadurch um drei schwere Eichbosonen W'^{\pm} und Z'^0 mit Massen zwischen 380 und 600 GeV sowie schwere Fermionen mit einer Massenskala von $\gtrsim 3$ TeV erweitert.

In dieser Arbeit wird durch eine analytische Rechnung gezeigt, dass sich die Unitaritätsgrenze der elastischen Streuung longitudinal polarisierter Eichbosonen durch die Beiträge der neuen Eichbosonen von ~ 1 TeV im higgslosen Standardmodell bis auf 2 TeV verschiebt.

Weiterhin wird in einer Detektorstudie die Möglichkeit der Entdeckung der neuen Eichbosonen am ATLAS-Detektor [2, 3, 4, 5] des LHC durch Produktion im s -Kanal und anschließenden Zerfall in Standardmodell-Eichbosonen [6] quantitativ untersucht. Dazu wurden 100 fb^{-1} an Signal und Untergrund für die semileptonischen Kanäle $W'/Z' \rightarrow \nu jj$ und $W' \rightarrow lljj$ sowie den rein leptonischen Kanal $W' \rightarrow \nu ll$ ($l = e, \mu$ und $j = \text{Hadronen-Jet}$) mit dem Monte Carlo-Generator WHIZARD (Version 1.92) [7] generiert und mit der Detektorsimulation ATLFAST-2 [8, 9, 10] der ATLAS-Software ATHENA (Release 14.5.0) [10] simuliert, um die zu erwartenden Signifikanzen abzuschätzen. Die niedrigsten 5σ -Entdeckungsschwellen liegen bei 5–20 fb^{-1} im νjj -Kanal für das Z' und 70–100 fb^{-1} im νll -Kanal für das vergleichsweise schwach koppelnde W' . Für die Trennung des W' -Signals vom Z' -Signal im νjj -Kanal wird eine statistische Methode zur Unterscheidung der Standardmodell-Eichbosonen in den Jet-Resonanzen untersucht [6].

Contents

Introduction	6
1 Unitarity Bounds in the Standard Model	9
1.1 Partial Wave Unitarity in Spontaneously Broken Gauge Symmetries	9
1.1.1 Scattering Theory and Partial Wave Expansion	9
1.1.2 Longitudinal Polarization	10
1.2 Self-coupling of Non-Abelian Gauge Bosons	12
1.3 Elastic Scattering of Longitudinal Gauge Bosons	13
1.3.1 Contact Diagram	14
1.3.2 s Channel Diagram	16
1.3.3 t and u Channels	18
1.3.4 Propagator Expansion and Leading-order Result	20
1.3.5 Basis Transformations	22
Mass and Charge	22
Custodial Isospin	25
1.3.6 Partial Wave Expansion	28
1.3.7 Higgs Scenario	29
1.4 Top Pair Annihilation into Gauge Bosons	31
1.4.1 Chiral States	32
1.4.2 Helicity States	35
2 The Three Site Higgsless Model	37
2.1 Construction	37
2.1.1 Chiral Lagrangian	37
2.1.2 Three Site Higgsless Model	39
2.2 Particle Spectrum and Mass Basis	40
2.2.1 Gauge Bosons	40
2.2.2 Fermions	44
2.3 Constraints on Parameter Space	45
2.3.1 Theoretical Bounds from Unitarity Violation	45
Scattering Amplitudes in the 3SHLM	45
Leading-order Cancellations	48
Partial Wave Expansion	51
2.3.2 Experimental Bounds	54
3 Experiment and Simulation	59
3.1 The ATLAS Detector	59
3.1.1 Coordinate System	59

3.1.2	Inner Detector	60
3.1.3	Calorimeters	61
3.1.4	Muon Spectrometer	62
3.2	The Data Simulation Chain	64
3.2.1	Production of Monte Carlo Events	64
	Final State Signatures	66
	Signal	67
	Backgrounds	69
3.2.2	Parton Shower and Fragmentation	71
3.2.3	Detector Simulation	72
3.2.4	Comparison with Validated Data	74
4	Search for Heavy Gauge Bosons	78
4.1	Final State Reconstruction	78
4.1.1	Muons	78
4.1.2	Electrons	81
4.1.3	Hadron Jets	83
	Jet-Finding Procedure	83
	Performance of Jet Algorithms and Inputs	85
	Rejection of Electron Jets	86
4.1.4	Neutrinos	87
	Basic Idea	87
	Reconstructed 4-Momenta	89
4.2	$l\nu jj$ Channel	93
4.2.1	Basic Analysis	93
4.2.2	Systematic Uncertainties	98
4.2.3	Disentanglement of Jet Resonances	100
4.3	$lljj$ Channel	104
4.4	$l\nu ll$ Channel	107
4.5	Significances and Discovery Thresholds	109
	Ideal Delocalization	109
	Almost Fermiophobic W'	110
	Conclusions	112
	References	114
	List of Figures	117
	Appendix	123

A	4-Momentum Conventions	123
B	Contractions of Longitudinal Polarization Vectors	124
	B.1 $W^{1/2}$ Scattering	124
	B.2 External Z^0 Bosons	126
C	Comparison of ATLFAST-2 and Full Simulation	127
	C.1 Jet Variables	127
	C.2 Electron Variables	129

Introduction

One of the best probed and most successful theories in physics, *Quantum Electrodynamics* (QED), was developed in the 1940s by Richard P. FEYNMAN and others. It describes all electromagnetic interactions among elementary particles through quantum fields which are coupled to each other by an exact local symmetry under phase transformations $U(1)_{em}$. In order to take also weak processes like the neutron decay into account, the so-called Fermi interaction, based on the work of Enrico FERMI in 1934 [11], was introduced as a four-fermion operator with a dimensionful coupling constant, the Fermi constant G_F . Because of this property of the coupling constant, the operator is non-renormalizable and violates partial wave unitarity at ~ 600 GeV. In the context of an effective field theory, however, this operator can be understood as an effective low-energy interaction of new, yet undiscovered physics at some higher energy scale. In this sense, generalizing the originally imposed gauge principle, the electromagnetic and weak interactions can be unified under a more complex local symmetry group. This symmetry, however, must be broken again to the exact $U(1)_{em}$ in order to give masses to all gauge bosons except for the photon, thus eliminating them from the low-energy spectrum of the theory. This also makes their interactions appear point-like at low energies, giving rise to the Fermi operator.

As a minimal extension, Sheldon L. GLASHOW proposed in 1961 a $SU(2)$ symmetry whose unbroken T_3 generator embeds the $U(1)_{em}$, whereas the two remaining broken generators lead to heavy, charged gauge bosons W^\pm , responsible for the charged currents of the weak interaction [12]. However, the discoveries of the neutral-current interactions in 1973 at the Gargamelle experiment at CERN [13] and eventually of the Z^0 resonance itself in 1983 at the UA1-Experiment of the SPS collider at CERN [14] obviously correspond to the necessity of an even larger symmetry group: The $SU(2)_L \times U(1)_Y$, already proposed independently by Steven WEINBERG [15] in 1967 and Abdus SALAM [16] in 1968, comprises an additional heavy, neutral gauge boson, hence providing the minimal experimentally solid extension of QED. Furthermore, the unitarity bound is shifted up to 1.2 GeV due to contributions of the heavy gauge bosons. Within the formalism of the so-called Glashow-Weinberg-Salam (GWS) theory, this symmetry group forms the electroweak gauge sector of the *Standard Model of Particle Physics* (SM), which has been a very powerful formalism for predicting and explaining the most different experimental results for more than three decades now.

Regardless of the success of this theory, there is so far no experimental evidence for the actual mechanism of electroweak symmetry breaking. Another problem of spontaneously broken gauge symmetries is the unitarity violation

in elastic scattering amplitudes of the longitudinal modes of heavy gauge bosons at high energies, becoming manifest in the *Low Energy Theorem* of pion- und Goldstone boson scattering [17, 18] as soon as the *Goldstone boson equivalence theorem* [18, 19, 20], relating Goldstone bosons to longitudinal gauge bosons at high energies, is applied. All extensions of the experimentally confirmed sectors of the SM should not only contain a mechanism for symmetry breaking but also address the inherent unitarity problem.

The introduction of a fundamental scalar field as in the Higgs mechanism [21, 22] of the GWS theory fulfills these requirements [23, 24], but comes along with other drawbacks like e. g. the quadratic dependence of the Higgs mass on the renormalization scale. Other approaches are, for example, the Technicolor models [25, 26] with an additional strongly interacting sector, whose meson-like bound states play the role of the symmetry-breaking scalars, or models with one or more additional space-time dimensions compactified on the electroweak length scale, where symmetry breaking can be implemented by non-trivial ground state configurations of the additional gauge field components. Indeed, in the case of exactly five dimensions (5D) with the geometry of a 5D Anti-de Sitter space [27], these different types of models turn out to be related to each other by a duality commonly addressed as AdS/CFT correspondence [28]. Without stressing this point any further, the *Three Site Higgsless Model* (3SHLM) introduced by R. S. CHIVUKULA et al. in 2006 [1] can be counted among this class of theories as a maximally deconstructed limit, with its extra dimension discretized on three sites only. In any case, the *Large Hadron Collider* (LHC) at CERN, as a proton-proton collider with center-of-mass energies up to 14 TeV, is designed to reach the scale of electroweak symmetry breaking in hard parton scattering processes, thus probing the underlying dynamics at the two large multi-purpose experiments ATLAS [2, 3, 4, 5] and CMS [29].

This thesis is dedicated to several phenomenological aspects of the 3SHLM: In a theoretical approach, after reviewing the SM scenario of the violation of partial wave unitarity in scattering processes involving longitudinally polarized gauge bosons, the additional contributions of the new heavy gauge bosons of the 3SHLM are calculated analytically, thus showing that the unitarity-violating energy scale is shifted from ~ 1 TeV in the higgsless SM to $\lesssim 2$ TeV in the 3SHLM. In an experimental context, a detector study of the ATLAS detector is performed in order to quantify the discovery potential of the new heavy gauge bosons via s channel production. To that end, signal and background events of the relevant final states $l\nu jj$, $lljj$ [6] and $l\nu ll$ were generated in samples corresponding to an integrated luminosity of 100 fb^{-1} using the Monte Carlo event generator WHIZARD [7]. After generation on parton level, the samples were hadronised with PYTHIA [30] and

their detector impact simulated with the detector simulation ATLFAST-2 [8, 9, 10] of the ATLAS software framework ATHENA (release 14.5.0) [10]. The simulated data give rise to estimated discovery thresholds of 5–20 fb⁻¹ for the Z' and at the very least 70 fb⁻¹ for the W' , whose coupling to SM fermions is suppressed relative to the Z' , whereas the data analysis features a new statistical method for the discrimination of the SM gauge bosons in di-jet resonances [6].

1 Unitarity Bounds in the Standard Model

1.1 Partial Wave Unitarity in Spontaneously Broken Gauge Symmetries

1.1.1 Scattering Theory and Partial Wave Expansion

In quantum mechanics as well as quantum field theory the initial and final states $|i\rangle$ and $|f\rangle$ of a scattering process, defined as asymptotic states corresponding, respectively, to the limits $t \rightarrow \pm\infty$, are connected by a unitary scattering matrix S ,

$$|f\rangle = S |i\rangle , \quad (1.1)$$

which in quantum field theory is usually evaluated as a perturbation series in the small coupling constants of interactions (cf. [31], ch. 4). Extracting the unit part of S containing no interaction,

$$S \equiv 1 + iT , \quad (1.2)$$

the matrix T defined that way is then expanded, element by element, in the coupling constants of the theory. Choosing momentum eigenstates in Fock space as asymptotic states, the matrix elements of T describing a $2 \rightarrow$ anything scattering process may be further decomposed [31]:

$$\langle \{p_f\} | iT | p_{i1} p_{i2} \rangle = (2\pi)^4 \delta^{(4)}(p_{i1} + p_{i2} - \Sigma p_f) \cdot i\mathcal{M}(p_{i1}, p_{i2} \rightarrow \{p_f\}) , \quad (1.3)$$

where energy and momentum conservation has been extracted. The remaining complex function \mathcal{M} , commonly referred to as Feynman amplitude, depends on all momenta involved and summarizes the dynamics of the theory, i. e. all possible interactions of matter and gauge fields of the theory which contribute to the matrix element specified by the asymptotic states: This is the object to be expanded in powers of the involved coupling constants. In the special case of $2 \rightarrow 2$ scattering considered in the further course of this chapter, \mathcal{M} is a function of the total energy \sqrt{s} in the center-of-mass system (CMS) and the polar scattering angle θ between the incoming and outgoing directions in the said reference frame, or, equivalently, of the Lorentz-invariant Mandelstam variables s , t and u (for the conventions used in this thesis, cf. appendix A).

It is now straightforward to perform a partial wave analysis as usual, using the spherical harmonics as a basis and expanding \mathcal{M} with respect to its partial wave coefficients a_L corresponding to specific angular momentum values L (cf. [32], ch. 3):

$$\mathcal{M}(s, \theta) = 32\pi \sum_L a_L(s) (2L + 1) P_L(\cos \theta) , \quad (1.4)$$

with P_L denoting the Legendre polynomials (rotational symmetry with respect to the azimuth angle assumed). The coefficients a_L are found by projecting onto the P_L :

$$\begin{aligned} a_L(s) &= \frac{1}{32\pi} \int_{-1}^1 d(\cos\theta) \mathcal{M}(s, \theta) P_L(\cos\theta) \\ &= \frac{1}{32\pi} \int_{-s}^0 \frac{dt}{s} \mathcal{M}(s, t, u) P_L\left(1 + 2\frac{t}{s}\right), \end{aligned} \quad (1.5)$$

where in the second line eqn. (A.4) has been used to transform the integration variable. From general scattering theory (e. g. cf. [33], ch. 7 or [32], ch. 3) it is clear that, in order to conserve probability in any elastic scattering process, the amplitudes of every partial wave have to obey the relation

$$|a_L(s) - i/2| = 1/2, \quad (1.6)$$

which particularly implies that the real part of a_L can never exceed $1/2$.

1.1.2 Longitudinal Polarization

When evaluating Feynman amplitudes using the Feynman rules of a theory, the polarization 4-vectors ε^μ of all external vector particles—such as gauge bosons—have to be contracted with other Lorentz tensors in order to make the overall amplitude Lorentz-invariant. However, the only Lorentz tensors usually occurring in the Feynman rules apart from the polarizations themselves are external and internal 4-momenta p_i^μ , and the Dirac matrices γ^μ of the vector currents associated with the gauge symmetries. Hence the only Lorentz contractions potentially occurring in \mathcal{M} are combinations of these three 4-vectors specified by the Feynman rules.

Bearing this in mind, one may look at the physical degrees of freedom of a heavy gauge boson with mass m and momentum $k^\mu = (E, \vec{k})$ so that $k^2 = m^2$ (cf. [31], ch. 21 for the remaining section). In contrast to the massless photon of QED with two purely transverse degrees of freedom, for a massive boson there always exists a rest frame with $k^\mu = (m, \vec{0})$ in which the three remaining orthonormal directions ε_i^μ respecting

$$\varepsilon_i(k) \cdot k = 0 \quad \text{and} \quad \varepsilon_i(k) \cdot \varepsilon_j(k) = -\delta_{ij} \quad \forall i, j = 1, 2, 3 \quad (1.7)$$

are obvious. After boosting the boson along an arbitrary space direction \vec{n} , two of the ε_i^μ may still be chosen transverse to \vec{n} , whereas the remaining third degree of freedom collinear to \vec{n} , denoted *longitudinal polarization* ε_L^μ from

now on, transforms into [19]

$$\varepsilon_L^\mu(k) = \left(\frac{|\vec{k}|}{m}, \frac{E}{m} \vec{n} \right), \quad (1.8)$$

which becomes increasingly collinear with the 4-momentum vector in the limit $E \gg m$,

$$\varepsilon_L^\mu(k) = \frac{k^\mu}{m} + \mathcal{O}\left(\frac{m}{E}\right), \quad (1.9)$$

while still fulfilling, to all orders, the orthonormality requirements (1.7). The *Goldstone boson equivalence theorem* [19, 20] states that, if the gauge boson mass originates from the spontaneous breaking of its corresponding gauge symmetry generator, all scattering amplitudes involving the longitudinal degree of freedom of the gauge boson are equivalent to amplitudes containing the Goldstone boson associated with the broken symmetry at high energies, whereas the underlying Feynman rules generally depend on the chosen gauge. Eqn. (1.9) is but another manifestation of this statement, pointing out that the longitudinal mode of a massive gauge boson increasingly behaves like its associated Goldstone boson, i. e. becomes scalar polarized, when going into the limit $E \gg m$.

Bearing these considerations in mind, it is now clear what are the potentially dangerous terms of the Feynman amplitude in the context of unitarity violation: With two longitudinally polarized gauge bosons in the external states, the worst-case scenario would be a direct contraction of their polarization vectors, giving a leading term according to eqn. (1.9) which grows as

$$\varepsilon_L(p_i) \cdot \varepsilon_L(p_j) \simeq \frac{s}{2m_i m_j} \gg 1 \quad \text{for} \quad \sqrt{s} \gg m_i, m_j, \quad i \neq j \quad (1.10)$$

in the s channel, so that the partial wave amplitudes will finally run into their unitarity limit given by (1.6) at a specific energy scale. Furthermore, since \mathcal{M} is a dimensionless object, the mass dimensions of all occurring external momenta are cancelled by other dimensionful objects, i. e. propagators carrying momenta in the denominator or mass parameters, the latter potentially leading to Lorentz contractions of the form $\varepsilon_L(p_i) \cdot \frac{p_j}{m}$ ($i \neq j$) with the same dangerous high energy behaviour as in eqn. (1.10). All kinematically possible combinations of the two said types of divergent Lorentz contractions with respect to the s , t and u channels are calculated in appendix B and expanded up to the necessary order in powers of the dimensionless large parameter

$$x \equiv \frac{s}{m^2} \gg 1, \quad m \equiv m_W, \quad (1.11)$$

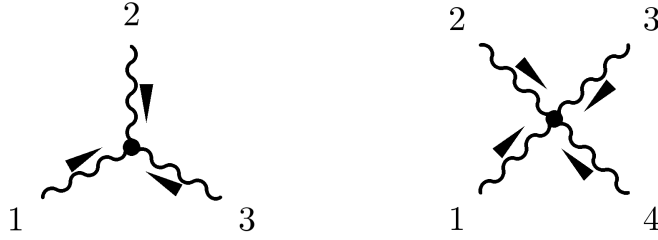


Figure 1: Feynman diagrams for the self-coupling vertices of gauge bosons in non-Abelian gauge theories. The arrows indicate the 4-momentum flows chosen to derive the Feynman rules, and the numbers enumerate all relevant properties of the gauge bosons (4-momentum, Lorentz index and gauge index), as consistent with the conventions pointed out in appendix A.

so that eventually the full amplitudes can be expanded in x and their high energy behaviour examined. In the following sections of this chapter, after a short recapitulation of gauge boson self-couplings in non-Abelian gauge theories, several $2 \rightarrow 2$ scattering processes involving longitudinal gauge bosons which produce contributions of the form (1.10) are discussed explicitly.

1.2 Self-coupling of Non-Abelian Gauge Bosons

In any Yang-Mills theory, it is an inherent feature of the non-Abelian gauge symmetries considered that the associated gauge fields are self-coupled due to those terms of the gauge-invariant field strength tensor which are quadratic in the respective gauge fields A_μ^a (e. g. cf. [31], ch. 15):

$$A_{\mu\nu}^a = \partial_\mu A_\nu^a - \partial_\nu A_\mu^a + gf_{abc}A_\mu^b A_\nu^c, \quad (1.12)$$

where g denotes the gauge coupling of the gauged symmetry group G and f_{abc} denotes the structure constants of its generator algebra: $A_\mu \equiv \vec{A}_\mu \cdot \vec{T}$ with $[T_a, T_b] = -if_{abc}T_c$ and $a, b, c = 1 \cdots d(G)$. Then the self-coupling terms emerge from the invariant contraction of the field strength in the Lagrangian density:

$$\begin{aligned} \mathcal{L}_A &= -\frac{1}{2}\text{tr}[A_{\mu\nu}A^{\mu\nu}] \\ &= -\frac{1}{4}\vec{A}_{\mu\nu} \cdot \vec{A}^{\mu\nu} \quad \text{with} \quad \text{tr}[T_a T_b] = \frac{1}{2}\delta_{ab} \\ &= (\text{kinetic terms}) + \\ &\quad -gf_{abc}(\partial_\mu A_\nu^a)A^{b\mu}A^{c\nu} - \frac{1}{4}g^2 f_{abc}f_{ade}A_\mu^b A_\nu^c A^{d\mu}A^{e\nu}, \end{aligned} \quad (1.13)$$

where the terms in the last line lead to couplings of three and four gauge bosons, respectively.

With the momentum flow and numbering conventions depicted in fig. 1, the Feynman rules for the three-boson and four-boson vertex may now be computed from eqn. (1.13) by summing up all possibilities to assign gauge indices to external momenta and polarizations (e. g., cf. [31], ch. 16): Using the total antisymmetry of the structure constants and replacing the derivatives with corresponding external 4-momentum factors for the chosen momentum flow convention, $\partial^\mu \rightarrow (-ip^\mu)$, the interaction terms in eqn. (1.13) lead to the following Feynman rules:

$$\text{---}\text{---}\text{---} \rightarrow gf_{a_1 a_2 a_3} [g_{\mu_1 \mu_2} (p_1 - p_2)_{\mu_3} + \text{all cyclic permutations}], \quad (1.14)$$

$$\begin{aligned} \text{---}\text{---}\text{---}\text{---} &\rightarrow -ig^2 [f_{a_1 a_2 b} f_{a_3 a_4 b} (g_{\mu_1 \mu_3} g_{\mu_2 \mu_4} - g_{\mu_1 \mu_4} g_{\mu_2 \mu_3}) + \\ &+ (1 \rightarrow 2, 2 \rightarrow 3, 3 \rightarrow 4, 4 \rightarrow 1) + (3 \leftrightarrow 4)]. \quad (1.15) \end{aligned}$$

Note here that all successive permutations occurring in the course of this thesis, such as in eqn. (1.15), must generally be understood as cumulative, i. e. every permutation is to be performed on top of the preceding one. Furthermore, the imaginary unit which was originally defined outside the Feynman amplitude, cf. eqn. (1.3), has been included here in the Feynman rules (1.14) and (1.15). The prefactor $\frac{1}{4}$ of the Lagrangian term for the four-boson vertex in (1.13) cancels against a combinatorial factor coming from four equivalent sets of index assignments within the $4!$ combinations which are possible in total.

The two gauge boson self-coupling vertices, eqns. (1.14) and (1.15), form the basic ingredients for the computation of tree-level Feynman diagrams with external longitudinal gauge bosons in the following sections: In the SM, with the non-Abelian factor $SU(2)_L$ in its gauge group, these vertices result in couplings of the charged W^\pm to the neutral Z^0 containing an admixture of the non-Abelian gauge component W^3 .

1.3 Elastic Scattering of Longitudinal Gauge Bosons

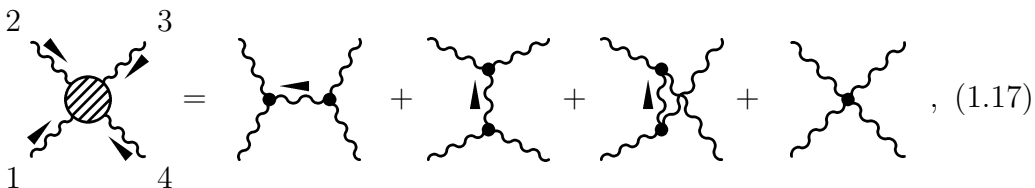
With all the considerations and preparations made in the previous sections, it is now time to compute the Feynman amplitudes of processes which are potentially dangerous for partial wave unitarity, and to investigate their high energy behavior. From eqn. (1.10) and the vertex rules (1.14) and (1.15) of the previous section, it follows that the more longitudinally polarized gauge bosons occur in the asymptotic states, the more dangerous the resulting high energy behavior will be. Restricting oneself to $2 \rightarrow 2$ processes, it is clear

that the elastic scattering of four longitudinally polarized gauge bosons will be the process diverging most rapidly with \sqrt{s} :

$$\mathcal{M}(A_L^{a_1} A_L^{a_2} \rightarrow A_L^{a_3} A_L^{a_4}) \propto [\varepsilon_L(p_1) \cdot \varepsilon_L(p_2)] [\varepsilon_L(p_3) \cdot \varepsilon_L(p_4)] = \frac{1}{4}x^2 + \mathcal{O}(x^1) \quad (1.16)$$

in the s channel, with gauge indices a_i . Therefore this amplitude will now be computed and analyzed in the SM both without and with Higgs.

In the SM without Higgs, all contributions to the amplitude (1.16) stem from the gauge interactions presented in the previous section and can be decomposed diagrammatically as follows:



where the labels follow the usual conventions and the arrows denote external and internal 4-momentum flows. It is indeed an inherent feature of the $SU(2)_L$ gauge symmetry imposed on the SM Lagrangian that the most divergent terms of this amplitude $\propto x^2$ cancel purely through the interplay of the gauge interactions [23, 24]. This will also become obvious below, although the emphasis is rather placed on the next-to-leading order terms $\propto x$, which do not cancel without additional contributions of any new physics and constitute the leading high energy divergence of the partial wave amplitudes. The following computation of all the separate diagrams in eqn. (1.17) is carried out in the interaction basis, i. e. the gauge indices are kept until the very end. The restriction to gauge components $a_i = 1, 2$ further simplifies the procedure, because the only occurring external mass is then m , whereas the case of asymptotic Z^0 will be addressed explicitly in section 1.3.5, on the grounds of the results of sections 1.3.1 – 1.3.4. Note that in the following calculations the moduli of the expressions t/m^2 and u/m^2 are considered to grow $\propto x$ despite their angular dependency, cf. eqn. (A.4): The problem of forward scattering will be addressed separately in the further course of this section.

1.3.1 Contact Diagram

The first and easiest diagram to be evaluated is the contact term in eqn. (1.17), since computation in the interaction basis means that starting from the Feynman rule (1.15) the only remaining task is to contract the Lorentz indices with the longitudinal polarization 4-vectors corresponding to the assigned external 4-momenta, eqn. (1.8), and to expand the resulting expres-

sion in powers of x . The starting point is then

$$\begin{aligned}
\text{Diagram} &= \varepsilon_L^{\mu_1}(p_1)\varepsilon_L^{\mu_2}(p_2)\varepsilon_L^{\mu_3}(p_3)\varepsilon_L^{\mu_4}(p_4) \times \\
&\times (-ig^2) [f_{a_1a_2b}f_{a_3a_4b}(g_{\mu_1\mu_3}g_{\mu_2\mu_4} - g_{\mu_1\mu_4}g_{\mu_2\mu_3}) + \\
&\quad + (1 \rightarrow 2, 2 \rightarrow 3, 3 \rightarrow 4, 4 \rightarrow 1) + (3 \leftrightarrow 4)] . \quad (1.18)
\end{aligned}$$

Writing out explicitly the non-trivial permutation leading to the second term in (1.18) and evaluating all the Lorentz contractions results in

$$\begin{aligned}
(-ig^2) [f_{a_1a_2b}f_{a_3a_4b} ([\varepsilon_L(p_1) \cdot \varepsilon_L(p_3)]^2 - [\varepsilon_L(p_1) \cdot \varepsilon_L(p_4)]^2) + \\
+ f_{a_2a_3b}f_{a_4a_1b} ([\varepsilon_L(p_2) \cdot \varepsilon_L(p_4)]^2 - [\varepsilon_L(p_2) \cdot \varepsilon_L(p_1)]^2) + (3 \leftrightarrow 4)] , \quad (1.19)
\end{aligned}$$

while the permutation leading from the second to the third term merely implies $t \leftrightarrow u$ in the final result. In order to evaluate this expression in terms of the Mandelstam variables, and to extract the first two orders in x , the respective x expansions given in eqns. (B.3) – (B.5) for the different combinations of polarization contractions in (1.19) are now plugged in up to the necessary order $\mathcal{O}(x^0)$. Squaring these contractions and separating $\mathcal{O}(x^2)$ from $\mathcal{O}(x^1)$, one arrives at

$$\begin{aligned}
(-ig^2) [f_{a_1a_2b}f_{a_3a_4b} \left(\frac{1}{4m^4} [u^2 - t^2] + \frac{1}{m^2s} [u^2 - t^2] \right) + \\
+ f_{a_2a_3b}f_{a_4a_1b} \left(\frac{1}{4m^4} [u^2 - s^2] + \frac{1}{m^2s} [u^2 - tu + s^2] \right) + (3 \leftrightarrow 4)] . \quad (1.20)
\end{aligned}$$

In the last step the binomials in (1.20) are factorized, e. g. $(u^2 - t^2) = (u - t)(u + t)$, so that the factor containing the sum can be replaced using eqn. (A.3). Note that in $\mathcal{O}(x^2)$ the identity (A.3) must be used exactly, shifting an additional term into the subleading order, whereas in $\mathcal{O}(x^1)$ the approximation suffices. To leading order, the expression is then already in its final shape, whereas to subleading order, after collecting and subsuming all contributing terms, it turns out that these cancel exactly for the s -type combination of structure constants, $(f_{a_1a_2b}f_{a_3a_4b})$, so that the final result, expanded in powers of x , reads

$$\begin{aligned}
\text{Diagram} &= (-ig^2) \left[f_{a_1a_2b}f_{a_3a_4b} \left(\frac{s(t-u)}{4m^4} + 0 \right) + \right. \\
&\quad + f_{a_2a_3b}f_{a_4a_1b} \left(\frac{t(s-u)}{4m^4} - 2\frac{tu}{m^2s} \right) + \\
&\quad \left. + f_{a_2a_4b}f_{a_3a_1b} \left(\frac{u(s-t)}{4m^4} - 2\frac{tu}{m^2s} \right) \right] . \quad (1.21)
\end{aligned}$$

1.3.2 s Channel Diagram

For the computation of the gauge boson exchange diagrams remaining in eqn. (1.15) the Feynman rule for a non-Abelian gauge boson propagator has to be plugged in. Since the gauge must be fixed to allow for an unambiguous definition of the Feynman path integral for the gauge field, the propagator formally depends on the chosen gauge (cf. [31], ch. 16). However, in a general gauge-fixing scheme some unphysical degrees of freedom—such as the Goldstone bosons emerging from spontaneous symmetry breaking—remain in the particle spectrum (cf. [31], ch. 21). For the purposes pursued here, it is therefore convenient to proceed in *unitarity gauge*, keeping only the physical degrees of freedom, i. e. the three transverse polarizations of massive vector bosons, in the spectrum. In this gauge the propagator reads

$$\frac{-i\delta_{ab}}{k^2 - m_a^2} \left[g^{\mu\nu} - \frac{k^\mu k^\nu}{m_a^2} \right] \quad (1.22)$$

with 4-momentum transfer k and gauge indices a, b . This propagator generically describes the propagation of the transversely polarized gauge component a with mass m_a originating from the spontaneous breaking of its symmetry generator.

The s -channel gauge boson exchange diagram in eqn. (1.17) can now be assembled from the Feynman rules for the three-boson vertex (1.14) and the gauge boson propagator just given in (1.22). As indicated by the arrow in (1.17), the momentum flow convention is chosen as

$$k \equiv -(p_1 + p_2) = p_3 + p_4, \quad (1.23)$$

so that the resulting algebraic expression for the diagram is

$$\begin{aligned} \text{Diagram} &= \varepsilon_L^{\mu_1}(p_1) \varepsilon_L^{\mu_2}(p_2) \varepsilon_L^{\mu_3}(p_3) \varepsilon_L^{\mu_4}(p_4) \times \frac{-i\delta_{bc}}{s - m_b^2} \left[g^{\nu\rho} - \frac{k^\nu k^\rho}{m_b^2} \right] \times \\ &\times g f_{a_1 a_2 b} (g_{\mu_1 \mu_2} [p_1 - p_2]_\nu + g_{\mu_2 \nu} [p_2 - k]_{\mu_1} + g_{\nu \mu_1} [k - p_1]_{\mu_2}) \times \\ &\times (1 \rightarrow 3, 2 \rightarrow 4, k \rightarrow -k, \nu \rightarrow \rho, b \rightarrow c), \end{aligned} \quad (1.24)$$

where the replacements given in the last line produce the correct factor for the second vertex from the respective factor for the first one written out in line two. Now the external polarization contractions can be carried out: Replacing k with external momenta according to (1.23) and minding the

orthogonality condition (1.7), this gives

$$\begin{aligned}
& (-ig^2) f_{a_1 a_2 b} f_{a_3 a_4 b} \times \frac{m^2}{s - m_b^2} \left[g^{\nu\rho} - \frac{(-p_1 - p_2)^\nu (p_3 + p_4)^\rho}{m_b^2} \right] \times \\
& \times \left\{ [\varepsilon_L(p_1) \cdot \varepsilon_L(p_2)] \left[\frac{p_1}{m} - \frac{p_2}{m} \right]_\nu - 2 [\varepsilon_L(p_1) \cdot \frac{p_2}{m}] [\varepsilon_L(p_1) - \varepsilon_L(p_2)]_\nu \right\} \times \\
& \times \left\{ [\varepsilon_L(p_3) \cdot \varepsilon_L(p_4)] \left[\frac{p_3}{m} - \frac{p_4}{m} \right]_\rho - 2 [\varepsilon_L(p_3) \cdot \frac{p_4}{m}] [\varepsilon_L(p_3) - \varepsilon_L(p_4)]_\rho \right\}, \tag{1.25}
\end{aligned}$$

where the entire expression was multiplied by m^2/m^2 to cancel the mass dimensions of the propagator and the external momenta. In this expression it becomes clear that the $k^\nu k^\rho$ part of the Lorentz tensor in the propagator does not contribute: Using orthogonality and mass shell conditions of the external polarizations and momenta, all remaining contractions in (1.25) except for the $g^{\nu\rho}$ part give either zeros or pairs of identical terms with opposite signs. Indeed, this is nothing but a manifestation of the Ward identity in momentum space, which follows from the conservation of gauge currents (cf. [31], ch. 7).

For the next step, some care must be taken concerning the x expansion of the expression: Note that the leading term of the propagator is of $\mathcal{O}(x^{-1})$, whereas the Lorentz contractions still to be carried out via the metric tensor of the propagator give terms of $\mathcal{O}(x^1)$ at most, thus raising the propagator order to give $\mathcal{O}(x^0)$ altogether. For the remaining factors of expr. (1.25), namely the Lorentz contractions which were already carried out, the same logic applies as for the contact term: When replacing them by their x expansions given in eqns. (B.3) and (B.8), it suffices to plug in the terms down to $\mathcal{O}(x^0)$ in order to be accurate to $\mathcal{O}(x^1)$ after squaring. The result of all that is then

$$\begin{aligned}
& (-ig^2) f_{a_1 a_2 b} f_{a_3 a_4 b} \times \frac{m^2}{s - m_b^2} g^{\nu\rho} \times \\
& \times \left(\frac{s}{2m^2} - 1 \right) \left[\left(\frac{p_1}{m} - \varepsilon_L(p_1) \right) - \left(\frac{p_2}{m} - \varepsilon_L(p_2) \right) - \varepsilon_L(p_1) + \varepsilon_L(p_2) \right]_\nu \times \\
& \times \left(\frac{s}{2m^2} - 1 \right) \left[\left(\frac{p_3}{m} - \varepsilon_L(p_3) \right) - \left(\frac{p_4}{m} - \varepsilon_L(p_4) \right) - \varepsilon_L(p_3) + \varepsilon_L(p_4) \right]_\rho, \tag{1.26}
\end{aligned}$$

where the remaining Lorentz vectors have been rearranged in such a way that the cancellation of the momenta by the leading terms of the polarization vectors becomes obvious, cf. eqn. (1.9). Using the results in appendix B again, eqns. (B.4) – (B.5) and (B.12) – (B.13), the remaining Lorentz contractions may now be carried out down to the necessary order $\mathcal{O}(x^0)$,

giving

$$\begin{aligned}
& (-ig^2) f_{a_1 a_2 b} f_{a_3 a_4 b} \times \frac{m^2}{s - m_b^2} \times \\
& \times \left(\frac{s}{2m^2} - 1 \right)^2 \left[2 \left(\frac{u}{2m^2} + \frac{u-t}{s} \right) - 2 \left(\frac{t}{2m^2} + \frac{t-u}{s} \right) - 4 \left(\frac{t}{s} \right) + 4 \left(\frac{u}{s} \right) \right]. \quad (1.27)
\end{aligned}$$

It is now straightforward to subsume all terms and expand the entire second line in powers of x to come to the final result for this diagram, which reads

$$\text{Diagram} = (ig^2) f_{a_1 a_2 b} f_{a_3 a_4 b} \times \frac{s}{s - m_b^2} \times \left[\frac{s(t-u)}{4m^4} + \frac{(t-u)}{m^2} + \mathcal{O}(x^0) \right]. \quad (1.28)$$

Note that the overall sign has changed and that a factor x^{-1} has been extracted from the propagator. Approximating the resulting propagator factor by unity to leading order and comparing this result with the the contact term, eqn. (1.21), the exact gauge cancellation of the highest-order terms $\propto x^2$ is obvious.

1.3.3 t and u Channels

For the computation of the t -channel amplitude the symmetric momentum flow and numbering convention pointed out in appendix A pays off, because now almost the whole job is done by some simple permutations in the s channel amplitude, cf. eqn. (1.17):

$$\text{Diagram} = \left(\text{Diagram} \right) \begin{matrix} \curvearrowright 1 \\ \curvearrowleft 2 \\ \curvearrowright 3 \\ \curvearrowleft 4 \end{matrix}, \quad (1.29)$$

where the permutations refer to all numbers occurring in eqn. (1.24). One may now jump at once to eqn. (1.25) of the s channel and translate it into the t channel:

$$\begin{aligned}
& (-ig^2) f_{a_2 a_3 b} f_{a_4 a_1 b} \times \frac{m^2}{t - m_b^2} g^{\nu\rho} \times \\
& \times \left\{ [\varepsilon_L(p_2) \cdot \varepsilon_L(p_3)] \left[\frac{p_2}{m} - \frac{p_3}{m} \right]_\nu - 2 \left[\varepsilon_L(p_2) \cdot \frac{p_3}{m} \right] [\varepsilon_L(p_2) - \varepsilon_L(p_3)]_\nu \right\} \times \\
& \times \left\{ [\varepsilon_L(p_4) \cdot \varepsilon_L(p_1)] \left[\frac{p_4}{m} - \frac{p_1}{m} \right]_\rho - 2 \left[\varepsilon_L(p_4) \cdot \frac{p_1}{m} \right] [\varepsilon_L(p_4) - \varepsilon_L(p_1)]_\rho \right\}. \quad (1.30)
\end{aligned}$$

The next step is in principle analog to the s channel but a little more complex here, because the x expansions to be pugged into (1.30) for the contracted

Lorentz vectors already differ in the subleading order $\mathcal{O}(x^0)$ which must be taken into account here, cf. eqns. (B.4) and (B.9). Therefore the x expansion can only be factored out partially in this case, giving rise to some additional mixing terms:

$$\begin{aligned}
& (-ig^2) f_{a_2 a_3 b} f_{a_4 a_1 b} \times \frac{m^2}{t - m_b^2} \times \\
& \times \left\{ \left(\frac{t}{2m^2} + \frac{t}{s} \right)^2 \left[\left(\frac{p_2}{m} - \varepsilon_L(p_2) \right) - \left(\frac{p_3}{m} - \varepsilon_L(p_3) \right) - \varepsilon_L(p_2) + \varepsilon_L(p_3) \right] \cdot \right. \\
& \quad \cdot \left[\left(\frac{p_4}{m} - \varepsilon_L(p_4) \right) - \left(\frac{p_1}{m} - \varepsilon_L(p_1) \right) - \varepsilon_L(p_4) + \varepsilon_L(p_1) \right] + \\
& \quad + 2 \left(\frac{t}{2m^2} + \frac{t}{s} \right) \left(-\frac{u}{s} \right) \left[\left(\frac{p_2}{m} - \varepsilon_L(p_2) \right) - \left(\frac{p_3}{m} - \varepsilon_L(p_3) \right) - \varepsilon_L(p_2) + \varepsilon_L(p_3) \right] \cdot \\
& \quad \quad \cdot \left[\frac{p_4}{m} - \frac{p_1}{m} \right] + \\
& \quad \left. + \left(-\frac{u}{s} \right)^2 \left[\frac{p_2}{m} - \frac{p_3}{m} \right] \cdot \left[\frac{p_4}{m} - \frac{p_1}{m} \right] \right\}. \tag{1.31}
\end{aligned}$$

Because of the x^{-1} factor in the propagator, the terms inside the curly brackets only have to be computed down to $\mathcal{O}(x^2)$, so that from the second term beginning in line four only the leading order needs to be collected, whereas the last term is of $\mathcal{O}(x^1)$ and can be neglected entirely for the expansion carried out here. However, this last term forms the leading-order contribution to the Coulomb singularity of t -channel photon exchange in forward scattering, because it is the highest-order term where the t in the denominator of the propagator is not cancelled by a t from the Lorentz contractions in the numerator: A more detailed account of this will be given in section 1.3.4.

The final result for this amplitude is now found completely analog to the s channel by evaluating the remaining Lorentz contractions of the terms inside the curly bracket, using eqns. (B.3), (B.5) and (B.11), (B.13) for the first term and eqns. (B.8), (B.10) for the second one. After expanding the entire curly bracket in powers of x and making some use of relation (A.3), one finds

$$\begin{aligned}
\text{Diagram} & = (ig^2) f_{a_2 a_3 b} f_{a_4 a_1 b} \times \frac{t}{t - m_b^2} \times \left[\frac{t(s-u)}{4m^4} + \frac{2t^2 - s(s-u)}{m^2 s} + \mathcal{O}(x^0) \right]. \tag{1.32}
\end{aligned}$$

It is no surprise that the leading order of this expression once more cancels exactly the respective contribution $\propto x^2$ of the contact term, cf. eqn. (1.21). The result for the u -channel diagram which remains from eqn. (1.17) can now be given immediately from the t -channel result, since the exchange $3 \leftrightarrow 4$

necessary for this transfer merely implies an exchange $t \leftrightarrow u$ in eqn. (1.32):

$$\begin{aligned}
 \text{Diagram} &= \left(\text{Diagram} \right)_{3 \leftrightarrow 4, t \leftrightarrow u} \\
 &= (ig^2) f_{a_2 a_4 b} f_{a_3 a_1 b} \times \frac{u}{u - m_b^2} \times \left[\frac{u(s-t)}{4m^4} + \frac{2u^2 - s(s-t)}{m^2 s} + \mathcal{O}(x^0) \right].
 \end{aligned} \tag{1.33}$$

1.3.4 Propagator Expansion and Leading-order Result

Now that all contributing diagrams are evaluated and the respective longitudinal polarization factors expanded in x , the last step to be done before summing everything up is to expand the propagator factors in the s , t and u channel boson exchange diagrams. Some care has to be taken while addressing this task, because even in the high energy limit considered here the t and u channel propagators do not necessarily become small due to the exchange of real gauge bosons in extreme forward (and backward) scattering: $\cos \theta \approx \pm 1$ which implies $t, u \approx 0$ from eqn. (A.4). Hence it is clear that extracting single terms from the propagator is formally only valid if the amplitudes are evaluated at a fixed angle which is well away from the forward and backward regions, so that t and u also become large with increasing s (cf. [32], ch. 3).

However, this is in basic contradiction to a partial wave expansion to be carried out later, since projection onto the spherical harmonics involves an integration over the whole unit sphere, cf. eqn. (1.5). This circumstance is being accounted for in the following way: The leading terms which become large in the forward directions are those where the respective t or u factors in the denominator of the propagator are not cancelled by equal factors coming from the polarizations and momenta in the numerator. As was already denoted along with eqn. (1.31) above, this happens for the first time in $\mathcal{O}(x^0)$ so that these terms are basically suppressed by a factor of x^{-1} compared to the leading high energy terms considered. On the other hand, the propagator terms with finite mass parameters—such as the W^\pm and the Z^0 in the SM—acquire logarithm factors containing the said masses after integration of the polar angle:

$$\int_{-s}^0 \frac{dt}{t - m^2} = \ln \frac{m^2}{s + m^2} \simeq -\ln x, \quad s \gg m^2. \tag{1.34}$$

It is now argued that these terms are suppressed by the factor $\ln x/x$ compared to the leading terms and can be neglected for all further considerations, at least as far as the SM gauge bosons are concerned.

However, the limit $m \rightarrow 0$ taken in eqn. (1.34), which describes the exchange of massless photons, produces a physical singularity known as *Coulomb singularity* (cf. [32], ch. 3). Its contribution, which becomes relevant only in the extreme forward directions, can be isolated from the overall amplitude and evaluated for finite angular ranges, e. g. the angular detector acceptance. This is done starting from eqn. (1.31) in the t channel: As denoted before, the leading term where the divergent behavior of the propagator for $t \rightarrow 0$ is not cancelled by the numerator comes from the last line of eqn. (1.31) and is of order $\mathcal{O}(x^0)$. With the non-trivial transformation law between the interaction basis and the mass basis of the SM gauge bosons (cf. [31], ch. 20),

$$\begin{pmatrix} B \\ W^3 \end{pmatrix} = \begin{pmatrix} \cos \theta_\omega & -\sin \theta_\omega \\ \sin \theta_\omega & \cos \theta_\omega \end{pmatrix} \begin{pmatrix} A \\ Z \end{pmatrix}, \quad (1.35)$$

with the Weinberg angle θ_ω (cf. section 2.1.1), causing the replacement $\frac{1}{t-m_b^2} \rightarrow \sin^2 \theta_\omega \frac{1}{t}$ due to the projection of the propagating photon onto the W^3 at the vertices, the relevant term of eqn. (1.31) then reads

$$\begin{aligned} i\mathcal{M}_C &= (-ig^2) f_{a_2 a_3 b} f_{a_4 a_1 b} \times \sin^2 \theta_\omega \left(\frac{u}{s}\right)^2 \frac{s-u}{t} + (3 \leftrightarrow 4, t \leftrightarrow u) \\ &= (-ig^2) f_{a_2 a_3 b} f_{a_4 a_1 b} \times 2 \sin^2 \theta_\omega \frac{s}{t} + (3 \leftrightarrow 4, t \leftrightarrow u) + \text{finite}, \end{aligned} \quad (1.36)$$

where the permutations given in brackets generate the symmetric u -channel contribution as usual. Note that the leading Coulomb-singular term in the cross section does not come from absolute-squaring eqn. (1.36), but from the interference term between \mathcal{M}_C and the leading-order contribution in x , cf. eqn. (1.39) below.

Bearing all these subtleties in mind, the propagator is now formally expanded into a geometric series:

$$\begin{aligned} \frac{k^2}{k^2 - m_b^2} &\xrightarrow{b=1,2} 1 + \frac{m^2}{k^2} + \left(\frac{m^2}{k^2}\right)^2 \frac{k^2}{k^2 - m^2} \quad \text{for } k^2 \equiv s, t, u \text{ and } |k^2| > m^2 \\ &\simeq 1 + \frac{m^2}{k^2}, \quad |k^2| \gg m^2 \end{aligned} \quad (1.37)$$

for the first two gauge components of the non-Abelian gauge field, i. e. $W^{1/2}$ exchange in the SM which implies external Z^0 because of the gauge structure of the vertices, cf. eqn. (1.14). However, the W^3 component propagating in pure $W^{1/2}$ scattering is no mass eigenstate, so that the propagations of the Z^0

and the photon superpose, cf. eqn. (1.35), corresponding to the replacement

$$\begin{aligned}
\frac{k^2}{k^2 - m_b^2} &\xrightarrow{b=3} \sin^2 \theta_\omega \frac{k^2}{k^2} + \cos^2 \theta_\omega \frac{k^2}{k^2 - m_Z^2} \\
&= \sin^2 \theta_\omega + \cos^2 \theta_\omega \left[1 + \frac{m_Z^2}{k^2} + \mathcal{O} \left(\left(\frac{m_Z^2}{k^2} \right)^2 \right) \right] \\
&\simeq 1 + \frac{m^2}{k^2}, \tag{1.38}
\end{aligned}$$

which gives the same result as (1.37) up to this order. These are the two leading terms of order $\mathcal{O}(x^0)$ and $\mathcal{O}(x^{-1})$ which are necessary to compute all mixing terms contributing to $\mathcal{O}(x^1)$ in the results of the exchange diagrams, eqns. (1.28), (1.32) and (1.33): Inserting (1.37) and expanding the remaining products, the summation of all four diagrams contributing to longitudinal gauge boson scattering, eqns. (1.21), (1.28), (1.32) and (1.33), can finally be carried out, resulting in

$$\begin{aligned}
\text{Diagram} &= \text{Diagram 1} + \text{Diagram 2} + \text{Diagram 3} + \text{Diagram 4} \\
&= (ig^2) \frac{1}{4m^2} \left[f_{a_1 a_2 b} f_{a_3 a_4 b} \times 5(t-u) \right. \\
&\quad \left. + f_{a_2 a_3 b} f_{a_4 a_1 b} \times (-5(t-u) + u) \right. \\
&\quad \left. + f_{a_2 a_4 b} f_{a_3 a_1 b} \times (-5(u-t) + t) \right] + \mathcal{O}(x^0). \tag{1.39}
\end{aligned}$$

This is the most general expression for the divergent $\mathcal{O}(x^1)$ high-energy behavior of this kind of scattering amplitudes in the SM. The individual terms of (1.39) already hint at the incomplete cancellation when the gauge amplitudes are summed up to physical processes, as pointed out in the next paragraph.

1.3.5 Basis Transformations

Mass and Charge With the general expression for the divergent parts of the amplitude given in eqn. (1.39), it is a straightforward step to compute the amplitudes of physical processes among eigenstates of charge and mass. For $W^{1/2}$ scattering this is but a rotation in isospin space: The only remaining step is to contract the unsaturated gauge indices in the sums of structure constants,

$$f_{a_i a_j b} f_{a_k a_l b} = \delta_{a_i a_k} \delta_{a_j a_l} - \delta_{a_i a_l} \delta_{a_j a_k} \quad \text{in the SU}(2), \tag{1.40}$$

with the respective components of the charge eigenstates in the interaction basis (cf. [31], ch. 20):

$$W_L^\pm(p_i) = \frac{1}{\sqrt{2}} (\delta_{a_i 1} \mp i\delta_{a_i 2}) W_L^{a_i}(p_i) , \quad i = 1, 2, 3, 4 . \quad (1.41)$$

Note that with all external momenta pointing inward, cf. eqn. (1.17) and appendix A, one consequently has to charge-conjugate the final state, thus technically computing the amplitude for an annihilation of four particles into vacuum, which is of course equal to the respective amplitude for $2 \rightarrow 2$ scattering due to crossing symmetries. The leading-order terms for some physical processes are now given, reproducing the results in [23, 24]:

- $W_L^+ W_L^- \rightarrow W_L^+ W_L^-$ scattering implies

$$\begin{aligned} f_{a_1 a_2 b} f_{a_3 a_4 b} &\rightarrow -1 , \\ f_{a_2 a_3 b} f_{a_4 a_1 b} &\rightarrow -1 , \\ f_{a_2 a_4 b} f_{a_3 a_1 b} &\rightarrow 0 , \end{aligned} \quad (1.42)$$

which leads to the following leading-order divergence of the amplitude:

$$\begin{aligned} i\mathcal{M}(W_L^+ W_L^- \rightarrow W_L^+ W_L^-) &= (ig^2) \frac{1}{4m^2} [-5(\cancel{t-u}) + 5(\cancel{t-u}) - u] \\ &= -i \frac{u}{v^2} , \end{aligned} \quad (1.43)$$

where the electroweak scale v was inserted using the symmetry-breaking relation (2.6), cf. section 2.1.1.

- For $W_L^- W_L^- \rightarrow W_L^- W_L^-$ scattering, the kinematic contributions are

$$f_{a_1 a_2 b} f_{a_3 a_4 b} \rightarrow 0 , \quad f_{a_2 a_3 b} f_{a_4 a_1 b} \rightarrow 1 , \quad f_{a_2 a_4 b} f_{a_3 a_1 b} \rightarrow 1 , \quad (1.44)$$

so that the divergent term reads

$$\begin{aligned} i\mathcal{M}(W_L^- W_L^- \rightarrow W_L^- W_L^-) &= (ig^2) \frac{1}{4m^2} [u + t] \\ &= -i \frac{s}{v^2} . \end{aligned} \quad (1.45)$$

Whenever external Z^0 are involved (always even numbers due to charge conservation), some care must be taken in principle when using the longitudinal polarization vectors for external particles, eqn. (1.8), during the computation of amplitudes, since $m_Z \neq m$. However, one may already expect from the small mass difference $\Delta m/m \approx 14\%$ that the error which comes up from

neglecting this circumstance should be small. Indeed, it turns out after some computation in the mass and charge basis that the prefactor of the amplitudes containing external Z^0 is exactly equal at leading order to that of external W^\pm only. It is crucial at this point to note that with asymptotic Z^0 the conservation of gauge currents, which lead to a vanishing contribution of the $k^\mu k^\nu$ part of the propagator in section 1.3.2, does not hold exactly any more, because the mass splitting between Z^0 and W^\pm violates the associated triplet symmetry. Hence one would expect a contribution from the polarization tensor which should be proportional to the difference of the squared masses, which can be readily verified in unitary gauge for asymptotic states with two Z and two W . Starting from eqn. (1.25) in the s channel, the term reads:

$$\begin{aligned}
& (-ig^2) f_{a_1 a_2 b} f_{a_3 a_4 b} \times \frac{m^2}{s - m^2} \times \{ [\varepsilon_L(p_1) \cdot \varepsilon_L(p_2)] \left[\frac{p_1}{m} - \frac{p_2}{m} \right] \cdot \frac{k}{m} \}^2 = \\
& = (-ig^2) f_{a_1 a_2 b} f_{a_3 a_4 b} \times \frac{m^2}{s - m^2} \times \left(\frac{s}{2mm_Z} \right)^2 \left(\frac{m_Z^2 - m^2}{m^2} \right)^2 \\
& = (-ig^2) f_{a_1 a_2 b} f_{a_3 a_4 b} \times \frac{s}{s - m^2} \times \frac{s}{m^2} \left(\frac{\sin^2 \theta_\omega}{2 \cos \theta_\omega} \right)^2, \tag{1.46}
\end{aligned}$$

where the Lorentz contractions have been carried out in leading order which suffices here. All other Lorentz contractions via the polarization tensor cancel each other, and the other kinematic channels result trivially from permuting the gauge indices and replacing s with t or u . Note that due to the gauge structure of the vertices there can never be two Z^0 which couple pointlike at one vertex, so that one always has mixed polarization contractions as displayed in eqn. (1.46), cf. also appendix B. The next step would be to redo all the other Lorentz contractions via the metric tensor and see how they are affected by the presence of external Z^0 . However, without giving any more details of this tedious task, it turns out that all modifications factor out at every order in x , so that the final result for the s channel reads:

$$\begin{aligned}
\text{Diagram} & = (ig^2) f_{a_1 a_2 b} f_{a_3 a_4 b} \times \frac{s}{s - m^2} \cos^2 \theta_\omega \times \\
& \times \left[\frac{s(t-u)}{4m^4} \cos^2 \theta_\omega + \frac{(t-u)}{m^2} \left(1 - \frac{1}{2} \sin^2 \theta_\omega \right) - \frac{s}{m^2} \left(\frac{\sin^2 \theta_\omega}{2 \cos \theta_\omega} \right)^2 + \mathcal{O}(x^0) \right], \tag{1.47}
\end{aligned}$$

where the global factor $\cos^2 \theta_\omega$ emerges because the $SU(2)$ gauge vertices project the two external Z onto their W^3 component, cf. eqn. (1.35). The other kinematic channels and the contact diagram also give the same results

as in pure $W^{1/2}$ scattering, cf. eqns. (1.21), (1.32) and (1.33), multiplied with identical angular factors as in eqn. (1.47) at each order in x .

However, it is obvious that the various terms in eqn. (1.47) cannot combine to reinstall the shape which was found in pure $W^{1/2}$ scattering, cf. eqn. (1.28): Only after expanding the propagator, cf. eqn. (1.37), and transforming into the charge basis, with a delta function $\delta_{a_i 3}$ inserted for every external $Z^0(p_i)$, do the leading-order terms of the gauge amplitudes combine to give the same prefactor as in $W^{1/2}$ scattering, namely just $\frac{1}{v^2}$. This circumstance gives rise to the following notion: Elastic scattering of longitudinal gauge bosons can be described exactly to leading order by the scattering of an unbroken $SU(2)_C$ triplet (W^+, Z^0, W^-) with masses m , i. e. the previous results for $W^{1/2}$ scattering, eqns. (1.21), (1.28), (1.32) and (1.33), hold exactly for all gauge components $a_i = 1, 2, 3$ up to the order $\mathcal{O}(x^1)$ considered here as long as they are always summed up to eigenamplitudes of charge or custodial isospin. For example, the scattering process

- $W_L^- Z_L^0 \rightarrow W_L^- Z_L^0$ contains gauge boson exchange terms according to

$$f_{a_1 a_2 b} f_{a_3 a_4 b} \rightarrow 1, \quad f_{a_2 a_3 b} f_{a_4 a_1 b} \rightarrow 1, \quad f_{a_2 a_4 b} f_{a_3 a_1 b} \rightarrow 0, \quad (1.48)$$

which are exactly opposite to eqn. (1.42), giving the $W_L^+ W_L^- \rightarrow W_L^+ W_L^-$ scattering amplitude, eqn. (1.43), with opposite sign, whereas

- $W_L^+ W_L^- \rightarrow Z_L^0 Z_L^0$ leads to contributions

$$f_{a_1 a_2 b} f_{a_3 a_4 b} \rightarrow 0, \quad f_{a_2 a_3 b} f_{a_4 a_1 b} \rightarrow -1, \quad f_{a_2 a_4 b} f_{a_3 a_1 b} \rightarrow -1, \quad (1.49)$$

hence giving the $W_L^- W_L^- \rightarrow W_L^- W_L^-$ scattering amplitude, eqn. (1.45), with opposite sign.

- Finally, the process $Z_L^0 Z_L^0 \rightarrow Z_L^0 Z_L^0$ is forbidden by the gauge structure of the $SU(2)_L$, as already denoted before:

$$f_{a_1 a_2 b} f_{a_3 a_4 b} \rightarrow 0, \quad f_{a_2 a_3 b} f_{a_4 a_1 b} \rightarrow 0, \quad f_{a_2 a_4 b} f_{a_3 a_1 b} \rightarrow 0. \quad (1.50)$$

All other possible processes are related to one of those addressed above by charge-conjugation and crossing symmetry.

Custodial Isospin As pointed out above, to leading order in the energy expansion the three massive gauge bosons W^\pm and Z^0 may be treated as an exact triplet under the unbroken global $SU(2)_C$ symmetry—completely analog to the low-energy pion triplet—so that all elastic $2 \rightarrow 2$ scattering processes which are possible among these triplet states conserve the associated

isospin quantum number I . It is therefore sensible to derive the eigenamplitudes corresponding to different isospin eigenstates carrying $I = 0, 1, 2$ which are possible with asymptotic states containing two particles with $I = 1$ and $I_3 = 0, \pm 1$ each:

$$\underline{1} \otimes \underline{1} = \underline{0} \oplus \underline{1} \oplus \underline{2}. \quad (1.51)$$

From isospin conservation together with crossing and CP symmetries, it follows that all corresponding $2 \rightarrow 2$ amplitudes can be written in terms of one single master amplitude $\mathcal{M}(s, t, u)$ symmetric under $t \leftrightarrow u$ [20, 24] (cf. [32], ch. 3). This is now briefly accounted for in the following way: Note first that, due to crossing symmetry, the scattering amplitudes of all $2 \rightarrow 2$ processes which can be mapped into each other by swapping one initial-state particle into the final state and vice versa are interrelated by the simple kinematic permutation $s \leftrightarrow t$ or $s \leftrightarrow u$, depending on the momentum convention. Furthermore, the conservation of the total isospin \vec{T} implies that the scattering matrix S must commute with the isospin operator:

$$[S, \vec{T}] = 0 \quad \text{and hence} \quad [S, T_{\pm}] = 0 \quad (1.52)$$

with the ladder operators T_{\pm} built up from the first two components of \vec{T} as usual.

With these two ingredients, all $2 \rightarrow 2$ scattering amplitudes among the triplet states may now be related to each other: At first, the master amplitude is identified with the process $W_L^+ W_L^- \rightarrow Z_L^0 Z_L^0$:

$$\mathcal{M}(s, t, u) \equiv \mathcal{M}(W_L^+ W_L^- \rightarrow Z_L^0 Z_L^0) = \frac{s}{v^2} + \mathcal{O}(x^0) \quad (1.53)$$

from eqns. (1.45) and (1.49). All other amplitudes are now related to this one using crossing symmetries and inserting ladder operators. For example, the amplitude for $W_L^- Z_L^0 \rightarrow W_L^- Z_L^0$ scattering is directly given by crossing eqn. (1.53):

$$\mathcal{M}(W_L^- Z_L^0 \rightarrow W_L^- Z_L^0) = \mathcal{M}(t, s, u), \quad (1.54)$$

whereas the process $W_L^- W_L^- \rightarrow W_L^- W_L^-$ is obtained from eqn. (1.54) using a lowering operator T_- and the commutation relation (1.52):

$$\begin{aligned} \mathcal{M}(W_L^- W_L^- \rightarrow W_L^- W_L^-) &= \langle W^- W^- | S | W^- W^- \rangle \\ &= \frac{1}{\sqrt{2}} \langle W^- W^- | S T_- | W^- Z^0 \rangle \\ &= \langle W^- Z^0 + Z^0 W^- | S | W^- Z^0 \rangle \\ &= \mathcal{M}(t, s, u) + (t \leftrightarrow u). \end{aligned} \quad (1.55)$$

The process $W_L^+W_L^- \rightarrow W_L^+W_L^-$ then simply follows from crossing eqn. (1.55):

$$\mathcal{M}(W_L^+W_L^- \rightarrow W_L^+W_L^-) = \mathcal{M}(s, t, u) + \mathcal{M}(t, s, u) , \quad (1.56)$$

while the process $Z_L^0Z_L^0 \rightarrow Z_L^0Z_L^0$ is derived from the identity

$$T_+ |W^- Z^0\rangle = \sqrt{2} |Z^0 Z^0 + W^- W^+\rangle \quad (1.57)$$

in the following way:

$$\begin{aligned} \langle Z^0 Z^0 | S | Z^0 Z^0 \rangle &= \frac{1}{\sqrt{2}} \langle Z^0 Z^0 | S T_+ | W^- Z^0 \rangle - \langle Z^0 Z^0 | S | W^- W^+ \rangle \\ &= \langle W^- Z^0 + Z^0 W^- | S | W^- Z^0 \rangle + \langle W^+ W^- | S | Z^0 Z^0 \rangle . \end{aligned} \quad (1.58)$$

Collecting the results of eqns. (1.53) and (1.55), this leads to

$$\mathcal{M}(Z_L^0Z_L^0 \rightarrow Z_L^0Z_L^0) = \mathcal{M}(s, t, u) + \mathcal{M}(t, s, u) + \mathcal{M}(u, s, t) . \quad (1.59)$$

Note that these relations are violated not only by $SU(2)_C$ -breaking operators but also very strongly in forward scattering where pure W^\pm scattering diverges due to W^3 and hence photon exchange while the amplitudes containing Z^0 only involve $W^{1/2}$ exchange and therefore stay finite ([32], ch. 3).

It is now straightforward to rewrite the results for the isospin product states, eqns. (1.53) – (1.56) and (1.59), in the basis of irreducible states of total isospin, cf. eqn. (1.51), thus imposing relations between the master amplitude $\mathcal{M}(s, t, u)$ with its two kinematic permutations and the three reduced amplitudes $\mathcal{M}_{I=0,1,2}$ corresponding to the different isospin channels which are possible in principle. Firstly, the case of $I = 2$ can be read off directly from eqn. (1.55):

$$\mathcal{M}(t, s, u) + \mathcal{M}(u, s, t) = \mathcal{M}_2 , \quad (1.60)$$

whereas eqn. (1.53) imposes the relation

$$\mathcal{M}(s, t, u) = \frac{1}{3} (\mathcal{M}_0 - \mathcal{M}_2) , \quad (1.61)$$

and finally eqn. (1.54) leads to the condition

$$\mathcal{M}(t, s, u) = \frac{1}{2} (\mathcal{M}_1 + \mathcal{M}_2) . \quad (1.62)$$

Solving the equation system (1.60) – (1.62), one finds the corresponding reduced isospin eigenamplitudes [34]:

$$\mathcal{M}_0 = 3\mathcal{M}(s, t, u) + \mathcal{M}(t, s, u) + \mathcal{M}(u, s, t) , \quad (1.63)$$

$$\mathcal{M}_1 = \mathcal{M}(t, s, u) - \mathcal{M}(u, s, t) , \quad (1.64)$$

$$\mathcal{M}_2 = \mathcal{M}(t, s, u) + \mathcal{M}(u, s, t) , \quad (1.65)$$

which can be readily evaluated to $\mathcal{O}(x^1)$ using the leading order of the master amplitude given in eqn. (1.53) and the interdependence of the Mandelstam variables, eqn. A.3:

$$\mathcal{M}_0 = 2 \frac{s}{v^2}, \quad (1.66)$$

$$\mathcal{M}_1 = \frac{t - u}{v^2}, \quad (1.67)$$

$$\mathcal{M}_2 = -\frac{s}{v^2}. \quad (1.68)$$

1.3.6 Partial Wave Expansion

Now that all amplitudes have been evaluated and transformed into physically sensible bases such as mass/charge or custodial isospin, their leading-order partial wave coefficients $a_L(s)$ are computed using eqn. (1.5) in order to examine their high energy behavior. Since the entire propagator structure of the amplitudes is either suppressed in the x expansion for exchange of massive SM bosons, cf. eqn. (1.34), or has been subtracted for divergent photon exchange, cf. eqn. (1.36), it is a trivial step to expand the leading amplitudes with respect to their $\cos\theta$ factors: The only partial waves which contribute in this approximation are $L = 0$ or 1 , depending on the occurring combinations of s , t and u .

As pointed out in section 1.1, the theory considered, in this case just the SM, is only consistent up to the CMS energy where $|a_L| \gtrsim 1/2$. This critical energy $\sqrt{s_c}$ is now evaluated for the partial wave coefficients of the various scattering processes addressed above, beginning with the physical basis of mass and charge:

$$a_{0/1}(W_L^+ W_L^- \rightarrow W_L^+ W_L^-) = -\frac{1}{64\pi} \frac{s}{v^2} \quad \Rightarrow \quad \sqrt{s_c} = 2.4 \text{ TeV}, \quad (1.69)$$

$$a_0(W_L^+ W_L^- \rightarrow Z_L^0 Z_L^0) = \frac{1}{32\pi} \frac{s}{v^2} \quad \Rightarrow \quad \sqrt{s_c} = 1.7 \text{ TeV}, \quad (1.70)$$

where v has been replaced by the Fermi constant $G_F = 1.166 \times 10^{-5} \text{ GeV}^{-2}$ according to eqn. (2.6) to calculate the numerical values. Now the coefficients of the isospin amplitudes, eqns. (1.66) – (1.68), are given together with their

corresponding critical energy scales (cf. [32], ch. 3):

$$a_0(I=0) = \frac{1}{16\pi} \frac{s}{v^2} \quad \Rightarrow \quad \sqrt{s_c} = 1.2 \text{ TeV}, \quad (1.71)$$

$$a_1(I=1) = \frac{1}{96\pi} \frac{s}{v^2} \quad \Rightarrow \quad \sqrt{s_c} = 3.0 \text{ TeV}, \quad (1.72)$$

$$a_0(I=2) = -\frac{1}{32\pi} \frac{s}{v^2} \quad \Rightarrow \quad \sqrt{s_c} = 1.7 \text{ TeV}. \quad (1.73)$$

From eqns. (1.69) – (1.73) it is clear that the most divergent partial wave coefficient is the s -wave of the custodial isospin amplitude corresponding to $I=0$, which will therefore constitute the unitarity bound for the Higgsless SM of 1.2 TeV. Any new physics models designed to explain electroweak symmetry breaking should at least delay this consistency limit up to a higher energy scale if not remove it entirely.

1.3.7 Higgs Scenario

The standard example for a new electroweak symmetry-breaking physics sector is the Higgs mechanism [15, 16, 21, 22] postulating a new fundamental scalar to do the job, cf. section 2.1.1. All other SM fields are coupled to this new Higgs field: The gauge fields via the covariant derivative of the Higgs field and the fermions via Yukawa terms for mass generation. Because of the construction principle to generate these masses through a non-vanishing vacuum expectation value (VEV) of the Higgs field, these Higgs couplings to the SM fields must be proportional to the measured mass parameters. For example, consider the coupling of massive gauge bosons to the Higgs in the GWS theory (cf. [31], ch. 20):

$$\begin{aligned} (D_\mu H)^\dagger (D^\mu H) &= \frac{1}{2} v h \left(g^2 \vec{W}_\mu \cdot \vec{W}^\mu + g'^2 B_\mu B^\mu + 2gg' W_\mu^3 B^\mu \right) + \\ &\quad + (\text{mass terms}) + (\text{kinetic terms}) + (\text{quartic terms}) \\ &= \frac{2}{v} h \left(m^2 W_\mu^+ W^{-\mu} + m_Z^2 Z_\mu Z^\mu \right) + \dots \end{aligned} \quad (1.74)$$

$$\text{with } D_\mu H = \frac{1}{\sqrt{2}} \left(\partial_\mu - ig \vec{W}_\mu \cdot \vec{\tau} - ig' B_\mu \right) \begin{pmatrix} 0 \\ v + h(x) \end{pmatrix},$$

where the quartic couplings have been neglected because they do not contribute to tree-level scattering of gauge bosons. Neglecting the fact that the W^3 is actually no mass eigenstate, the Feynman rule for the cubic interaction

vertex in the basis of the $SU(2)_L$ gauge field components can be read off from eqn. (1.74):

$$\begin{array}{c} 1 \\ \diagdown \\ \text{---} \\ \diagup \\ 2 \\ | \\ \text{---} \\ h \end{array} \rightarrow 2i \frac{m^2}{v} \delta_{a_1 a_2} g_{\mu_1 \mu_2}, \quad (1.75)$$

where the usual numeration scheme for the gauge bosons has been used, cf. section 1.2. Then the additional diagrams contributing to elastic gauge boson scattering, eqn. (1.17), arise from Higgs exchange via the new vertex:

$$\begin{array}{c} 2 \\ \diagdown \\ \text{---} \\ \diagup \\ 1 \\ | \\ \text{---} \\ 3 \\ \diagdown \\ \text{---} \\ \diagup \\ 4 \end{array} = \left(\begin{array}{c} \text{---} \\ \diagdown \\ \text{---} \\ \diagup \\ \text{---} \\ \diagdown \\ \text{---} \\ \diagup \end{array} \right)_{\text{SM}} + \begin{array}{c} \text{---} \\ | \\ \text{---} \\ h \\ | \\ \text{---} \\ \text{---} \end{array} + \begin{array}{c} \text{---} \\ | \\ \text{---} \\ h \\ | \\ \text{---} \\ \text{---} \end{array} + \begin{array}{c} \text{---} \\ | \\ \text{---} \\ h \\ | \\ \text{---} \\ \text{---} \end{array}. \quad (1.76)$$

Plugging in the Higgs propagator (cf. [31], ch. 21),

$$\frac{i}{k^2 - m_h^2}, \quad (1.77)$$

the s -channel Higgs exchange diagram can now be computed explicitly:

$$\begin{aligned}
 \begin{array}{c} \text{---} \\ | \\ \text{---} \\ h \\ | \\ \text{---} \\ \text{---} \end{array} &= \varepsilon_L^{\mu_1}(p_1) \varepsilon_L^{\mu_2}(p_2) \varepsilon_L^{\mu_3}(p_3) \varepsilon_L^{\mu_4}(p_4) \times \frac{i}{s - m_h^2} \times \\
 &\times \left(2i \frac{m^2}{v} \right)^2 \delta_{a_1 a_2} \delta_{a_3 a_4} g_{\mu_1 \mu_2} g_{\mu_3 \mu_4} \\
 &= (-i) \delta_{a_1 a_2} \delta_{a_3 a_4} \times \frac{(2m^2)^2}{v^2 s} [\varepsilon_L(p_1) \cdot \varepsilon_L(p_2)]^2 \times \frac{s}{s - m_h^2} \\
 &= (-i) \delta_{a_1 a_2} \delta_{a_3 a_4} \times \frac{s}{v^2} + \mathcal{O}(x^0), \quad (1.78)
 \end{aligned}$$

where in the last line the leading terms in x have been inserted for the propagator and the polarization contraction, cf. eqns. (1.37) and (B.3), to find the leading order $\propto x$ of the Higgs exchange amplitude. This is of course only valid at an energy scale $s > m_h^2$, i. e. the Higgs has to be light enough to cancel the divergent terms presented in section 1.3 before they actually violate unitarity, which implies $m_h < 1.2$ TeV. The t and u channel amplitudes are obtained by performing the permutations pointed out in eqns. (1.29) and (1.33). From eqn. (1.78) it is also clear that neglecting the difference between W^3 and Z produces no error at leading order, because any external mass going into the numerator via the Higgs vertex is cancelled by the denominator of the leading term of the respective longitudinal polarization

contraction. Now it is also clear that the leading order of the gauge diagrams must necessarily be independent of whether or not there are Z bosons in the asymptotic states, if the corresponding Higgs contribution is to cancel it exactly.

In order to compare the high energy limit of all Higgs exchange and gauge interaction amplitudes, the gauge indices in eqn. (1.78) can again be contracted with the components of external states in a specific basis, just as in section 1.3.5. For example, consider the basis of physical states [24]:

- For $W_L^+ W_L^- \rightarrow W_L^+ W_L^-$ scattering the kinematic contributions are

$$\delta_{a_1 a_2} \delta_{a_3 a_4} \rightarrow 1, \quad \delta_{a_2 a_3} \delta_{a_4 a_1} \rightarrow 1, \quad \delta_{a_2 a_4} \delta_{a_3 a_1} \rightarrow 0, \quad (1.79)$$

so that the resulting leading-order Higgs amplitude reads

$$\mathcal{M}_h (W_L^+ W_L^- \rightarrow W_L^+ W_L^-) = -\frac{s+t}{v^2} = \frac{u}{v^2}, \quad (1.80)$$

cancelling exactly the result of the gauge interactions, eqn. (1.43).

- $W_L^- W_L^- \rightarrow W_L^- W_L^-$ scattering gets kinematic contributions from the t and u channels, implying

$$\mathcal{M}_h (W_L^- W_L^- \rightarrow W_L^- W_L^-) = \frac{s}{v^2}, \quad (1.81)$$

which also cancels the respective gauge interaction term, eqn. (1.45).

All other relevant amplitudes can be found completely analog to the procedure of section 1.3.5, leading to the same kind of cancellations.

1.4 Top Pair Annihilation into Gauge Bosons

In the previous section it was shown that the inherent structure of gauge boson self-interactions occurring in non-Abelian local symmetries leads to a cancellation of the most divergent terms of $\mathcal{O}(x^2)$ in the scattering of longitudinal modes through the interplay of the various contributing diagrams, so that the high energy divergence is delayed to $\mathcal{O}(x^1)$ in the SM. However, according to eqn. (1.10), even two longitudinal bosons in the asymptotic states may be enough to contribute to this order, thus potentially causing unitarity violation in scattering processes other than elastic gauge boson scattering. Restricting oneself once more to tree-level $2 \rightarrow 2$ scattering, these dangerous processes are fermion pair annihilations into longitudinal gauge bosons, $f\bar{f} \rightarrow W_L^+ W_L^-$ and $f\bar{f} \rightarrow Z_L^0 Z_L^0$, where top is certainly the most interesting flavor because of the large mass parameter.

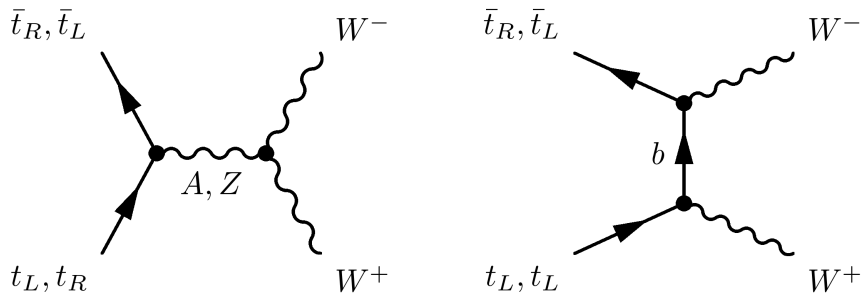


Figure 2: Potentially divergent $t\bar{t}$ annihilation diagrams. The contributions depend on the initial chiralities: s -channel gauge boson propagation works only with mixed initial chirality (left), t -channel b exchange is possible only for left-handed initial particles (right).

1.4.1 Chiral States

Given the chiral structure of the SM fermions, the $t\bar{t}$ initial states must be distinguished with respect to their chiral handedness in order to determine the contributing diagrams. Due to the structure of the covariant Dirac equation in the fermion sector,

$$\bar{\Psi}(i\not{D})\Psi = \bar{\Psi}_L(i\not{D}_L)\Psi_L + \bar{\Psi}_R(i\not{D}_R)\Psi_R \quad (1.82)$$

$$\text{with } D_L^\mu = \partial^\mu - ig\vec{W}^\mu \cdot \vec{\tau} - ig'B^\mu Y, \quad D_R^\mu = \partial^\mu - ig'B^\mu Y,$$

and heeding the fact that left-handed final-state fermions are equal to right-handed anti-fermions in the initial state, only the initial states with mixed chirality, $t_R\bar{t}_L$ and $t_L\bar{t}_R$, can annihilate pointlike into a neutral s -channel boson and hence into a W^\pm pair, with indices denoting handedness here, unlike the gauge boson notation for longitudinal modes. For the equal-handed initial states, $t_L\bar{t}_L$ and $t_R\bar{t}_R$, only t -channel fermion exchange remains to annihilate into gauge bosons, where initial $t_R\bar{t}_R$ can only produce a Z^0 pair, since right-handed fermions are singlets under $SU(2)_L$ and therefore do not couple directly to W^\pm , cf. eqn. (1.82). Note that, on the other hand, b exchange is therefore forbidden for initial $t_R\bar{t}_L$. It may then be concluded here that to the final state $Z_L^0 Z_L^0$ only t -channel top exchange contributes. However, the production of longitudinal Z^0 modes implies, to leading order, the coupling of a scalar boson to a conserved gauge current, cf. eqn. (1.9), which vanishes due to the corresponding Ward identity, so that only the final state $W_L^+ W_L^-$ remains to potentially produce a high energy divergence, cf. fig. 2 for all allowed initial chiralities and according diagrams.

The three remaining potentially dangerous initial states, $t_R\bar{t}_L$, $t_L\bar{t}_R$ and $t_L\bar{t}_L$, all lead to different high energy behavior when annihilating into a longi-

tudinal W^\pm pair, so that they are examined here separately, beginning with the easiest one, $t_R \bar{t}_L$, which carries hypercharge only (cf. [31], ch. 20 and 21 for the course of the whole section). In this case, only s -channel exchange of the neutral bosons A and Z must be taken into account. The fermion vertex comes from the Lagrangian term

$$-i\bar{u}_R g' \not{B} Y u_R = -i\bar{u}_R \gamma_\mu u_R \times \frac{2}{3} g \left(\sin \theta_\omega A^\mu - \frac{\sin^2 \theta_\omega}{\cos \theta_\omega} Z^\mu \right), \quad (1.83)$$

where the right-handed up-type hypercharge $Y = +\frac{2}{3}$ and the angular relation between the coupling constants, eqn. (2.1), as well as the mass-mixing coefficients of the neutral gauge bosons, eqn. (1.35), have been plugged in. When decaying into a W^\pm pair via the $SU(2)_L$ self-interaction vertex, cf. section 1.2, the neutral mass states collect exactly interchanged coefficients due to their respective admixture of the W^3 , cf. eqn. (1.35), so that, because of the relative sign, the overall product of vertex coefficients is exactly oppositely equal for the two exchange diagrams: $\pm \frac{2}{3} g \sin^2 \theta_\omega$. This allows for the summation of the propagators in the form

$$\begin{array}{c} \bar{t}_L \\ \nearrow \\ \text{---} \\ \searrow \\ t_R \end{array} \propto -\frac{1}{s} + \frac{1}{s - m_Z^2} = \left(\frac{m_Z^2}{s} \right) \frac{1}{s - m_Z^2}, \quad s > m_Z^2, \quad (1.84)$$

which is of course valid for the considerations here. Due to this propagator cancellation the overall order in x is lowered to $\mathcal{O}(x^0)$ even with longitudinally polarized final state bosons, so that the initial state $t_R \bar{t}_L$ produces no critical high energy behavior at all. Note that the gauge-dependent term of the propagator proportional to the Lorentz tensor $k^\mu k^\nu$, cf. eqn (1.22), does not contribute here either, following the same arguments as given below eqn. (1.25) in section 1.3.2.

The same structure occurs for the initial state $t_L \bar{t}_R$, but due to its additional weak isospin charge $\tau_3 = +\frac{1}{2}$ the vertex is a bit more complex because of W^3 contributions, so that not the entire Z propagator cancels against the photon propagator:

$$\begin{aligned} -i\bar{u}_L (g \not{W}^3 \tau_3 + g' \not{B} Y) u_L &= \\ &= -i\bar{u}_L \gamma_\mu u_L \times \left[\frac{1}{2} g (\cos \theta_\omega Z^\mu + \sin \theta_\omega A^\mu) + \frac{1}{6} g' (-\sin \theta_\omega Z^\mu + \cos \theta_\omega A^\mu) \right] \\ &= -i\bar{u}_L \gamma_\mu u_L \times g \left[\frac{2}{3} \left(\sin \theta_\omega A^\mu - \frac{\sin^2 \theta_\omega}{\cos \theta_\omega} Z^\mu \right) + \frac{1}{2 \cos \theta_\omega} Z^\mu \right], \end{aligned} \quad (1.85)$$

where the left-handed up-type hypercharge $Y = +\frac{1}{6}$ has been inserted in the second line. The first term leads again to a propagator cancellation as shown above in eqn. (1.84), whereas the second term constitutes an $\mathcal{O}(x^1)$

contribution. Collecting a factor $\cos \theta_\omega$ from the three-boson vertex, the entire $\mathcal{O}(x^1)$ s -channel amplitude then reads

$$\begin{array}{c} \bar{t}_R \\ \nearrow \\ \bullet \\ \nwarrow \\ t_L \end{array} \begin{array}{c} \text{---} \\ \text{---} \\ \text{---} \\ \text{---} \\ \text{---} \end{array} = \bar{v}_L \gamma_\mu u_L \times \left(-\frac{1}{2}ig\right) \frac{-ig^{\mu\nu}}{s - m_Z^2} (ig) \times \frac{s}{2m^2} (p_- - p_+)_\nu, \quad (1.86)$$

where the leading-order approximation for the polarization vectors, eqn. (1.9), has already been plugged in, and the p_\pm denote the corresponding 4-momenta of the final-state W^\pm . However, for this initial state also the t -channel b exchange diagram contributes, cf. fig. 2, and it turns out that, similar to the gauge cancellations in the leading order of elastic gauge boson scattering, it delivers exactly the correct term to cancel the leading order $\propto x$: The purely left-handed Lagrangian term reads

$$-i\bar{q}_L g (W^1 \tau_1 + W^2 \tau_2) q_L = -\frac{i}{\sqrt{2}} g (\bar{u}_L W^+ d_L + \bar{d}_L W^- u_L), \quad (1.87)$$

and the fermion propagator is (from [31], ch. 4)

$$\frac{i(\not{k} + m_f)_{\alpha\beta}}{k^2 - m_f^2}, \quad (1.88)$$

with Dirac indices α, β and the fermion mass m_f , so that the resulting exchange amplitude can be assembled:

$$\begin{array}{c} \bar{t}_R \\ \nearrow \\ \bullet \\ \nwarrow \\ t_L \end{array} \begin{array}{c} \text{---} \\ \text{---} \\ \text{---} \\ \text{---} \\ \text{---} \end{array} = \left(-\frac{i}{\sqrt{2}}g\right)^2 \bar{v}_L \frac{\not{p}_-}{m} \frac{i(\not{k} + m_b)}{t - m_b^2} \frac{\not{p}_+}{m} u_L(p_t), \quad (1.89)$$

with momentum transfer $p_t - p_+ \equiv k$ where p_t denotes the momentum of the initial t_L . Note that once more the longitudinal polarization vectors have already been replaced by their leading order, cf. eqn. (1.9). Now the Dirac equation can be plugged in,

$$\not{p}_+ u_L(p_t) = (m_t - \not{p}_t + \not{p}_+) u_L(p_t) = (m_t - \not{k}) u_L(p_t), \quad (1.90)$$

producing an additional term where one momentum is traded for the large but constant mass parameter m_t in the numerator, so that it contributes to $\mathcal{O}(x^{1/2})$ only. Inserting (1.90) into eqn. (1.89) and using $\not{k}^2 = k^2$, one finds

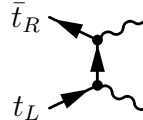
$$\left(\frac{1}{2}ig^2\right) \bar{v}_L \frac{\not{p}_-}{m^2} u_L(p_t) + \mathcal{O}(x^{1/2}) \quad \text{with} \quad m_b \simeq 0. \quad (1.91)$$

Finally, momentum conservation and the Dirac equation are used to rewrite the remaining slashed momentum as follows:

$$\bar{v}_L \not{p}_- u_L = \frac{1}{2} \bar{v}_L (\not{p}_- - \not{p}'_+ + \not{p}'_t + \not{p}'_{\bar{t}}) u_L \quad (1.92)$$

$$= \frac{1}{2} \bar{v}_L (\not{p}_- - \not{p}'_+ + 2m_t) u_L, \quad (1.93)$$

which delivers the leading-order result for b exchange:



$$= \left(\frac{1}{2}ig^2\right) \bar{v}_L \gamma^\mu u_L \times \frac{1}{2m^2} (p_- - p_+)_\mu + \mathcal{O}(x^{1/2}) . \quad (1.94)$$

This term exactly cancels the leading order $\propto x$ of the s -channel contributions, eqn. (1.86).

The subleading order in the s channel comes from the subleading terms of the propagator and the polarization contraction and is therefore $\propto x^0$, hence showing no divergent high energy behavior any more. On the other hand, in the b exchange amplitude, eqn. (1.89), trading slashed momenta for fermion masses via the Dirac equation while deriving expr. (1.94) gives rise to some potentially divergent terms of order $\mathcal{O}(x^{1/2})$. Consider the term which arises from inserting eqn. (1.90):

$$\left(-\frac{1}{2}ig^2\right) \bar{v}_L \frac{\not{p}'_- \not{k}'_- m_t}{m \not{t} m} u_L = \left(-\frac{1}{2}ig^2\right) \bar{v}_L \left(\frac{m_t}{m^2} + \frac{m_t^2 \not{k}'_-}{m^2 \not{t}}\right) u_L , \quad (1.95)$$

where the same manipulation as in eqn. (1.90) has been performed for $\bar{v}_L \not{p}'_-$ to find the right-hand side. The first term of expr. (1.95) exactly cancels the $\mathcal{O}(x^{1/2})$ term which comes from inserting eqn. (1.93), and the second term in (1.95) is of $\mathcal{O}(x^0)$, so that no unitarity-violating behavior remains for this initial state.

Finally, consider the equal-handed initial state $t_L \bar{t}_L$ where only b exchange is possible: The slashed momentum in the fermion propagator, eqn. (1.88), does not contribute because the flipped chirality structure of the initial state gives zero together with the additional γ matrix. Hence the only non-vanishing contribution from t -channel b exchange must be proportional to the bottom mass of the propagator, and therefore basically of order $\mathcal{O}(x^{1/2})$.

1.4.2 Helicity States

After analyzing the scattering of chiral interaction eigenstates, the issue of physically sensible initial states must be addressed now: Rather than chiral eigenstates, one would have to consider specific eigenstates of the helicity operator $h \equiv \hat{p} \cdot \vec{S}$ which projects the spin onto the 3-momentum direction (cf. [31], ch. 3), denoted right-handed for $h = +\frac{1}{2}$ and left-handed for $h = -\frac{1}{2}$. This is Lorentz-invariant only for massless fermions, since for massive particles, which propagate with less than speed of light, one can always boost into a reference frame where the helicity is flipped. Furthermore, helicity eigenstates are no chiral interaction eigenstates any more when the fermions have finite masses: Any given helicity contains an admixture with

relatively flipped chirality which is suppressed by the particle mass over the energy in the chosen frame, \sqrt{s} in the CMS of two fermions.

It follows that helicity eigenstates of initial $t\bar{t}$ in the CMS can be treated as interaction eigenstates up to a correction proportional to m_t/\sqrt{s} which lowers the respective order by $x^{-1/2}$. This implies that opposite helicities in the initial state show no divergent high energy behavior just like opposite chiralities, because after one chirality flip s -channel production of neutral gauge bosons is forbidden again due to the chiral vertex structure, and two chirality flips already lower the order to $\mathcal{O}(x^0)$. Similar arguments apply for t -channel b exchange: After one chirality flip, collecting the slashed momentum of the b propagator gives zero due to chirality, and collecting m_b gives contributions to $\mathcal{O}(x^0)$ only.

However, the picture is very different when comparing initial states of equal chirality with those of equal helicity: In the interaction basis, the leading high energy divergent term is $\propto m_b\sqrt{s}/m^2$, cf. the discussion above, whereas for initial helicity eigenstates the largest leading-order contribution is $\propto m_t\sqrt{s}/m^2$ which results from flipping the chirality once and collecting the slashed momentum in the propagator: This is the leading-order high energy divergence of the $t\bar{t} \rightarrow W_L^+W_L^-$ scattering amplitude in the higgsless SM. Inserting all numerical values, it leads to unitarity violation of the partial wave coefficient a_0 at an energy of roughly 30 TeV, which thus constitutes an upper limit of this process for the occurrence of new physics: In the presence of a Higgs field, for example, the divergence is cancelled by s -channel Higgs exchange, as long as $m_h < 30$ TeV [35]. However, as already mentioned in the introduction, the Higgs mechanism is but the simplest of a whole bunch of different ideas to account for electroweak symmetry breaking and unitarity violation in the SM. In the next chapter, one of the alternative approaches is introduced with the 3SHLM [1], describing its mechanism of electroweak symmetry breaking as well as the influence of its new physical degrees of freedom on the unitarity-violating scattering processes discussed in the course of this chapter.

2 The Three Site Higgsless Model

2.1 Construction

2.1.1 Chiral Lagrangian

A sensible starting point for the construction of new models which break the electroweak symmetry spontaneously is the formalism of the so-called *chiral Lagrangian* (for the whole section, cf. [32], ch. 2): It contains the full electroweak gauge group $SU(2)_L \times U(1)_Y$ with according gauge fields $W_\mu = \vec{W}_\mu \cdot \vec{\tau}$ ($\tau_i = \frac{\sigma_i}{2}$ are the generators of the $SU(2)$ with the Pauli matrices σ_i , $i = 1, 2, 3$) and B_μ as well as gauge coupling constants g und g' ,

$$g/g' \equiv \tan \theta_\omega \quad (2.1)$$

with the Weinberg angle θ_ω . Symmetry breaking is parametrized formally and model-independently, i. e. at first without any phenomenological implications, by a complex 2×2 matrix field $\Sigma(x)$, whose bilinear transformation under local gauge transformations $U(x) \in SU(2)_L$ and $V(x) \in U(1)_Y$,

$$\Sigma(x) \rightarrow U(x) \Sigma(x) V^\dagger(x), \quad (2.2)$$

is fixed uniquely by the necessity of invariant mass terms for fermions as well as gauge bosons: The chiral SM fermion fields Ψ_L and $\Psi_R = (u/d)_R$ receive their masses from invariant Yukawa couplings to the Σ (neutrino masses not taken into account):

$$\bar{\Psi}_L \Sigma \begin{pmatrix} \lambda_u & 0 \\ 0 & \lambda_d \end{pmatrix} \begin{pmatrix} u_R \\ d_R \end{pmatrix} \quad (2.3)$$

with the non-trivial matrices $\lambda_{u/d}$ in generation space of the SM fermions. Mass terms for the gauge bosons are contained in the kinetic term of the Σ field:

$$\frac{1}{2} \text{tr} \left[(D_\mu \Sigma) (D^\mu \Sigma)^\dagger \right] + \frac{\beta}{4} \text{tr} \left[\Sigma^\dagger (D_\mu \Sigma) \tau_3 \right] \text{tr} \left[\Sigma^\dagger (D^\mu \Sigma) \tau_3 \right] \quad (2.4)$$

$$\text{with } D_\mu \Sigma \equiv \partial_\mu \Sigma + ig W_\mu \Sigma - ig' \Sigma B_\mu,$$

in which the trace is taken over the $SU(2)$ generators. The second term in (2.4) parametrizes a mass splitting between $W^{1/2}$ and W^3 . This violates the *custodial symmetry* $SU(2)_C$ resulting from a global symmetry-breaking scheme $SU(2)_L \times SU(2)_R \rightarrow SU(2)_{diag} \equiv SU(2)_C$ which is in good approximation given in the SM: $\beta = \alpha T \approx 0$ (with the electromagnetic fine-structure constant α , for T cf. section 2.3.2).

The electroweak symmetry is broken by a non-vanishing VEV of the invariant operator $\text{tr} [\Sigma^\dagger(x) \Sigma(x)]$:

$$\langle \text{tr} [\Sigma^\dagger(x) \Sigma(x)] \rangle = 2v^2, \quad \text{e. g. via} \quad \langle \Sigma(x) \rangle = \sqrt{2}v \quad (2.5)$$

with the electroweak scale v . Plugging the VEV into expressions (2.3) and (2.4) results in bilinear terms in the fermion and gauge boson fields, which are in general non-diagonal in the interaction basis. Diagonalizing these terms leads to eigenvalues and eigenstates in the mass basis, so that the electroweak scale v introduced in (2.5) relates the gauge coupling constants of the theory to the gauge boson masses:

$$v^2 \equiv \frac{4m^2}{g^2} = \frac{1}{\sqrt{2}G_F} \quad \text{with} \quad m \equiv m_W = m_Z \cos \theta_w \quad (2.6)$$

on tree level. The VEV (2.5) can, for example, be generated dynamically by an invariant potential term in the Lagrangian:

$$-\frac{\mu^2}{4} \text{tr} [\Sigma^\dagger(x) \Sigma(x)] + \frac{\lambda}{16} \text{tr} [\Sigma^\dagger(x) \Sigma(x)]^2 + \dots \quad \text{with} \quad \frac{\mu^2}{\lambda} \equiv v. \quad (2.7)$$

If one additionally chooses the minimal linear parametrization of the Σ field with four scalar, real degrees of freedom, the Higgs sector of the GWS theory [15, 16] as presented in section 1.3.7 is exactly reproduced [32].

However, the choice of parametrization is not fixed in any way. Specifically, a minimal parametrization with respect to the number of real degrees of freedom is non-linear:

$$\Sigma(x) = \sqrt{2}v \exp\left(-\frac{i}{v} \vec{\tau} \cdot \vec{\omega}(x)\right) \quad (2.8)$$

with the three real degrees of freedom $\vec{\omega}(x)$ which are the Goldstone bosons of the broken symmetry generators. This parametrization contains no physical Higgs boson, though: It restricts the Σ field to unitary matrices, thus strengthening the VEV condition (2.5) to an equation,

$$\Sigma^\dagger(x) \Sigma(x) = 2v^2, \quad (2.9)$$

so that the potential term (2.7) becomes constant and therefore physically meaningless. It may be noted here that the non-linearly parametrized Lagrangian cannot be renormalized, since, upon expanding $\exp.$ (2.8), interactions of arbitrarily high order contribute already on tree level. The construction of the chiral Lagrangian is model-independent in the sense that any mechanism of spontaneous symmetry breaking should—at least in the limit of low energies of scale m —be equivalent to a certain parametrization of the Σ field.

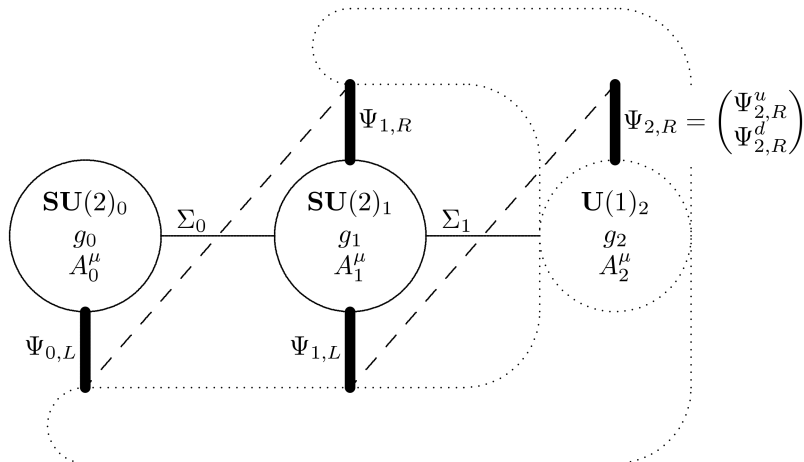


Figure 3: Field content and gauge structure of the 3SHLM as a moose diagram [6]. The dashed lines depict the invariant terms of the Yukawa sector (cf. section 2.2), the dotted line hints at the non-trivial $U(1)_2$ charges carried by all fermion fields.

2.1.2 Three Site Higgsless Model

Starting from the chiral Lagrangian, it is a natural and intuitive step to simply plug another $SU(2)$ group factor between the two gauge group factors of the SM and to connect these three with now two fields $\Sigma_{0/1}$ instead of just one. This is already the complete electroweak gauge group of the 3SHLM [1]:

$$SU(2)_0 \times SU(2)_1 \times U(1)_2 . \quad (2.10)$$

This construction may be seen as a maximally deconstructed version of a theory with one additional, compactified space-time dimension y , where the new dimension is discretized on just three sites. The continuous analog is then a gauged $SU(2)$ symmetry on the entire 5D bulk of space-time, which is broken by boundary conditions on a 4D brane of y to the $U(1)_2$, to be understood as the remaining τ_3 generator of the full $SU(2)$. In this picture it is consequent to stretch also the fermion fields Ψ over the whole extension of y , and to implement the chiral structure of the SM, with right-handed fermions Ψ_R carrying $U(1)$ charges exclusively, also via boundary conditions. The described gauge structure and complete field content of the 3SHLM is displayed in a moose model in fig. 3.

Such a 5D approach automatically accounts for the higgsless, non-linear parametrization of the Σ fields with three scalar degrees of freedom each: The Σ fields can be viewed as a deconstructed version of Wilson line fields

along the y direction in the adjoint representation of the $SU(2)$, and thus as y components of the 5D gauge field coming with the full bulk gauge group (cf. [31], ch. 15). The transformations of the Σ fields under local gauge transformations are, as in the chiral Lagrangian, completely fixed by the necessity to write down invariant mass terms for both fermions and gauge bosons [6]:

$$\Sigma_0 \rightarrow U_0 \Sigma_0 U_1, \quad \Sigma_1 \rightarrow U_1 \Sigma_1 e^{-\frac{i}{v} \theta \tau_3} \quad (2.11)$$

with $U_0 \in SU(2)_0$, $U_1 \in SU(2)_1$ and $e^{-\frac{i}{v} \theta \tau_3} \in U(1)_2$. The breaking of the full gauge symmetry (2.10) to the $U(1)_{em}$ is also instantiated analog to (2.9) by conditions for $\Sigma_{0/1}$:

$$(\Sigma^\dagger \Sigma)_{0/1} = 2v^2, \quad \text{e. g. via} \quad \langle \Sigma_{0/1} \rangle = \sqrt{2}v. \quad (2.12)$$

With respect to the chiral Lagrangian approach, one should be able to choose the parameters of the 3SHLM such that the effects of new physics associated with the additional $SU(2)_1$ gauge factor become negligibly small in the low energy limit, i. e. $\sqrt{s} \rightarrow m$, so that the model will morph into the chiral Lagrangian with a non-linear parametrization of the Σ field. This expectation may be illustrated again in the picture of the deconstructed 5D theory: In the continuous compactified case, there is an infinite tower of Kaluza-Klein (KK) excitations with masses proportional to the quantized momentum component k_y . In a dimension which is deconstructed on merely three sites, only two orthogonal modes remain in the Fourier spectrum, so that the particle spectrum comprises, apart from the SM particles associated with the boundary sites (the 0- and 2-brane), only the first KK excitation in each case, associated with the bulk site 1. Supposing a large enough mass splitting between the KK modes, the heavy modes can be integrated out at low energies, thereby collecting a suppression factor due to their own mass scale, which makes the morphing into the chiral Lagrangian become rather obvious.

2.2 Particle Spectrum and Mass Basis

2.2.1 Gauge Bosons

In order to find the mass eigenvalues and eigenstates of the gauge bosons, the kinetic terms of the Σ fields have to be evaluated starting from the interaction basis. These terms can be formulated completely analog to the chiral Lagrangian (2.4) with a summation over the two Σ fields [36]:

$$\sum_{i=0}^1 \frac{1}{2} \text{tr} \left[(D_\mu \Sigma_i) (D^\mu \Sigma_i)^\dagger \right] \quad (2.13)$$

$$\text{with } D^\mu \Sigma_i \equiv \partial^\mu \Sigma_i + ig_i A_i^\mu \Sigma_i - ig_{(i+1)} \Sigma_i A_{(i+1)}^\mu ,$$

where the custodial symmetry-breaking term was neglected here. Plugging in the complete expression for the covariant derivatives, the mass terms may easily be read off in unitary gauge, $\vec{\omega}_i = 0$:

$$\frac{v^2}{2} \sum_{i=0}^1 \left(g_i^2 \vec{A}_{i\mu} \cdot \vec{A}_i^\mu + g_{(i+1)}^2 \vec{A}_{(i+1)\mu} \cdot \vec{A}_{(i+1)}^\mu - g_i g_{(i+1)} \vec{A}_{i\mu} \cdot \vec{A}_{(i+1)}^\mu \right) , \quad (2.14)$$

where the dot-products are to be understood in the adjoint SU(2) representation of the A_i^μ , originating from the orthogonality of the SU(2) generators: $\text{tr} [\tau_i \tau_j] = \frac{\delta_{ij}}{2}$. So as to reach the regime denoted in the end of the preceding section, where the new gauge boson mass states W' and Z' are concentrated at the bulk site in the interaction basis and at the same time become heavy compared to m , expression (2.14) immediately suggests to choose the couplings g_0 and g_2 to be small in relation to g_1 , in order to localize heavy masses $m' \sim g_1 v$ in the bulk and light masses $m \sim g_{0/2} v$ on the branes. It is therefore sensible to expand in the small parameters

$$g_0/g_1 \equiv \xi \ll 1 \quad \text{and} \quad g_2/g_1 \equiv \eta \ll 1 . \quad (2.15)$$

Moreover, angular relations between g_0 and g_2 are defined analog to the GWS formalism:

$$g_0/g_2 \equiv t_\theta = \frac{s_\theta}{c_\theta} . \quad (2.16)$$

In the imposed limit (2.15) one finds $g_0 \approx g$ and $g_2 \approx g'$ approximately, which enables the identification of the brane gauge factors of (2.10) with the SM gauge group $SU(2)_L \times U(1)_Y$ to $\mathcal{O}(\xi^0)$. This corresponds again to the original construction principle of the model, i. e. embedding the SM on the branes and establishing the new physics in the bulk of y .

The terms included in (2.14) can now be cast into mass matrices for the separate gauge components of the A_i^a ($a = 1, 2, 3$ with Lorentz indices suppressed from here on), whose entries depend on ξ and η or equivalently t_θ . Heeding the fact that A_2 only contains a τ_3 factor and therefore does not contribute to the charged states W' , these can be expressed with the following matrix in the interaction basis (this and all following results in this section are taken from [1]):

$$\frac{g_1^2 v^2}{2} \begin{pmatrix} A_0^a & A_1^a \end{pmatrix} \begin{pmatrix} \xi^2 & -\xi \\ -\xi & 2 \end{pmatrix} \begin{pmatrix} A_0^a \\ A_1^a \end{pmatrix} , \quad a = 1, 2 . \quad (2.17)$$

The diagonalization of this matrix, using an expansion in ξ , results in one light eigenvalue, of $\mathcal{O}(\xi^2)$, and a heavy one, of $\mathcal{O}(\xi^0)$:

$$\begin{aligned} m^2 &= g_1^2 v^2 \left[\frac{1}{4}\xi^2 - \frac{1}{16}\xi^4 + \mathcal{O}(\xi^8) \right] \\ \text{and } m'^2 &= g_1^2 v^2 \left[1 + \frac{1}{4}\xi^2 + \frac{1}{16}\xi^4 + \mathcal{O}(\xi^6) \right] \end{aligned} \quad (2.18)$$

with $m' \equiv m_{W'}$, and corresponding eigenstates

$$\begin{aligned} \begin{pmatrix} W \\ W' \end{pmatrix} &\equiv \begin{pmatrix} v_W^0 & v_W^1 \\ v_{W'}^0 & v_{W'}^1 \end{pmatrix} \begin{pmatrix} A_0 \\ A_1 \end{pmatrix} \\ &= \begin{pmatrix} v_W^0 & v_W^1 \\ -v_W^1 & v_W^0 \end{pmatrix} \begin{pmatrix} A_0 \\ A_1 \end{pmatrix} \end{aligned} \quad (2.19)$$

$$\text{with } v_W^0 = 1 - \frac{1}{8}\xi^2 + \mathcal{O}(\xi^4)$$

$$\text{and } v_W^1 = \frac{1}{2}\xi + \frac{1}{16}\xi^3 + \mathcal{O}(\xi^5) .$$

In the ξ expansion one can see immediately that the light eigenstate identified with the SM W is located mostly on the 0-brane whereas the heavy eigenstate W' lives mostly at the bulk site. As for the 3-components of the gauge fields, the contributions from the 2-brane have to be taken into account, leading to the matrix

$$\frac{g_1^2 v^2}{2} \begin{pmatrix} A_0^a & A_1^a & A_2^a \end{pmatrix} \begin{pmatrix} \xi^2 & -\xi & 0 \\ -\xi & 2 & -t_\theta \xi \\ 0 & -t_\theta \xi & t_\theta^2 \xi^2 \end{pmatrix} \begin{pmatrix} A_0^a \\ A_1^a \\ A_2^a \end{pmatrix}, \quad a = 3. \quad (2.20)$$

After diagonalization, one eigenvalue is found which exactly equals zero: This is the photon with an eigenstate constructed in analogy to the SM by projecting onto the $U(1)_{em}$ via the electromagnetic charge e :

$$\begin{aligned} A &\equiv v_A^0 A_0 + v_A^1 A_1 + v_A^2 A_2 \\ &= \frac{e}{g_0} A_0 + \frac{e}{g_1} A_1 + \frac{e}{g_2} A_2, \end{aligned} \quad (2.21)$$

with e defined properly by the original gauge couplings of the model, in analogy to the SM:

$$\frac{1}{e^2} = \frac{1}{g_0^2} + \frac{1}{g_1^2} + \frac{1}{g_2^2}. \quad (2.22)$$

The other two non-zero mass eigenvalues are, expanded in ξ :

$$m_Z = \frac{g_1^2 v^2}{c_\theta^2} \left[\frac{1}{4} \xi^2 - \frac{(1-t_\theta^2)^2}{16} \xi^4 + \mathcal{O}(\xi^8) \right]$$

and $m_{Z'} = g_1^2 v^2 \left[1 + \frac{(1+t_\theta^2)}{4} \xi^2 + \frac{(1-t_\theta^2)^2}{16} \xi^4 + \mathcal{O}(\xi^6) \right],$ (2.23)

giving rise to the following set of eigenstates:

$$\begin{pmatrix} Z \\ Z' \\ A \end{pmatrix} \equiv \begin{pmatrix} v_Z^0 & v_Z^1 & v_Z^2 \\ v_{Z'}^0 & v_{Z'}^1 & v_{Z'}^2 \\ v_A^0 & v_A^1 & v_A^2 \end{pmatrix} \begin{pmatrix} A_0 \\ A_1 \\ A_2 \end{pmatrix} \quad (2.24)$$

with $v_Z^0 = c_\theta - \frac{c_\theta^3(1+2t_\theta^2-3t_\theta^4)}{8} \xi^2 + \mathcal{O}(\xi^4),$

$$v_Z^1 = \frac{c_\theta(1-t_\theta^2)}{2} \xi + \frac{c_\theta^3(1-t_\theta^2)^3}{16} \xi^3 + \mathcal{O}(\xi^5),$$

$$v_Z^2 = -s_\theta - \frac{s_\theta c_\theta^2(3-2t_\theta^2-t_\theta^4)}{8} \xi^2 + \mathcal{O}(\xi^4)$$

and $v_{Z'}^0 = -\frac{1}{2} \xi - \frac{(1-3t_\theta^2)}{16} \xi^3 + \mathcal{O}(\xi^5),$

$$v_{Z'}^1 = 1 - \frac{(1+t_\theta^2)}{8} \xi^2 + \mathcal{O}(\xi^4),$$

$$v_{Z'}^2 = -\frac{t_\theta}{2} \xi + \frac{t_\theta(3-t_\theta^2)}{16} \xi^3 + \mathcal{O}(\xi^5)$$

and the v_A^i already given in eqn. (2.21). Note again that the light states identified with the SM gauge bosons A and Z live on the branes while the new heavy state Z' is located mostly at the bulk site. All the Clebsch-Gordan coefficients given in eqns. (2.19), (2.21) and (2.24) will later become crucial for the evaluation of the gauge boson scattering amplitudes in the 3SHLM and deriving the unitarity bounds of the model, cf. section 2.3.1.

Having solved for the mass eigenvalues in dependence on the small parameter ξ , one can derive mutual relations between this parameter and the gauge boson masses m and m' using eqns. (2.18) and (2.23):

$$\xi^2 = 4 \left(\frac{m}{m'} \right)^2 + 8 \left(\frac{m}{m'} \right)^4 + \mathcal{O} \left(\left(\frac{m}{m'} \right)^6 \right)$$

or $\left(\frac{m}{m'} \right)^2 = \frac{1}{4} \xi^2 - \frac{1}{8} \xi^4 + \mathcal{O}(\xi^6),$ (2.25)

pointing out the fact that, after fixing the SM gauge boson masses and couplings, only one free parameter remains in this sector, to be chosen as ξ or m' , equivalently. Moreover, comparison of eqns. (2.18) and (2.23) immediately illustrates that the masses of the heavy gauge bosons are almost degenerate:

$$\frac{m_{Z'}^2 - m'^2}{m'^2} = \frac{1}{4} t_\theta^2 \xi^2 \lesssim \mathcal{O}(10^{-2}) , \quad (2.26)$$

cf. section 2.3.2 for the numerical upper limit, so that for all further discussions the heavy masses may be assumed as equal: $m_{Z'} \simeq m'$. At last, the interrelations of the mixing angles and hence gauge couplings between the SM and the 3SHLM can also be fixed in a ξ expansion from eqns. (2.18) and (2.23):

$$\begin{aligned} \cos^2 \theta_\omega|_Z &= \frac{m^2}{m_Z^2} \\ &= c_\theta^2 - s_\theta^2 \left(c_\theta^2 - \frac{1}{4} \right) \xi^2 + \mathcal{O}(\xi^4) \end{aligned} \quad (2.27)$$

$$\text{and therefore } \sin^2 \theta_\omega|_Z = s_\theta^2 + s_\theta^2 \left(c_\theta^2 - \frac{1}{4} \right) \xi^2 + \mathcal{O}(\xi^4) , \quad (2.28)$$

where the relations are understood to be evaluated at the Z pole. Eqns. (2.27) and (2.28) directly point out that $\theta \approx \theta_\omega$ and hence $g_0 \approx g$ and $g_2 \approx g'$ up to corrections of order $\mathcal{O}(\xi^2)$.

2.2.2 Fermions

The mass terms of the fermions are inserted analog to the chiral Lagrangian via Yukawa couplings to the Σ fields. To that end, the charges of the fermion fields under the various factors of the gauge group (2.10) are first assigned as denoted in fig. 3. The chiral structure of the SM is implemented by boundary conditions along y , i. e. by conditions for the brane fields: On the 0-brane there exist exclusively left-handed fermion fields $\Psi_{0,L}$, on the 2-brane only right-handed ones named $\Psi_{2,R}$. These last ones are isospin singlets under all $SU(2)$ factors and carry $U(1)_2$ charges according to the hypercharges of the right-handed SM fermions. All other Fermions, including the right-handed $\Psi_{1,R}$, are isospin doublets under their respective $SU(2)_i$ factor, $\tau_{i,3} = \pm \frac{1}{2}$, and additionally carry $U(1)_2$ charges according to the hypercharges of the left-handed SM fermions [1, 6].

With these assignments made, all invariant terms of the Yukawa sector of the 3SHLM can be written down analog to (2.3):

$$\lambda_L \bar{\Psi}_{0,L} \Sigma_0 \Psi_{1,R} + M \bar{\Psi}_{1,L} \Psi_{1,R} + \bar{\Psi}_{1,L} \Sigma_1 \begin{pmatrix} \lambda_{u,R} & 0 \\ 0 & \lambda_{d,R} \end{pmatrix} \begin{pmatrix} u_{2,R} \\ d_{2,R} \end{pmatrix} , \quad (2.29)$$

where all fermion fields must be understood as three-component vectors in generation space, and the gauge invariant Dirac mass term $M\bar{\Psi}_{1,L}\Psi_{1,R}$ was added for completeness. Except for the $\lambda_{u/d,R}$, which—like the $\lambda_{u/d}$ in expr. (2.3)—implement the non-trivial flavor structure of the SM, all parameters arising are generation-diagonal. Plugging in the VEV (2.12) gives

$$M \left\{ \epsilon_L \bar{\Psi}_{0,L} \Psi_{1,R} + \bar{\Psi}_{1,L} \Psi_{1,R} + \bar{\Psi}_{1,L} \begin{pmatrix} \epsilon_{u,R} & 0 \\ 0 & \epsilon_{d,R} \end{pmatrix} \begin{pmatrix} u_{2,R} \\ d_{2,R} \end{pmatrix} \right\} \quad (2.30)$$

with $\epsilon_L \equiv \frac{\sqrt{2}v\lambda_L}{M}$ and $\epsilon_{u/d,R} \equiv \frac{\sqrt{2}v\lambda_{u/d,R}}{M}$.

The parameters defined here can be interpreted as follows: The $\epsilon_{u/d,R}$ matrices are completely fixed by requiring the fermion mass splittings and flavor structure of the SM as known from the the Cabibbo-Kobayashi-Maskawa (CKM) quark-mixing matrix [37], and choosing the mass scale M of the heavy fermions, which is a free parameter of the 3SHLM. The delocalization parameter ϵ_L is a switch for adjusting the profile of the mass eigenstates along the gauge factors in the interaction basis, i. e. the admixture of contributions from the bulk site to the SM states, and vice versa. It completes the set of free parameters in the 3SHLM, together with m' and M . The next section is dedicated to the derivation of constraints on the parameter space, both from theoretical considerations and experimental results: In section 2.3.1 theoretical upper bounds on the mass scales m' and M will be motivated by the requirement that the new particles affect the unitarity-violating scales discussed in section 1.3, whereas the experimental constraints presented in section 2.3.2 will basically bound the said mass scales from below and impose a rather strict interdependence between ϵ_L and m' .

2.3 Constraints on Parameter Space

2.3.1 Theoretical Bounds from Unitarity Violation

Scattering Amplitudes in the 3SHLM In the 3SHLM with its enlarged gauge group, the gauge kinetic sector, which is basically constructed analog to eqn. (1.13), comprises a sum over the two independent non-Abelian gauge fields on sites 0 and 1:

$$\mathcal{L}_{\text{Yang-Mills}} = -\frac{1}{2} \sum_{i=0}^1 \text{tr} \left[A_{(i)\mu\nu} A_{(i)}^{\mu\nu} \right]. \quad (2.31)$$

The remaining gauge field A_2^μ gauges the $U(1)_2$ symmetry on the 2-brane, which is Abelian and shows no self-couplings. Because of the non-trivial

transformation matrices connecting interaction and mass states (cf. section 2.2.1), the self-interactions on sites 0 and 1 are generally not diagonal in the mass basis, so that the heavy modes W' and Z' couple not only among each other but also to the light SM states W , Z and A .

The resulting three-vertex has the same gauge and Lorentz structure as the three-boson vertex in the SM, cf. eqn. (1.14), only the coupling constant must be replaced by an expression containing the gauge couplings of the 3SHLM and the overlap of the mass eigenstates taken into account on the two sites 0 and 1 which carry the SU(2) factors, cf. eqns. (2.19) and (2.24):

$$\begin{array}{c} 1 \\ \text{wavy} \\ \text{3} \end{array} \begin{array}{c} 2 \\ \text{wavy} \\ \text{3} \end{array} \sim g_0(v_{V_1}^0)(v_{V_2}^0)(v_{V_3}^0) + g_1(v_{V_1}^1)(v_{V_2}^1)(v_{V_3}^1), \quad (2.32)$$

where the labels $V_i^{(l)}$ refer to the coefficients of those mass states which contain admixtures of the respective gauge components a_i , i. e. $V_i^{(l)} = W^{(l)}$ for $a_i = 1, 2$ and $V_i^{(l)} = Z^{(l)}$ for $a_i = 3$. With this additional vertex, the full tree-level matrix element for elastic scattering of longitudinal gauge bosons gets new contributions due to an exchange of the heavy gauge bosons:

$$\begin{array}{c} 2 \\ \text{wavy} \\ 1 \end{array} \begin{array}{c} 3 \\ \text{wavy} \\ 4 \end{array} = \left(\begin{array}{c} \text{SM} \\ \text{wavy} \\ \text{wavy} \end{array} \right) + \begin{array}{c} \text{wavy} \\ \blacktriangle \\ \text{wavy} \end{array} + \begin{array}{c} \text{wavy} \\ \blacktriangle \\ \text{wavy} \end{array} + \begin{array}{c} \text{wavy} \\ \blacktriangle \\ \text{wavy} \end{array}. \quad (2.33)$$

Note that the SM-like diagrams, eqn. (1.17), also get contributions from the bulk site due to the delocalization of the light mass states:

$$\begin{array}{c} 1 \\ \text{wavy} \\ \text{3} \end{array} \begin{array}{c} 2 \\ \text{wavy} \\ \text{3} \end{array} \sim g_0 \left[(v_{V_1}^0)(v_{V_2}^0)(v_{V_3}^0) + \frac{1}{\xi}(v_{V_1}^1)(v_{V_2}^1)(v_{V_3}^1) \right], \quad (2.34)$$

$$\begin{array}{c} 2 \\ \text{wavy} \\ 1 \end{array} \begin{array}{c} 3 \\ \text{wavy} \\ 4 \end{array} \sim g_0^2 \left[(v_{V_1}^0)(v_{V_2}^0)(v_{V_3}^0)(v_{V_4}^0) + \frac{1}{\xi^2}(v_{V_1}^1)(v_{V_2}^1)(v_{V_3}^1)(v_{V_4}^1) \right], \quad (2.35)$$

where $\xi \equiv g_0/g_1$, cf. section 2.2. However, because of the relative suppression of the bulk fields in the light mass eigenstates, $v_{V_i}^{0/2} \sim \mathcal{O}(\xi^0)$ and $v_{V_i}^1 \sim \mathcal{O}(\xi^1)$ from eqns. (2.19) and (2.24), the contributions from the bulk site to the SM-like contact and propagator diagrams will in general be suppressed at least by a factor ξ^2 compared to the brane contributions, so that to order $\mathcal{O}(\xi^0)$ with $g_0 \approx g$ the SM expressions discussed thoroughly in section 1.3 are reproduced. The only new $\mathcal{O}(\xi^0)$ contribution from the bulk site must therefore come from the exchange of a heavy gauge boson: Although the

coefficients alone also produce ξ^2 factors, cf. eqn. (2.32), the x expansion of the propagator conveys negative powers of ξ due to the large mass m' in the denominator. This first expectation will be discussed in detail further below, starting from the full scattering amplitude in the 3SHLM.

In order to tie in with the procedure of section 1.3 and use the results given there, this amplitude is derived at first for $W^{1/2}$ scattering only. Starting with the contact amplitude again, its result is just the same as in the SM, eqn. (1.21), with the replacement $g \rightarrow g_0$ and multiplication of the respective Clebsch-Gordan coefficients, i. e. eqn. (2.35) with $V_i \rightarrow W$:

$$\begin{aligned}
\text{Diagram} &= (-ig_0^2) \left[(v_W^0)^4 + \frac{1}{\xi^2} (v_W^1)^4 \right] \left[f_{a_1 a_2 b} f_{a_3 a_4 b} \left(\frac{s(t-u)}{4m^4} + 0 \right) + \right. \\
&\quad + f_{a_2 a_3 b} f_{a_4 a_1 b} \left(\frac{t(s-u)}{4m^4} - 2 \frac{tu}{m^2 s} \right) + \\
&\quad \left. + f_{a_2 a_4 b} f_{a_3 a_1 b} \left(\frac{u(s-t)}{4m^4} - 2 \frac{tu}{m^2 s} \right) \right] \\
&= (-ig_0^2) \left[1 - \frac{7}{16} \xi^2 + \mathcal{O}(\xi^4) \right] [\dots] . \tag{2.36}
\end{aligned}$$

Once again, this result explicitly illustrates the fact that considering only $\mathcal{O}(\xi^0)$, which implies setting $g_0 \approx g$ again, the SM expression is exactly reproduced.

Replacing g with g_0 once more, the s , t and u exchange diagrams can also be transferred formally from section 1.3, eqns. (1.28), (1.32) and (1.33), if all the non-trivial site-mixing structure is absorbed into the propagator factors. Consider the s channel at first:

$$\begin{aligned}
&\text{Diagram A} + \text{Diagram Z} + \text{Diagram Z'} = \\
&= (ig_0^2) f_{a_1 a_2 b} f_{a_3 a_4 b} \times \left[\frac{s(t-u)}{4m^4} + \frac{(t-u)}{m^2} + \mathcal{O}(x^0) \right] \times \\
&\quad \times \left\{ C_A(\xi) + C_Z(\xi) \frac{s}{s - m_Z^2} + C_{Z'}(\xi) \frac{s}{s - m'^2} \right\} , \tag{2.37}
\end{aligned}$$

where the functions $C_V(\xi)$ are just the squared ξ -dependent coefficients of the respective three-boson vertices corresponding to the different

propagating mass states, cf. eqns. (2.32) and (2.34):

$$\begin{aligned} C_A(\xi) &\equiv \left[(v_W^0)^2 (v_A^0) + \frac{1}{\xi} (v_W^1)^2 (v_A^1) \right]^2 \\ &= s_\theta^2 - s_\theta^4 \xi^2 + \mathcal{O}(\xi^4) , \end{aligned} \quad (2.38)$$

$$\begin{aligned} C_Z(\xi) &\equiv \left[(v_W^0)^2 (v_Z^0) + \frac{1}{\xi} (v_W^1)^2 (v_Z^1) \right]^2 \\ &= c_\theta^2 - \frac{(1+4c_{2\theta}-c_{4\theta})}{8} \xi^2 + \mathcal{O}(\xi^4) , \end{aligned} \quad (2.39)$$

$$\begin{aligned} C_{Z'}(\xi) &\equiv \left[(v_W^0)^2 (v_{Z'}^0) + \frac{1}{\xi} (v_W^1)^2 (v_{Z'}^1) \right]^2 \\ &= \frac{1}{16} \xi^2 - \frac{(3+5t_\theta^2)}{64} \xi^4 + \mathcal{O}(\xi^4) . \end{aligned} \quad (2.40)$$

Note that due to the orthonormality of the v_V^i ,

$$\sum_{V=A,Z,Z'} (v_V^i) (v_V^j) = \delta_{ij} , \quad i, j = 0, 1, 2 , \quad (2.41)$$

the sum of all $C_V(\xi)$ expectedly leaves just the external coefficients behind

$$C_A(\xi) + C_Z(\xi) + C_{Z'}(\xi) = (v_W^0)^4 + \frac{1}{\xi^2} (v_W^1)^4 , \quad (2.42)$$

so that, when approximating all propagators by unity and comparing with eqn. (2.36), the exact cancellation of the most divergent terms of order $\mathcal{O}(x^2)$ is obvious also in the 3SHLM, to all orders in ξ .

Leading-order Cancellations Now consider the ξ expansion of the coefficient functions for each propagator, eqns. (2.38) – (2.40): Formally taking the limit $m' \rightarrow \infty$ and hence $\xi \rightarrow 0$, the coefficients of the light propagators become $C_A \rightarrow s_\theta^2 \rightarrow \sin^2 \theta_\omega$ and $C_Z \rightarrow c_\theta^2 \rightarrow \cos^2 \theta_\omega$, cf. eqns. (2.27) and (2.28), and $C_{Z'} \rightarrow 0$ which reproduces the SM amplitudes as expected. However, if the heavy bosons are to interfere with the leading-order high energy divergence of the amplitudes, their mass m' must be bounded from above by $\sqrt{s_c}$, cf. section 1.3.6, hence ξ is small but finite. Therefore, in a regime where $m' < \sqrt{s} < \sqrt{s_c}$, the leading-order terms of the amplitudes can be isolated by geometrically expanding all propagators (including the heavy one) and sorting the leading power of the unbounded parameter $x = s/m^2$ in powers of ξ . It was already denoted that at order $\mathcal{O}(\xi^0)$ the only remaining task is to expand the heavy propagator analog to eqn. (1.37), always bearing in

mind the respective considerations of section 1.3.4:

$$\begin{aligned} \frac{k^2}{k^2 - m'^2} &= 1 + \frac{m'^2}{k^2} + \left(\frac{m'^2}{k^2}\right)^2 \frac{k^2}{k^2 - m'^2} \quad \text{for } k^2 \equiv s, t, u \text{ and } |k^2| > m'^2 \\ &= 1 + \left(\frac{4}{\xi^2} + 2 + \mathcal{O}(\xi^2)\right) \frac{m^2}{k^2} + \mathcal{O}\left((\xi^2 x)^{-2}\right), \end{aligned} \quad (2.43)$$

where relation (2.25) was plugged in up to the necessary order in ξ . It is stressed that, although the geometric series does converge in the regime $\xi^2 x > 1$ considered here, the first two terms of eqn. (2.43) constitute a much worse approximation compared to the case of light propagators (cf. the discussion in section 1.3.4), because every suppression factor x is offset by a factor of ξ^2 due to the heavy mass m' . This situation severely aggravates when integrating over the polar angle in partial wave analysis, thus collecting another logarithmic factor, cf. eqn. (1.34), which further reduces the suppression of the terms $\propto x^0$. Therefore, and to include the scale where $\sqrt{s} \lesssim m'$ in the partial-wave analysis, the full heavy propagator will be maintained below to derive realistic numerical values, while the expansion of the light propagators remains a good approximation.

However, eqn. (2.43) can be used now to derive the influence of the heavy bosons on the leading divergent terms of order $\mathcal{O}(x^1)$. This constitutes an upper limit for the capability of the W' and Z' to delay unitarity violation, because it would become a valid approximation in a regime where $m \ll m' \ll \sqrt{s} < \sqrt{s}_c$ which is practically non-existent, since the overall energy range is only ~ 1 TeV. Nonetheless, the result is obtained by plugging the ξ expansions of $C_{Z'}$ (ξ), eqn. (2.40), and of the propagator, eqn. (2.43), into the amplitude, eqn. (2.37), and expanding the resulting product in powers of x and ξ . The most divergent term, proportional to $\xi^2 x^2$, contributes to the gauge cancellation of the entire order $\mathcal{O}(x^2)$ as pointed out previously, whereas to subleading order $\mathcal{O}(\xi^0 x^1)$ only one term contributes,

$$\frac{s(t-u)}{4m^2} \left(\frac{1}{16}\xi^2\right) \left(\frac{4}{\xi^2}\right) \frac{m^2}{s} = \frac{(t-u)}{16m^2}, \quad (2.44)$$

so that the result for all kinematic channels reads:

$$\begin{aligned} \text{[Diagram 1]} + \text{[Diagram 2]} + \text{[Diagram 3]} &= (ig^2) \frac{1}{4m^2} \left[f_{a_1 a_2 b} f_{a_3 a_4 b} \times \frac{1}{4}(t-u) \right. \\ &\quad + f_{a_2 a_3 b} f_{a_4 a_1 b} \times \frac{1}{4}(s-u) \\ &\quad \left. + f_{a_2 a_4 b} f_{a_3 a_1 b} \times \frac{1}{4}(s-t) \right] + \mathcal{O}(\xi^2). \end{aligned} \quad (2.45)$$

This amplitude may now be transformed into a physically sensible basis, like it has been done several times before already, cf. sections 1.3.5 and 1.3.7: Using eqns. (1.42), (1.44), (1.49), (1.53) and (1.63) one finds

$$\mathcal{M}_{Z'}(W_L^+ W_L^- \rightarrow W_L^+ W_L^-) = -\frac{1}{4v^2} [(t-u) + (s-u)] = \frac{3}{4} \frac{u}{v^2}, \quad (2.46)$$

$$\mathcal{M}_{Z'}(W_L^- W_L^- \rightarrow W_L^- W_L^-) = \frac{3}{4} \frac{s}{v^2}, \quad (2.47)$$

and so on. Comparing with eqns. (1.43), (1.45) and (1.66), the incomplete cancellation of the divergent terms is obvious: The Z' exchange diagram cancels at most $3/4$ of the SM divergence in the limit $m \ll m' \rightarrow 0$, which corresponds to a delay of unitarity violation by a factor $\lesssim 2$, whereas the amount of this cancellation lessens when effects of realistic values for m' are collected.

Before performing a partial wave analysis, the structure of 3SHLM amplitudes with external Z^0 is briefly addressed now: For the polarization contractions the same arguments are valid here as in the SM of course, cf. section 1.3.5, and in the propagator diagrams only charged gauge bosons are exchanged because of the gauge structure of the vertices. Transferring the results for the Lorentz contractions from section 1.3.5, eqn. (1.47), the s channel amplitude then reads

$$\begin{aligned} & \text{Diagram with } W \text{ and } W' \text{ exchange} = \\ & = (ig_0^2) f_{a_1 a_2 b} f_{a_3 a_4 b} \times \left\{ \left[\frac{s(t-u)}{4m^4} \cos^2 \theta_\omega + \frac{(t-u)}{m^2} \left(1 - \frac{1}{2} \sin^2 \theta_\omega \right) + \mathcal{O}(x^0) \right] \times \right. \\ & \quad \times \left[C_W(\xi) \frac{s}{s-m^2} + C_{W'}(\xi) \frac{s}{s-m'^2} \right] + \\ & \quad \left. - \left(\frac{\sin^2 \theta_\omega}{2 \cos \theta_\omega} \right)^2 \left[\frac{s}{m^2} C_W(\xi) \frac{s}{s-m^2} + \frac{s}{m'^2} C_{W'}(\xi) \frac{s}{s-m'^2} \right] \right\}, \quad (2.48) \end{aligned}$$

where all mass-mixing coefficients have been pulled into the coefficient functions $C_V(\xi)$ again. Note that the contributions of the polarization tensors in the propagators cannot be factored out because of the different masses in

the denominator. The coefficient functions in this case read:

$$\begin{aligned} C_W(\xi) &\equiv \left[(v_W^0)^2 (v_Z^0) + \frac{1}{\xi} (v_W^1)^2 (v_Z^1) \right]^2 \\ &= c_\theta^2 - \frac{(1+4c_{2\theta}-c_{4\theta})}{8} \xi^2 + \mathcal{O}(\xi^4) , \end{aligned} \quad (2.49)$$

$$\begin{aligned} C_{W'}(\xi) &\equiv \left[(v_W^0) (v_Z^0) (v_{W'}^0) + \frac{1}{\xi} (v_W^1) (v_Z^1) (v_{W'}^1) \right]^2 \\ &= \frac{1}{16c_\theta^2} \xi^2 + \left(\frac{1}{64c_\theta^4} - \frac{1}{16} \right) \xi^4 + \mathcal{O}(\xi^4) . \end{aligned} \quad (2.50)$$

It is clear that the coefficients involved here are also orthonormal, so that the coefficient functions sum up again to leave just the external coefficients behind, completely analog to eqns. (2.41) and (2.42). Note that the leading-order term c_θ^2 of $C_W(\xi)$, eqn. (2.49), is identified with the global $\cos^2 \theta_\omega$ factor of eqn. (1.47) at order $\mathcal{O}(\xi^0)$, which is necessary to cancel all dependencies on the Weinberg angle when summing all SM-like contributions to a given charge eigenamplitude, just like the procedure in section 1.3.5. On the other hand, the c_θ^2 in the denominator of the leading order of $C_{W'}(\xi)$, eqn. (2.50), also cancels the dependency on the Weinberg angle when collecting all factors for the leading-order contribution $\propto \xi^0$ of the W' propagator, cf. eqns. (2.43) and (2.48), so that the resulting leading-order terms are exactly the same as those for $W^{1/2}$ scattering given in eqn. (2.45). One may now conclude that the cancellation of the high energy divergent leading-order terms due to heavy gauge boson exchange is always $\lesssim 3/4$ for all possible charge eigenamplitudes and hence, from eqns. (1.53) and (1.63) – (1.65), also for all isospin eigenamplitudes.

Partial Wave Expansion In order to systematize the computation of scattering amplitudes in $SU(2)_C$ isospin space and to perform a partial wave analysis, the master amplitude $\mathcal{M}(s, t, u)$ introduced in section 1.3.5, eqn. (1.53), is now assembled for the 3SHLM. Looking at the definition in eqn. (1.53) and at the corresponding kinematic contributions in eqn. (1.49), it is clear that the t and u channels of gauge boson exchange superpose to make up $\mathcal{M}(s, t, u)$. While the SM-like light propagators are expanded and subsumed to give rise to leading-order contributions as discussed in section 1.3.5, the heavy propagators are now inserted in full shape to collect the effects of large m' values in the allowed range $380 \text{ GeV} < m' < \sqrt{s_c}$ (cf. section 2.3.2 for the lower bound). Note that all propagators are plugged in together with the

leading order of the coefficient functions $C_V(\xi)$:

$$\begin{aligned} \mathcal{M}(s, t, u) &\equiv \mathcal{M}(W_L^+ W_L^- \rightarrow Z_L^0 Z_L^0) \\ &= \frac{1}{v^2} \left\{ s - \frac{1}{4m'^2} \left[t(s-u) \left(\frac{t}{t-m'^2} - 1 \right) \right. \right. \\ &\quad \left. \left. + u(s-t) \left(\frac{u}{u-m'^2} - 1 \right) \right] \right\}. \end{aligned} \quad (2.51)$$

This amplitude is valid in a regime where $m \ll \sqrt{s}$ and $m \ll m'$ but not necessarily $m'^2 < |k^2|$. Note that in this regime the most divergent order $\propto x^2$ cannot formally be cancelled yet, because to that end the first expansion term of the heavy propagators in the regime $|k^2| > m'^2$ is necessary.

Now, in order to compute the partial wave coefficients, the isospin eigenamplitudes can be assembled from the master amplitude, eqn. (2.51), using eqns. (1.63) – (1.65). The resulting expressions are then integrated according to eqn. (1.5) to obtain the partial wave amplitudes $a_L(s)$: The corresponding functions $|a_L|(\sqrt{s})$ are plotted in fig. 4 for the leading angular momenta in the three possible isospin channels up to the unitarity-violating scale where $|a_L| \gtrsim 1/2$. Moreover, setting $|a_L| = 1/2$ allows to solve for \sqrt{s}_c depending on the choice of m' . This function $\sqrt{s}_c(m')$ is also plotted in fig. 4 for the lowest contributing angular momenta of all isospin channels, and illustrates the lessening cancellation of the divergence with increasing mass parameter m' . In the limit $m' \rightarrow \infty$ the critical energy \sqrt{s}_c converges against the SM value as expected, whereas at the lower bound $m' \sim 380$ GeV it is close to its upper limit in the 3SHLM which is twice the SM value.

From fig. 4 it is clear that the s wave of the $I = 0$ isospin channel diverges most rapidly, as could be expected from the SM results (1.71) – (1.73). Hence this channel will now basically fix a theoretical upper limit on m' from the requirement that the heavy gauge bosons be light enough to affect the unitarity bound at all. An absolute upper bound on m' is therefore given by demanding that it do not exceed its own unitarity-violating energy scale, which is exactly the case for $m' = \sqrt{s}_c \sim 1.4$ TeV (cf. fig. 4). However, this would correspond to a delay of unitarity violation of merely 200 GeV compared to the SM value. In fact, the effect of the heavy gauge bosons on the critical energy scale only becomes large for light boson masses $m' < 600$ GeV, which is already in the vicinity of the experimental lower bound of 380 GeV. In this region of m' , the critical energy \sqrt{s}_c is situated between 1.8 TeV for $m' = 600$ GeV and its absolute upper limit that is possible in the 3SHLM with all experimental constraints taken into account, namely 2.1 TeV for $m' = 380$ GeV. In summary, two distinct scenarios of bounding the heavy

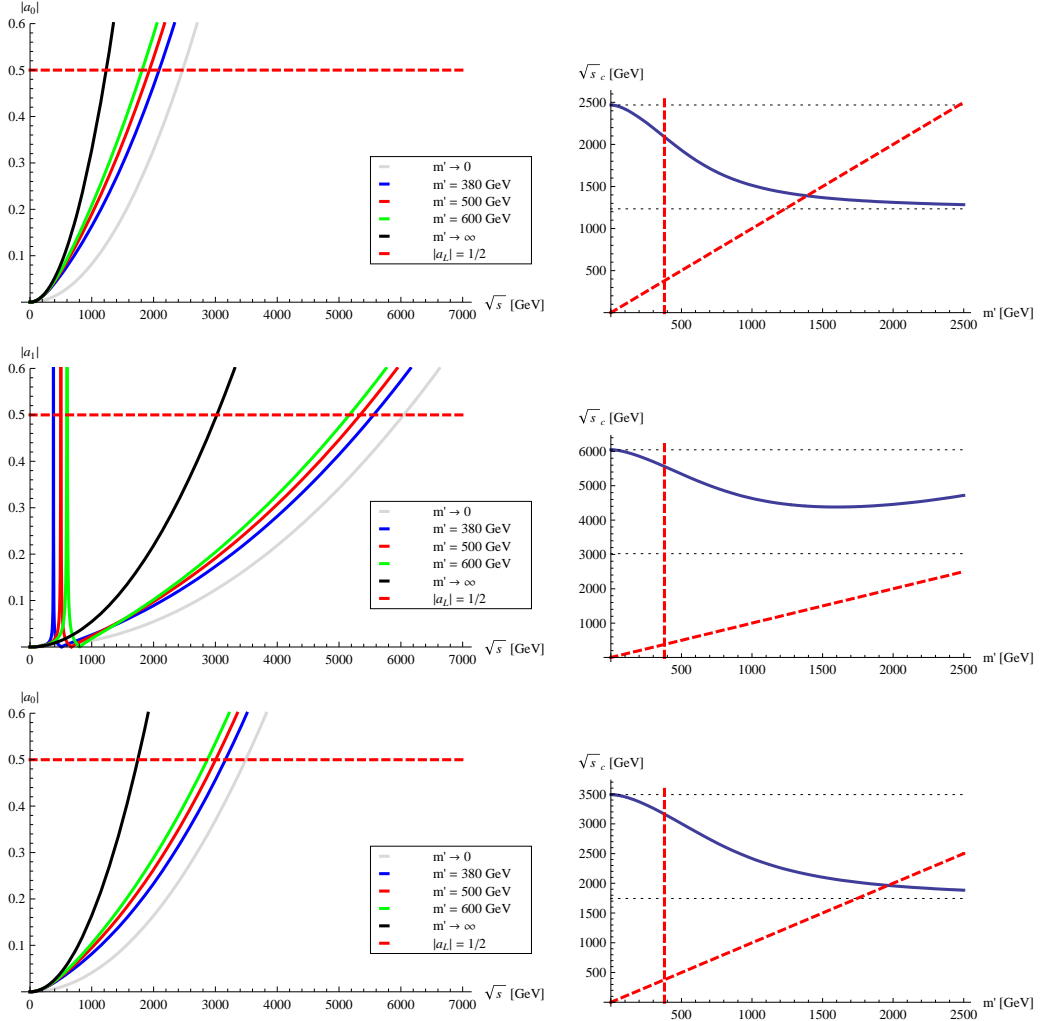


Figure 4: Divergent high energy behavior of the partial wave coefficients corresponding to the lowest contributing angular momenta in the 3SHLM, for the three isospin channels $I = 0, 1, 2$ (from top to bottom). The functions $|a_L|(\sqrt{s})$ are plotted on the left for different values of m' , where the limit $m' \rightarrow 0$ illustrates an upper limit for the possible cancellation in the 3SHLM and the limit $m' \rightarrow \infty$ corresponds to the SM result. The right side displays the corresponding functions $\sqrt{s}_c(m')$, with the red dashed lines illustrating the constraints m' , i. e. that it be heavier than 380 GeV (cf. section 2.3.2) but also lighter than its own unitarity-violating energy scale \sqrt{s}_c . The black dotted lines show the limits described above, i. e. the SM threshold as well as twice that value. Note that in the $I = 1$ channel the gauge boson resonance contributing to the lowest angular momentum $L = 1$ (center left) runs into the critical energy range above $m' \gtrsim 1.5$ TeV (center right).

gauge boson mass from above result from these considerations: The loose one is to basically demand any effect, however small, on the unitarity-violating scale at all, which corresponds to $m' \lesssim 1.4 \text{ TeV}$, whereas the tighter one is given by requiring a quantitatively significant delay of unitarity violation, which further restricts the value of m' to the vicinity of its lower bound, $m' \lesssim 600 \text{ GeV}$.

Just like the heavy gauge boson mass m' , the heavy fermion mass scale M introduced in section 2.2 is in principle also bounded from above by unitarity arguments: As pointed out in section 1.4, top pair annihilation into longitudinal gauge bosons also diverges with the CMS energy, although half an order slower in x than elastic gauge boson scattering, thus violating unitarity at $\sim 30 \text{ TeV}$. It is argued in [35] that in Higgsless 5D models such as the 3SHLM the higher KK modes of the fermions eventually contribute to t -channel bottom exchange, thereby reinstalling unitarity, at least in a continuous extra dimension. With a deconstructed dimension such as in the 3SHLM, this cancellation cannot be expected to be complete, similar to the results for elastic gauge boson scattering. Nonetheless, if such a cancellation is to take place at all, the unitarity-violating scale just given formally imposes an upper bound on the heavy fermion mass scale: $M < 30 \text{ TeV}$.

2.3.2 Experimental Bounds

Having fixed the 3SHLM to respect all the basic SM parameters such as masses, couplings and flavor phases, one remains with the parameters ϵ_L , m' and M , as described in section 2.2. Apart from the theoretical bounds presented in the previous section, the parameter space turns out to be additionally constrained by electroweak precision tests (EWPT) at LEP1 and LEP2 [38] which experimentally determine a set of variables known as the Peskin-Takeuchi precision observables S , T and U [39] (or redefined recently in [40]) with high accuracy. The original definitions of these parameters are based on loop corrections to the SM gauge boson propagators in fermionic $2 \rightarrow 2$ scattering processes, so that it is clear that any new physics contributing potentially to these amplitudes, such as new gauge couplings between SM fermions and gauge bosons as in the 3SHLM, will obtain constraints from the experimentally well-known values of S , T and U .

In a tree level analysis, it was shown [41, 42] that, in a general class of deconstructed 5D models, the contributions of new gauge factors to the precision observables can be minimized by aligning the wave functions of the SM fermions to the wave function of the charged W which is of course orthogonal to all of its KK excitations—in this case just the W' —so that the heavy modes decouple from the SM fermions: They become *fermiophobic*,

making it impossible to produce them in the s channel at the LHC. This condition reinstalls the SM-like shape of the coupling g_W of light fermions to the light W boson in very good approximation, relating m' or ξ uniquely to the delocalization parameter ϵ_L , which is why it is usually addressed as *ideal delocalization*. Looking at the fermion mass terms read from (2.30),

$$M \begin{pmatrix} \bar{\Psi}_{0,L} & \bar{\Psi}_{1,L} \end{pmatrix} \begin{pmatrix} \epsilon_L & 0 \\ 1 & \epsilon_{u/d,R} \end{pmatrix} \begin{pmatrix} \Psi_{1,R} \\ \Psi_{2,R} \end{pmatrix}, \quad (2.52)$$

one can, without explicitly solving the eigenvalue problem, check the consistency of the model by relating ϵ_L to ξ for the left-handed fermions: Given their light mass eigenstates f_L in the interaction basis,

$$f_L = v_{f_L}^0 \Psi_{0,L} + v_{f_L}^1 \Psi_{1,L}, \quad (2.53)$$

the ideal delocalization condition can be formulated as

$$g_i (v_{f_L}^i)^2 \stackrel{!}{=} g_W v_W^i, \quad i = 0, 1, \quad (2.54)$$

or, taking the ratio of sites 0 and 1,

$$\frac{g_0 (v_{f_L}^0)^2}{g_1 (v_{f_L}^1)^2} \stackrel{!}{=} \frac{v_W^0}{v_W^1}. \quad (2.55)$$

The definition of ξ (2.15) and the W coefficients (2.19) may now be plugged into this expression. Neglecting all fermion masses and hence the $\epsilon_{u/d,R}$, which is a good approximation for all flavors except for top and implies $|v_{f_L}^1/v_{f_L}^0| = \epsilon_L$ to leading order, (2.55) results in

$$\epsilon_L^2 = \frac{1}{2} \xi^2 + \mathcal{O}(\xi^4). \quad (2.56)$$

This is the leading-order relation fixing ϵ_L from m' which follows from ideal delocalization [1]. Moreover, it shows that choosing ξ small also concentrates the light left-handed fermion mass eigenstates on the 0-brane.

The heavy gauge boson mass m' itself is also constrained by EWPT: The triple gauge boson coupling g_{ZWW} may easily be calculated in the 3SHLM from the overlap of the light eigenstates of the gauge bosons on sites 0 and 1:

$$g_{ZWW} = g_0 (v_W^0)^2 v_Z^0 + g_1 (v_W^1)^2 v_Z^1, \quad (2.57)$$

whereas its deviation Δg_{ZWW} from the SM value is bounded experimentally by LEP2 [38]. After plugging in the coefficients (2.19) and (2.24) and simplifying the resulting expression, one arrives at [1]

$$\Delta g_{ZWW} = \frac{1}{8c_\theta^2} \xi^2 + \mathcal{O}(\xi^4) \stackrel{!}{<} 0.028 \quad \text{on 95 \% C.L.} \quad (2.58)$$

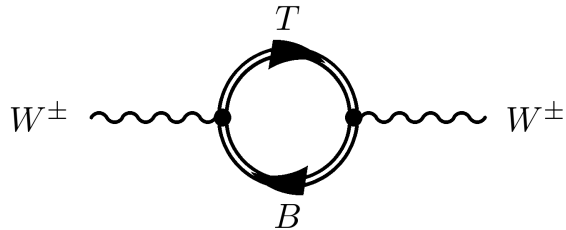


Figure 5: New contribution to αT in the 3SHLM due to the heavy isospin-violating fermion doublet (T, B) coupling to the charged SM gauge bosons W^\pm . Double fermion lines and capital letters indicate heavy mass eigenstates.

Setting $c_\theta \approx \cos \theta_\omega \approx 0.77$ to leading order, this corresponds to a lower bound of $m' \geq 380$ GeV [1].

The remaining parameter to be dealt with is the mass scale M of the heavy fermions: In this case the argument (following [1]) is a little more intricate, collecting several phenomenological constraints to cast them into a lower bound on M . For a starting point, consider the electroweak precision observable αT which is defined as the difference of the vacuum polarizations $\Pi_{aa}(p)$ with respect to the gauge components W^a of the $SU(2)_L$ gauge field in the SM [39]:

$$\begin{aligned} \alpha T &\equiv \frac{e^2}{\sin^2 \theta_\omega \cos^2 \theta_\omega m_Z^2} [\Pi_{11}(0) - \Pi_{33}(0)] \\ &= 1 - \rho \quad \text{with} \quad \rho \equiv \left(\frac{m}{\cos \theta_\omega m_Z} \right)^2 \simeq 1. \end{aligned} \quad (2.59)$$

It parametrizes the violation of the custodial symmetry mentioned in section 2.1, therefore depending on isospin-violating contributions to the vacuum polarizations such as fermion isodoublets with large mass splittings coupling to the W^\pm . In the 3SHLM, the largest new contribution of that kind clearly is the heavy Top-Bottom loop (with capital letters indicating the heavy mass eigenstates, cf. fig. 5), since the isospin-violating mass-splitting parameter $\epsilon_{t,R}$ is chosen universally in the model and is therefore fixed by the requirement to generate the large mass m_t of the SM-top. This is precisely the connection relating the two phenomenologically known quantities αT and m_t which will be used to derive a bound on M : Evaluating the (T, B) -loop diagram (fig. 5) in the limit $\epsilon_L \rightarrow 0$ (since ϵ_L respects custodial symmetry) gives [1]

$$\alpha T \approx \frac{1}{16\pi^2} \frac{\lambda_{t,R}^2 \epsilon_{t,R}^2}{v^2} = \frac{1}{16\pi^2} \frac{M^2 \epsilon_{t,R}^4}{v^2} \quad (2.60)$$

with the expected quadratic dependence [39] of αT on the isospin-violating

mass scale $\lambda_{t,R}$, cf. expr. (2.29), and the mass-splitting parameter $\epsilon_{t,R}$. On the other hand, m_t is obtained by the diagonalization of expr. (2.30), which gives [1]:

$$m_t \approx \frac{\epsilon_L \epsilon_{t,R} M}{\sqrt{1 + \epsilon_{t,R}^2}} \quad (2.61)$$

to leading order in ξ . Taking into account that $\epsilon_{t,R} < 0.67$ from phenomenological constraints on the decay $b \rightarrow s\gamma$ [1], and that ϵ_L has a small but finite value which is fixed in the ideal delocalization scheme, the combination of (2.60) and (2.61) leads to a lower bound on M between 1.8 and 2.3 TeV, depending on the Higgs mass chosen for the calculation of the phenomenological bound on αT [1].

Bearing in mind that all constraints on the model parameters pointed out so far were—except partially for the fermion mass scale M —essentially based on tree level considerations, the most remarkable result of the full one-loop analysis of the 3SHLM that was carried out recently [43] is that ideal delocalization does indeed violate EWPT. On the contrary, the precision observables exclude on 95 % C. L. an exact fermiophobicity of the heavy modes of the charged gauge bosons, thus trading the exact relation (2.56) for intervals of allowed delocalizations ϵ_L which essentially depend on the choice of the other parameters m' and M . The range of allowed delocalizations can be translated into small but non-vanishing couplings $g_{W'ff}$ of the heavy charged gauge boson W' to SM fermions as depicted in fig. 6, a circumstance which would enable its s channel production via fermionic parton-parton annihilation at the LHC: The remaining two chapters of this thesis are dedicated to a thorough study of the ATLAS detector, addressing the discovery prospects of the rather solid Z' signal as well as the discrimination of the ideally delocalized scenario from the one-loop scenario via an explicit W' search.

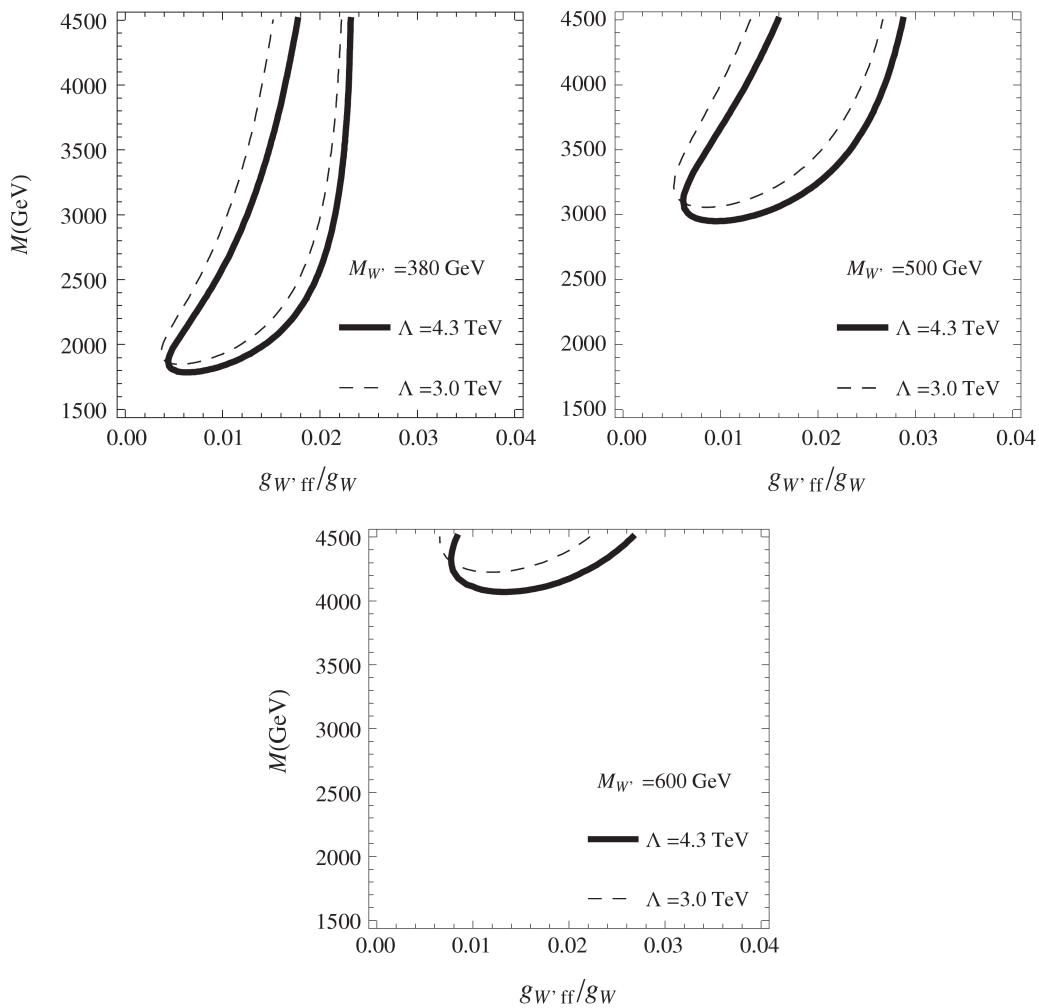


Figure 6: Allowed range of values for the W' coupling to SM fermions according to the one-loop analysis in [43]. The values were normalized to the SM coupling of W to fermions and plotted in dependence on the heavy fermion mass scale M for different gauge boson masses $m' (\equiv M_{W'})$ of 380, 500 and 600 GeV. Λ denotes the momentum cutoff taken for the loop calculations.

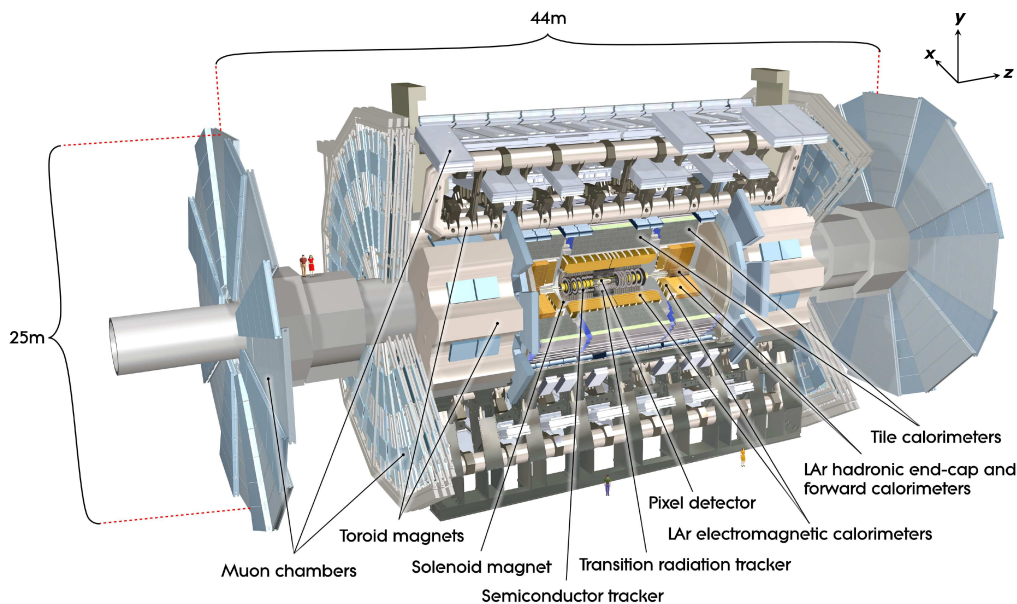


Figure 7: Three-dimensional view of the ATLAS detector [4].

3 Experiment and Simulation

3.1 The ATLAS Detector

The ATLAS detector (cf. [4, 5] for the entire section) is the largest of the four LHC experiments. In its center, single proton bunches of two oppositely directed beams collide every 25 ns at design luminosity, thereby causing hard scattering processes whose final states can be detected inside the individual detector elements. Although originally designed for CMS energies up to 14 TeV, the LHC is planned to start its first run with half the energy in November 2009, increasing the energy step by step in the succeeding runs if everything works flawless. The high collision frequency implies a tremendous amount of data output which can only be handled with a highly efficient three-stepped trigger system: In order to enable data storing, the task is to reduce the event rate from 40 MHz to ~ 200 Hz without losing interesting events.

3.1.1 Coordinate System

The ATLAS detector possesses an unambiguous coordinate system: The origin is located at the beam-crossing point. The z axis runs parallel to the proton beam, where its direction is defined in such a way that it constitutes a right-handed system with the x axis pointing to the center of the collider

ring and the y axis pointing vertically upward (cf. coordinate axes in fig. 7). Based on this cartesian coordinate system, solid angles are specified in spherical coordinates (φ, θ) , where φ denotes the azimuth angle in the x - y plane with respect to the x axis. The polar angle θ with respect to the z axis is usually converted into the so-called pseudorapidity

$$\eta \equiv -\ln\left(\tan\frac{\theta}{2}\right), \quad (3.1)$$

which is at relativistic energies, i. e. negligible masses, in good approximation equal to the rapidity

$$\frac{1}{2}\ln\left(\frac{E+p_z}{E-p_z}\right), \quad (3.2)$$

where E is the energy of the particle and p_z is the z component of its 3-momentum. This quantity is invariant under Lorentz boosts along the z axis, so that any direction given by (φ, η) is also approximately invariant with respect to the choice of one of these inertial frames [44]. Moreover, using these direction variables, an invariant measure can be defined for the solid angle ΔR enclosed by two particle trajectories:

$$\Delta R \equiv \sqrt{(\Delta\eta)^2 + (\Delta\varphi)^2}. \quad (3.3)$$

This solid angle definition is used in the analysis of ATLAS data, e. g. to evaluate the angular separation of single particles inside a boosted bunch, or to retrieve the energy deposition in the calorimeters (section 3.1.3) along a specific particle trajectory.

3.1.2 Inner Detector

The inner detector (ID), fig. 8, directly surrounds the beam-pipe (36 mm in diameter) and consists of three shells which are traversed by the high-energetic particles almost without any energy deposition. However, combining the single interaction points allows for the determination of the particle trajectory and, in combination with a magnetic field, also of the transverse momentum p_T , defined as the 3-momentum projection onto the x - y plane, and the charge sign of electromagnetically charged particles.

The innermost shell is formed by the three-layered silicon pixel detector with a resolution of $60\ \mu\text{m}$ along the z axis and $12\ \mu\text{m}$ in the x - y plane. This shell is enclosed by eight layers of silicon microstrip trackers with a resolution of $600\ \mu\text{m}$ along the z axis and $20\ \mu\text{m}$ in the x - y plane, and eventually by the transition radiation tracker, which enables a distinction between electrons and pions and possesses a resolution of $170\ \mu\text{m}$ in the x - y plane. The

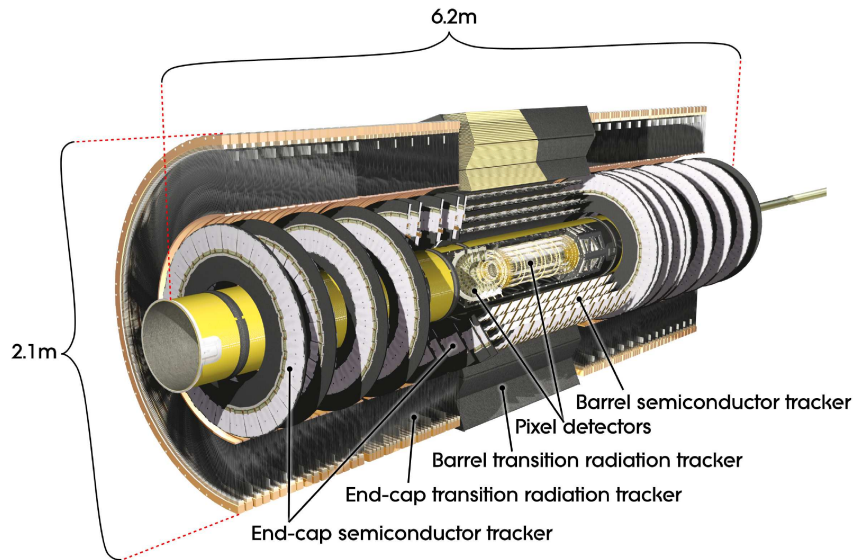


Figure 8: 3D view of the inner detector [5].

entire inner detector is coated by a superconducting magnetic field coil (the solenoid magnet in fig. 7), which generates a magnetic field with ~ 2 T in the z direction, so that the transverse momentum p_T and the charge sign of a particle can be determined from the curvature of its measured trajectory. The overall dimensions of the inner detector are 2 m in diameter and 7 m in length, where the overall angular coverage is $|\eta| < 2.5$, with $|\eta| < 2.0$ covered by the barrel and the rest covered by the end-caps which consist of a similar sequence of detector layers as the barrel itself.

3.1.3 Calorimeters

The solenoid magnet is surrounded, from inside to outside, by the electromagnetic calorimeter (ECal) and the hadronic calorimeter (HCal), cf. figs. 7 and 9, where most of the particles emerging from high-energy collisions lose their entire energy. Both ECal and HCal are so-called sampling calorimeters, i. e. they are composed of alternating layers of absorbing and active material. The incoming particles interact with the absorber, thus forming showers of new particles, so that the energy which is thereby deposited in the absorbing medium is determined by measuring the electromagnetic charge occurring in each subsequent layer of active medium. To enable a three-dimensionally resolved measurement, all calorimeters are divided up into separate cells of different sizes and shapes, depending on the region of the calorimeter. Note that the two-medium systems of the barrel calorimeters are arranged in a

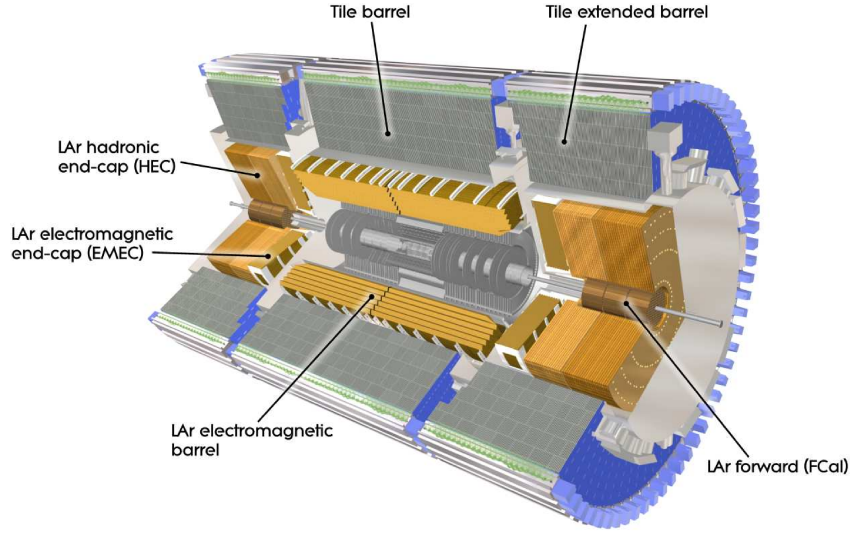


Figure 9: 3D view of the calorimeter system, including ECal (electromagnetic barrel and end-cap) and HCal (tile barrels and HEC) [5].

radial accordion geometry instead of alternating tube shells which facilitates the cabling of every single layer from outside the calorimeters.

The barrel and end-caps of the ECal consist of absorbing lead layers with an overall thickness of 24 interaction lengths, where mostly electrons and photons interact electromagnetically, and of active layers made of liquid argon (LAr). The expected fractional accuracy of energy measurement is roughly $\Delta E/E = 10\%/\sqrt{E/\text{GeV}}$. For the barrel of the HCal steel layers with an overall thickness of 11 interaction lengths are used as absorber and plastic scintillators form the active layers, whereas the end-caps comprise a copper/LAr system. The HCal is where the jets of hadronic particles, which emerge from hard partons via hadronization and mostly traverse the ECal because of the large masses (bremsstrahlung is $\propto 1/m^2$), deposit their energy via strong interactions with the absorber medium. The energy resolution of the HCal is estimatedly $\Delta E/E = 50 - 100\%/\sqrt{E/\text{GeV}}$. The overall dimensions of the calorimeters are 4 m in diameter and 12 m in length, with an overall angular coverage, including end-caps, of $|\eta| < 3.2$ for the ECal and $|\eta| < 4.9$ for the HCal.

3.1.4 Muon Spectrometer

In the SM there are basically only two kinds of particles which can traverse all detector layers including the HCal: neutrinos and muons. The neutrinos exclusively interact weakly and therefore only appear in collision events as

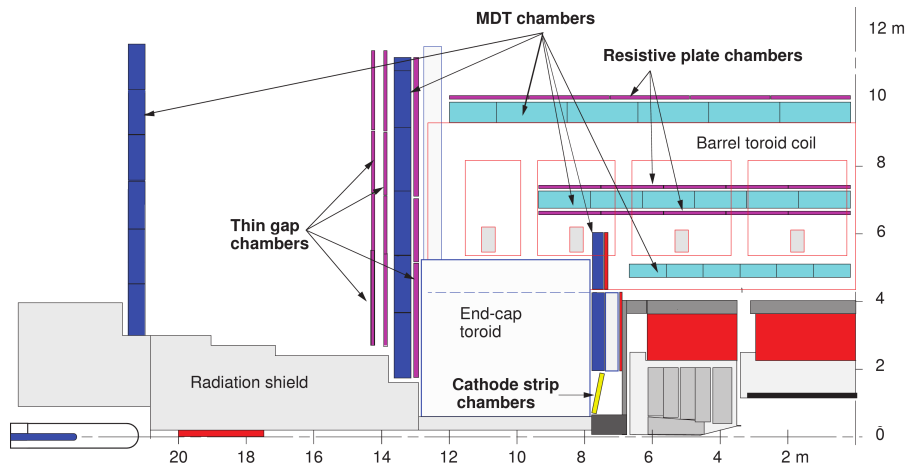


Figure 10: The ATLAS muon spectrometer [5].

missing transverse momentum, whereas the muons, which traverse all inner detectors because of their long lifetime and large mass while interacting only electroweakly, are detected by another separate stand-alone detector system surrounding the calorimeter, the muon spectrometer (cf. figs. 7 and 10). It is majorly built up of monitored drift tube chambers (MDT) for tracking and different types of trigger chambers, namely resistive plate chambers (RPC) in the barrel and thin gap chambers (TGC) in the end-cap regions, cf. fig. 10). Moreover, both the barrel and the end-cap region contain eight superconducting magnetic field coils each, which generate a toroidal magnetic field with roughly 0.4 T, so that the transverse momentum can be measured from the curvature of the muon trajectory in the η - z plane.

Every MDT chamber contains from 96 to 432 drift tubes with a diameter of 3 cm each, whereas the entire spectrometer is composed of three MDT layers in the barrel as well as the end-cap region. The drift tubes work in principle like a Geiger-Müller tube: They are filled with an Ar/CO₂ compound gas which is ionized by traversing muons, so that the anode wire in the center of the tube can detect the avalanche resulting from the high electrostatic potential between wire and tube shell. The time interval between the collision moment (known from the LHC frequency) and the drift tube signal is then converted into a closest radial distance between the muon trajectory and the anode wire via an empirically known x - t relation, so that the combination of different drift tube signals allows for the reconstruction of the trajectory in the η - z plane with a resolution of 50 μ m (cf. fig. 11). In order to attain this accuracy, the distortions and relative positions of the MDT are measured with a laser-based optical system and included real-time

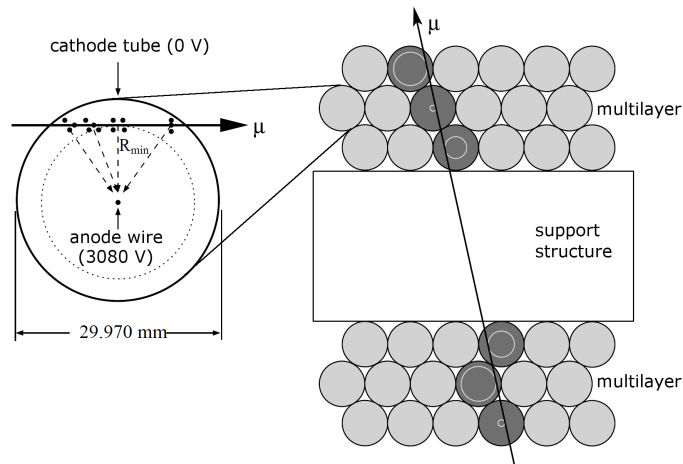


Figure 11: Cross section of a single MDT drift tube (left, [4]) and of an entire MDT consisting of two multilayers enclosing a central support structure (right, [45]). Furthermore, the principle of track reconstruction based on the determination of minimal radii in several drift tubes is illustrated.

into track reconstruction (so-called alignment). Only in the extreme forward regions are the MDT replaced by cathode strip chambers (CSC), because the event rate is too large there for the dimensions of the MDT drift tubes.

Since the MDT principle is based on the precise measurement of time delays which are in general larger than the time gaps between collisions, an additional trigger system is needed to assign MDT data to specific collision events: The RPC are composed of two parallel Bakelite plates with a gas-filled spacing of 2 mm, where a traversing muon causes ionization which is again amplified by a potential between the plates. Both plates are lined with metal strips, one in η direction and the other in φ direction, so that the capacity change between single strips due to the avalanches allows for position-resolved triggering and conveys φ information on which the MDT are not sensitive.

3.2 The Data Simulation Chain

3.2.1 Production of Monte Carlo Events

Since a collider detector like ATLAS is an extremely complex technical device, it is indispensable to get a theoretical grip on the physics input in order to simulate and understand the according detector response. For a given high-energy process, the essential tasks are [46] to find the complete Feynman amplitude, eqn. (1.3), up to a specific order, absolute-square it and

perform the phase-space integration in order to get differential cross-sections and finally generate event samples with correctly distributed final-state kinematics. The actual challenge is to systematically find all contributing diagrams (which grow exponentially with the number of final-state particles) while avoiding double-counting, and to numerically integrate the squared matrix element within a realistic time interval. Whereas different approaches are made by various matrix-element generators to determine the Feynman amplitude, a very powerful and therefore commonly used tool exists for the subsequent phase space integration, the Monte Carlo (MC) method: In principle the idea is to generate random sets of phase-space points and according amplitude values and see if they are below or above the actual integrand at the given point. This is repeated several times while counting the number of hits below the integrand, so that finally the hit count can be compared with the overall number of attempts to get the integral value. A huge time-saver in this procedure is to adapt the probability distribution of the random points according to the resonant regions of the amplitude rather than taking uniformly distributed points. In summary, there exists a large variety of MC generators with different implementations of matrix-element generators and phase-space integrators, and various included physics models such as the SM of course, and some of its extensions.

In section 2.3.2 it was argued that in the 3SHLM ideal delocalization is necessary at tree level to account for the EWPT, which implies vanishing couplings of the W' and small couplings of the Z' ($\mathcal{O}(10^{-2})$) to SM fermions [1], whereas at one-loop order ideal delocalization is excluded so that also the W' ought to have small but finite couplings to the SM fermions in order to respect EWPT [43]. The implied possibility to produce both heavy gauge bosons in the s channel at the LHC via quark-antiquark annihilation (cf. fig. 12) leads to a rather unique phenomenology of solely one charged and one neutral heavy vector resonance in the LHC-relevant energy range below 1 TeV. This gave rise to the implementation [6] of the 3SHLM into the parton level MC generator WHIZARD [7] with the matrix element generator O'Mega [47] in order to get a first, parton-level based clue of the discovery potential of the heavy resonances at the LHC [6]. One of the goals of this thesis is to perform a full ATLAS detector simulation of W' and Z' signal and background samples in order to verify the results of [6] with more realistic data. A cursory outline for an analysis addressing ATLAS detector signatures of heavy gauge bosons decaying into SM bosons can be found in [3], although with the phenomenologically critical assumption of SM-like couplings of the heavy gauge bosons. Nonetheless, the final states discussed in [3] correspond to some of those to be introduced in the further course of this section.

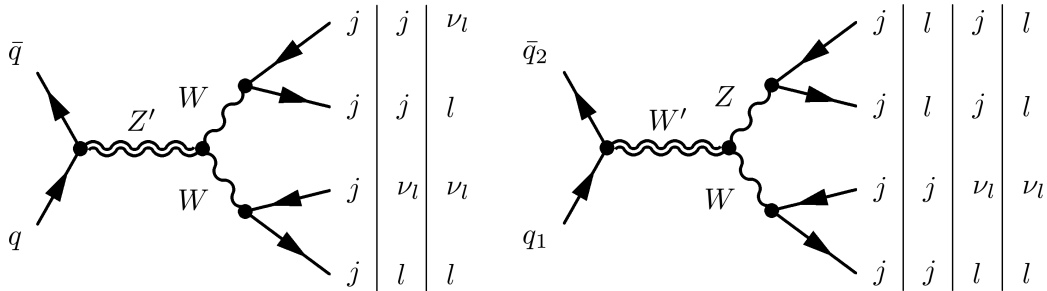


Figure 12: Dominating class of diagrams for the production and subsequent decay of the Z' (left) and the W' (right) at the LHC. For the resulting four-fermion state, the various possible detector signatures are listed, to be read in columns with each column denoting a separate final-state signature. The label j stands for quarks on parton level, which will hadronize to form physical hadron jets in the detector, and the label l denotes the light charged leptons e and μ , where the explicit distinction of anti-particles is suppressed in the notation.

Final State Signatures Since the W' is almost fermiophobic, its decay into SM fermions is strongly suppressed so that it dominantly decays into SM gauge bosons, $W' \rightarrow WZ$. Although the Z' has a much more robust coupling to SM fermions than the W' , its decay into SM gauge bosons, $Z' \rightarrow WW$, strongly dominates nevertheless because of the decay of the longitudinal mode [6]. Finally, the SM gauge bosons decay into SM fermions as usual, thus giving rise to four-fermion final states with very similar shapes for W' and Z' (cf. fig. 12 for a summary of all possible final-state signatures for each boson).

When determining the final states to be analyzed, the total cross sections of the signal have to be weighed up against the corresponding background cross sections in order to maximize the signal significance. From this point of view, the purely hadronic final state $jjjj$ is not included in the analysis despite its very large cross section due to the huge QCD background and poor discriminative power [6]. On the other hand, the purely leptonic final states have very clean signatures but comparably small cross sections due to the lack of color multiplicity. Moreover, the neutrinos escape detection and hence only appear as missing transverse momentum in the event, so that their 4-momentum cannot be uniquely determined, cf. section 4.1.4. This gives rise to the exclusion of the leptonic final state $l\nu l\nu$ of the Z' because of the two neutrinos, whereas the W' decay channel $l\nu ll$ lacks only one scalar information while constituting a very clean signature of the W' , so that it is included in the analysis. Finally, the semi-leptonic final states can

be distinguished between $lljj$ with two charged leptons, which unanimously reflects the decay of a W' , and $l\nu jj$ with one charged lepton and missing transverse momentum, which contains an inherent ambivalence with respect to the original heavy gauge boson: Bearing in mind the fact that the heavy gauge boson masses are almost degenerate, cf. eqn. (2.26), the only way to disentangle the two heavy resonances in this channel is to distinguish the resonances of the SM gauge bosons in the two final-state jets (cf. fig. 12). A statistical approach to achieve this task is presented in section 4.2. To sum up, the final states of the heavy gauge bosons with the highest discovery potential, which are therefore considered in the following data analysis, are $l\nu jj$ for the Z' and $lljj$, $l\nu ll$ as well as $l\nu jj$ for the W' .

Signal In order to simulate proton-proton collisions with WHIZARD, one first has to define a proton as a set of colored elementary particles, commonly subsumed as partons, and to convey the internal kinematics in the form of empirically known parton distribution functions (PDF) for the proton. For all samples produced for this thesis, the proton is defined as the set of all first-generation quarks and anti-quarks plus the gluon,

$$p \equiv \{u, \bar{u}, d, \bar{d}, g\} , \quad (3.4)$$

with the CMS energy of the colliding protons set to the original LHC design value of 14 TeV as in the parton level study [6]. The final states are defined as the sum of all allowed combinations for

$$\begin{aligned} j &= \{u, \bar{u}, d, \bar{d}, s, \bar{s}, c, \bar{c}, b, \bar{b}\} , \\ l &= \{e, \bar{e}, \mu, \bar{\mu}\} \end{aligned} \quad (3.5)$$

and the corresponding neutrino flavors, with the CKM matrix set to unity. Note that $j = b (\bar{b})$ contributes to the signal in the $l\nu jj$ channel but only to the background in the $lljj$ channel, because top-bottom decay of a W is basically excluded on kinematic grounds. For parton kinematics WHIZARD was linked against the CTEQ6 PDF library [48] in the \overline{MS} scheme, whereas the resulting cross sections were checked with other PDF sets, namely the MRST2004 NLO [49] and the CTEQ6 LO, which are all in agreement up to relative variations $\lesssim 10\%$ (cf. table 1).

In order to reduce background and restrict the number of events to be generated, following [6] the kinematic cuts were set at generator level for both signal and background as follows:

$$\begin{aligned} p_T &\geq 50 \text{ GeV} , \\ |\eta| &\leq 3.0 \end{aligned} \quad (3.6)$$

final state	cross sections		
	CTEQ6 \overline{MS} [fb]	MRST2004 NLO	CTEQ6 LO
$e\nu j_1 j_1$	332.5 (7)	+2.73 (1) %	-7.58 (2) %
$\mu\nu j_2 j_2$	218.3 (4)	+2.75 (1) %	-6.60 (2) %
$\mu\nu j_1 g$	2591 (6)	+0.888 (3) %	-5.02 (2) %
$\mu\nu g g$	529 (1)	+4.16 (1) %	-3.78 (1) %

Table 1: Total cross sections for several parton-level final states (jet indices denoting the quark generation) in the phase space region specified by eqns. (3.6) – (3.8), which were computed with WHIZARD using different parton distribution functions for initial kinematics.

for all final-state particles. To avoid infrared singularities, a cut on minimal x was applied for the incoming partons,

$$x \geq 1.4 \times 10^{-3}, \quad (3.7)$$

where x is the usual PDF notation for the momentum fraction carried by a single parton with respect to the overall momentum of the proton. Moreover, in order to further restrict phase space to the signal-relevant regions, a cut was applied on the invariant mass of the two partons in the semi-leptonic final states:

$$\begin{aligned} 50 \text{ GeV} &\leq m_{jj} \leq 120 \text{ GeV} && \text{for } l\nu jj, \\ 50 \text{ GeV} &\leq m_{jj} \leq 110 \text{ GeV} && \text{for } lljj. \end{aligned} \quad (3.8)$$

In this basic setup, signal samples were generated with a number of events corresponding to an integrated luminosity $\mathcal{L} = 100 \text{ fb}^{-1}$, according to the total cross sections determined by WHIZARD during phase space integration. In order to account for the fact that the heavy gauge boson mass is a free parameter of the 3SHLM, the complete signal was generated in all final states for $m' = 380 \text{ GeV}$ and 500 GeV with a bulk mass $M = 3.5 \text{ TeV}$, and for $m' = 600 \text{ GeV}$ with $M = 4.3 \text{ TeV}$, in each case with corresponding maximal couplings $g_{W'ff}$ of the W' to SM fermions according to the one-loop results of [43]. Moreover, the signal was additionally generated in the ideally delocalized scenario of [1] for $m' = 500 \text{ GeV}$, in order to cross-check the W' searches in the one-loop scenario against the case of vanishing $g_{W'ff}$.

Backgrounds As a first step, the background is classified into reducible and irreducible backgrounds: The irreducible background is the sum of all diagrams producing identical parton-level final states as the signal and therefore interfering with it. Hence this background has to be generated by re-running the signal final states within the SM to truly separate it from signal contributions. On the other hand, the reducible background is made up of all contributions producing the same final-state signature on detector level. Due to the ambiguity of hadron jets in the detector, this background is greatly dominated by QCD processes producing hard partons on matrix-element level. The straightforward approach to account for this background is to replace one or two of the quark jets in the signal final states by a gluon [6]. Note that when putting just one gluon into a semi-leptonic final state, the remaining quark jet is restricted to the first generation due to the definition of the proton, eqn. (3.4), and flavor conservation. Both reducible and irreducible backgrounds were generated with the same generator cuts as the signal, cf. eqns. (3.6) – (3.8), with sample sizes corresponding to $\mathcal{L} = 100 \text{ fb}^{-1}$ for $l\nu jj$, 500 fb^{-1} for $lljj$, and 10^3 fb^{-1} for $l\nu ll$, where the luminosity was increased and the background scaled down to 100 fb^{-1} afterwards for the channels with small cross sections in order to reduce background fluctuations.

However, since jet reconstruction from detector data is a rather complex procedure depending on some algorithms and free parameters, cf. section 4.1.3, it is certainly not a matter of course that two hard partons on matrix-element level are recognized as exactly two hard jets in the detector. For example, due to parton showering, cf. section 3.2.2, it is possible that one hard parton produces two or more hard jets within a very restricted angular cone in the detector, i. e. three-particle final states with one parton may readily produce detector signatures which fulfill the cutting restrictions for the signal search. This is accounted for by generating three-particle final state samples with one gluon or first-generation quark. Their impact on the heavy gauge boson search will only become obvious at the end of the simulation chain, when it is clear how many events are reconstructed with two hard jets in the detector instead of just one. For parton-level generation, the usual kinematic cuts, eqn. (3.6), were applied for all final-state particles, as well as a rather loose back-to-back cut between the directions of the parton and the boosted leptons coming from the decay of an SM gauge boson,

$$\Delta R(j, W(Z)) \geq 1.8, \quad (3.9)$$

thus restricting the phase space to the region which produces dangerous four-particle final states on detector level, since in the signal the parton pair and the lepton pair each emerge from SM gauge bosons which are boosted in

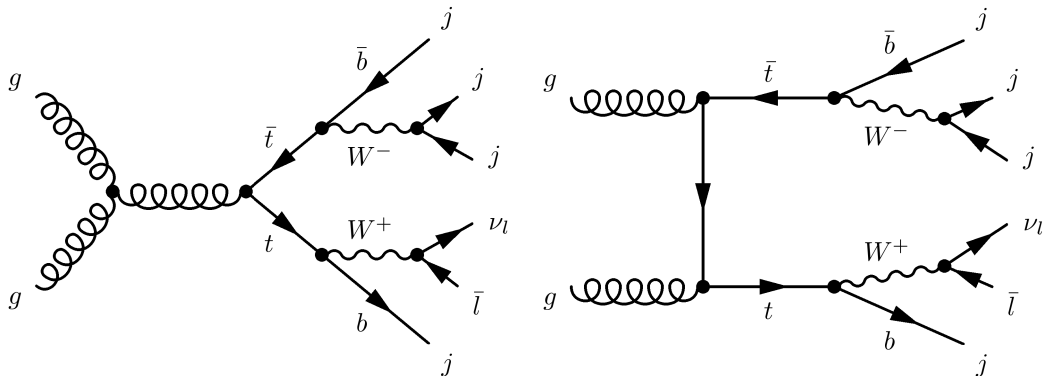


Figure 13: $t\bar{t}$ production via gluon-gluon scattering, which is dominant ($\sim 90\%$) at the LHC [5], and subsequent semi-leptonic decay via W bosons.

opposite directions from the decay of the heavy gauge boson. The final states were generated in samples corresponding to $\mathcal{L} = 20 \text{ fb}^{-1}$ for $l\nu j$ and 100 fb^{-1} for llj and scaled up for $l\nu j$ afterwards because of the huge cross sections to be coped with for this kind of three-particle final states. Note that the fraction of events which contribute to the signal search potentially depends on the definition of the splitting parameter PYTHIA [30] uses for the parton shower (cf. section 3.2.2), whereas the PYTHIA default definition used here is most likely to produce QCD final state radiation [30], so that the samples produced here may be seen as an upper limit for the background contribution of these final states. Nonetheless, in order to estimate the size of this dependence, a small part of the entire sample was showered with the most restrictive definition of the splitting parameter with respect to final state radiation before performing the detector simulation. It turns out that the fraction of events which are reconstructed with two jets on detector level lies between 12.9(2) % with the most restrictive definition and 20.17(7) % with the default definition of the splitting parameter in PYTHIA. Hence the mean background contribution to the di-jet signature of the signal is 16.5(2) % of the entire cross section of the parton-level final states $l\nu j$ and llj , with a systematic uncertainty of 22(1) %.

On the other hand, just like splitting a hard parton into two boosted detector jets, it is also possible that two strongly boosted hard partons are merged into one jet at detector level. Although this circumstance is not fully accounted for in this analysis, its potential influence is estimated in the following way: Five-particle final states with three partons have very poor cross sections for the kinematic topology considered in the signal, and are thus neglected for the background, whereas the most dangerous six-particle final state with four partons and two leptons emerges from top pair production,

because it has a large cross section at LHC energies and the semi-leptonic decay via two W bosons is kinematically very similar to the $l\nu jj$ signal channel if two or more boosted jets are merged together in the detector (cf. fig. 13). Therefore $t\bar{t}$ production with semileptonic final states on parton level is generated in samples of $\mathcal{L} = 100 \text{ fb}^{-1}$ and included into the analysis.

3.2.2 Parton Shower and Fragmentation

It was already mentioned several times now that, due to the confinement property of the strong interaction at low energies or large distances, colored particles which are produced on matrix element level in hard scattering processes undergo a highly non-trivial evolution until they finally end up in jets consisting of hundreds of boosted color-neutral hadrons.

The first step to get a theoretical handle on this behavior is the factorization theorem of QCD saying that QCD final state processes at energies below the scale of the hard process can be factored out of the hard matrix element in good approximation. Thus QCD final state radiation can be separated from the hard matrix element and evaluated perturbatively in the QCD coupling constant, where it turns out that the emission of collinear and soft gluons are the most likely processes. Hence the energy regime can be lowered in parton-showering cascades from $\sim 1 \text{ TeV}$ for the hard matrix element down to the confinement scale $\sim 1 \text{ GeV}$, which is where the QCD coupling constant becomes of $\mathcal{O}(1)$ so that the perturbation expansion breaks down. The final step of theoretical jet-building is therefore the so-called fragmentation or hadronization, i. e. the formation of color-neutral hadronic bound states from the parton shower at the confinement scale. There are several models describing this procedure which are implemented in different MC generators, such as the Lund string model included in PYTHIA [30] or the cluster fragmentation model of HERWIG [50] (cf. [46] for this paragraph).

Since version 1 of WHIZARD, which was used for data production in this thesis, is a pure parton level MC generator, it is mandatory to reprocess its output with another MC generator that is capable of parton showering and hadronization. The standard procedure for the ATLAS detector simulation of WHIZARD events as described in [10] is to convert the WHIZARD data into the highly compatible *Les Houches Accord* (LHA) event format [51] and to reprocess them with PYTHIA. This generator is a fully integrated part of the ATLAS data production chain and hence produces hadronized truth level events in the pool format which is commonly used within the ATLAS software framework ATHENA [10].

3.2.3 Detector Simulation

Once fully hadronized truth level samples are available, the remaining task is to simulate the detector response of each collision event. To that end ATHENA contains a detector simulation chain comprising several steps to transform the event samples from truth level to reconstruction (reco) level [8, 10]: The first one is the actual detector simulation, i. e. the physical interactions of all particles in the event with the different kinds of matter inside the various detector parts. This is done by the GEANT4 software toolkit [52], which produces so-called GEANT4 hits of the particles inside the detector parts. In the following digitization step these hits are converted into raw detector data like currents and voltages which exactly correspond to the future ATLAS output in real LHC runs. The last step of the chain, which is common to simulated and real detector data, is the reconstruction of actual particle tracks from the raw detector data and finally the creation of ESD and AOD files which are the standard ATHENA bookkeeping formats for reconstructed detector events, where the AOD format is just a compact summary of ESD. The actual analysis programs for truth and reco data make extensive use of the C++ data analysis framework ROOT [53], running on the data samples in its internal n-tuple file format which can be obtained within ATHENA from the PYTHIA output on truth level and from the AOD files on reco level.

The full simulation chain as described above takes roughly six minutes per event for the transformation from truth to reco level, which would add up to tremendous amounts of simulation time for the samples considered here, especially in the $l\nu jj$ channel: For example, the 100 fb^{-1} of signal and irreducible background in this channel correspond to nearly $6 \cdot 10^4$ events for each lepton flavor, and the the sum of all reducible backgrounds is even larger by one order of magnitude, so that, apart from making use of the possibility of highly parallel processing on the CERN Computing Grid [10], the fast detector simulation ATLFAST-2 [9, 10] of ATHENA release 14.5.0 was utilized. It takes less than one minute per event, thus reducing the computing time on each Grid node by a factor 6 at least, which is achieved majorly by using full simulation results to speed up the very complex calorimeter simulation.

Nonetheless, in order to validate the ATLFAST-2 samples against the full simulation, $2 \cdot 10^4$ events were fully simulated for each lepton flavor of the $l\nu jj$ signal. Since ATLFAST-2 saves time first and foremost during calorimeter simulation, it suggests itself to compare observables which are closely related to calorimeter measurements such as the kinematic quantities p_T , η and φ of jets and electrons as well as missing transverse momentum and muon isolation, cf. fig. 14 as well as figs. 36 and 37 in appendix C for respective

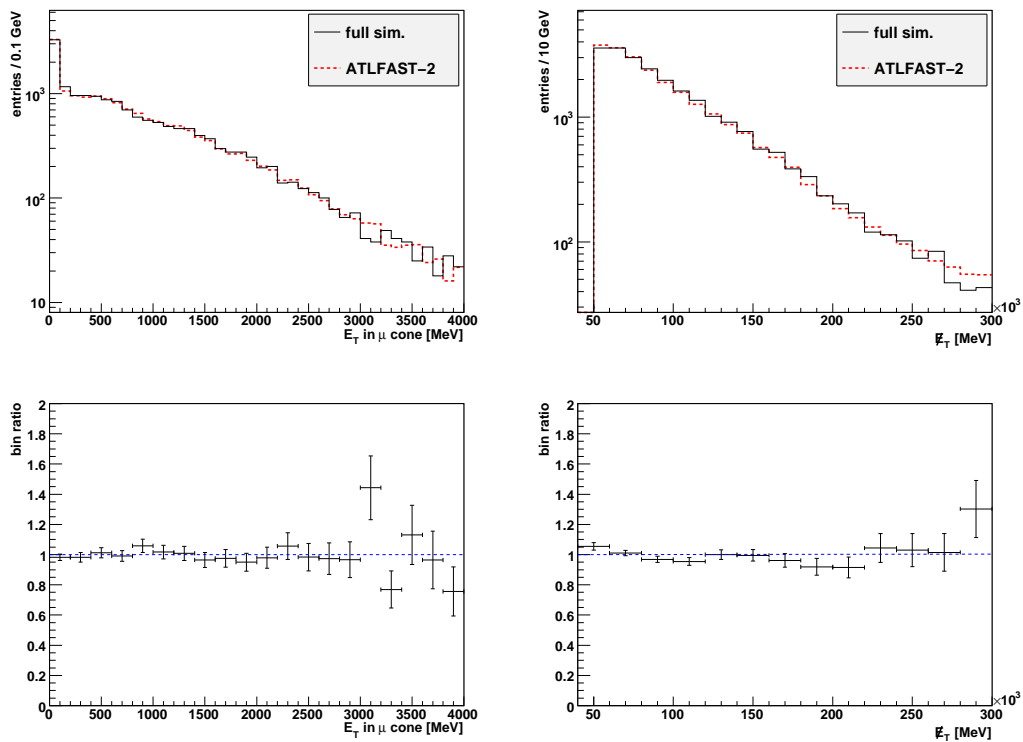


Figure 14: Comparison of observables which depend on calorimeter data in fully simulated and ATLFAS-2 samples. The left side shows the deposition of transverse energy inside an angular cone of size $\Delta R = 0.2$ around the muons, while the missing transverse momentum is displayed on the right. The upper histogram shows absolute distributions (with ATLFAS-2 data normalized to full sim. data with fewer statistics) and the lower one shows the bin ratios. Generally, the results are in good agreement.

plots. As expected, the ATLFAST-2 and full simulation samples are in solid agreement, so that the utilization of ATLFAST-2 results for all other samples in this analysis is justified. Note here that for the entire analysis of simulated detector data the loosest kinematic cuts are set to

$$\begin{aligned} p_T &\geq 50 \text{ GeV} , \\ |\eta| &\leq 2.5 , \end{aligned} \tag{3.10}$$

i. e. the same p_T cut and a tighter η cut compared to the generation cuts, eqn. (3.6), to account for potential particle scattering into regions with smaller η inside the detector.

3.2.4 Comparison with Validated Data

Although the official ATLAS policy is to use centrally validated background samples for all analyses, that was impossible in this case, because the statistics of all existing validated background samples with the relevant final states is by far not enough to account for the required luminosity in the high-energetic cut region of this analysis, so that it was necessary to produce all backgrounds privately as described above. However, the existing samples are used to cross-check the basic approach of this analysis to encompass the fully inclusive background for the semi-leptonic final state signatures considered. This is done on truth level in order to focus on the MC generation, parton showering and fragmentation steps of the data production chain, which is justified because only centrally available default job transformation scripts have been used to simulate and reconstruct the privately produced hadronized truth data.

The basic claim of the background production procedure described in the course of this chapter is to fully account for the inclusive SM background for two hard jets plus a gauge boson decaying into two leptons. However, since gauge couplings and lepton flavors are universal at generator level, the validation procedure carried out here is restricted to the case of a Z boson decaying into two muons for simplicity, assuming that the results will also hold for other flavors as well as charged bosons. The approach is to use WHIZARD and PYTHIA, following the procedure described in sections 3.2.1 and 3.2.2, to generate sufficient statistics of truth level data within the loose kinematic cut region of the validated sample. After that, the fraction of events which contain exactly two jets passing the kinematic cuts

$$p_T \geq 15 \text{ GeV} \quad \text{and} \quad |\eta| \leq 2.5 \tag{3.11}$$

and two muons passing the same kinematic cuts and an invariant mass cut

$$82 \text{ GeV} < m_{\mu\mu} < 100 \text{ GeV} \tag{3.12}$$

	WHIZARD + PYTHIA					SHERPA
	$\mu\mu jj$	$\mu\mu j_1 g$	$\mu\mu gg$	$\mu\mu j_1$	$\mu\mu g$	
$\sigma_{\text{prod}} \times \Phi_{\text{cut}} [\text{pb}]$	19.94	74.93	18.83	104.3	64.41	
	282.4					1591
efficiency [%]	24.89					4.351
$\sigma_{\text{eff}} [\text{pb}]$	70.29					69.19

Table 2: Production cross sections times generator cut efficiencies (for SHERPA also times multi-lepton filter efficiency of 78.94 %), event selection efficiencies for the requirement of exactly two muons and two jets passing the cuts (3.11) and (3.12), and resulting effective cross sections for the relevant final state.

is computed both in the privately produced and in the official sample. The event selection efficiencies thus determined are then multiplied with the total cross sections of the original samples in order to compare the effective cross sections which contribute to the relevant final state signature.

The official sample used for this procedure is the fully inclusive SM background for $Z \rightarrow \mu\mu$ plus zero to three hadron jets with 14 TeV CMS energy, which is available at [54]. The sample contains $2 \cdot 10^6$ events and was generated, showered and hadronized with the MC generator SHERPA [55], applying merely an invariant mass cut

$$m_{\mu\mu} > 60 \text{ GeV} \quad (3.13)$$

on the leptons at generator level. The corresponding total production cross section (QCD up to NNLO) times branching ratio is given as

$$\sigma_{\text{prod}} \times \mathcal{B}(Z \rightarrow \mu\mu) = 2015 \text{ pb} , \quad (3.14)$$

whereas an additional multi-lepton filter requiring at least one muon within the kinematic cuts

$$p_T \geq 15 \text{ GeV} \quad \text{and} \quad |\eta| \leq 2.7 , \quad (3.15)$$

with an efficiency of 78.94 %, has been applied after generation.

In order to compare this sample with private production, all processes contributing to the irreducible and reducible backgrounds of the $\mu\mu jj$ final state have been generated with an identical invariant mass cut (3.13)

on the muons and the kinematic cuts (3.15) on both leptons and one or two partons at generator level, which merely increases the event selection efficiency compared to the SHERPA sample. All relevant numbers such as cross sections and event selection efficiencies as well as the final comparison of the effective cross sections obtained from the SHERPA sample and the WHIZARD/PYTHIA sample are summarized in table 2, illustrating a very good quantitative agreement between the two production methods. Bearing in mind that the cross section given for the SHERPA sample already includes NNLO corrections, whereas the WHIZARD values are all LO, the result in table 2 implies that the privately produced background rather tends to be too large than too small.

Furthermore, the distributions of the kinematic observables p_T and η of the jets and muons as well as the Z resonance in the invariant masses of the two muons are compared in fig. 15, also showing basic agreement between the two generators. Note that these kinematic distributions have been evaluated exclusively in events passing the selection criteria pointed out above, in order to exclude false disagreements between the samples originating from final states which are irrelevant for the analysis of this thesis and therefore not fully accounted for in the WHIZARD/SHERPA sample (especially events with zero jets). The discrepancies left in fig. 15 could be effects of the detailed jet simulation procedure or electromagnetic final state radiation. The remaining plot in fig. 15 presents the normalized event selection efficiencies in the different samples when tightening the p_T cut on all final state objects, pointing out that the quantitatively good agreement of the effective cross sections is more or less stable against a tightening p_T cut.

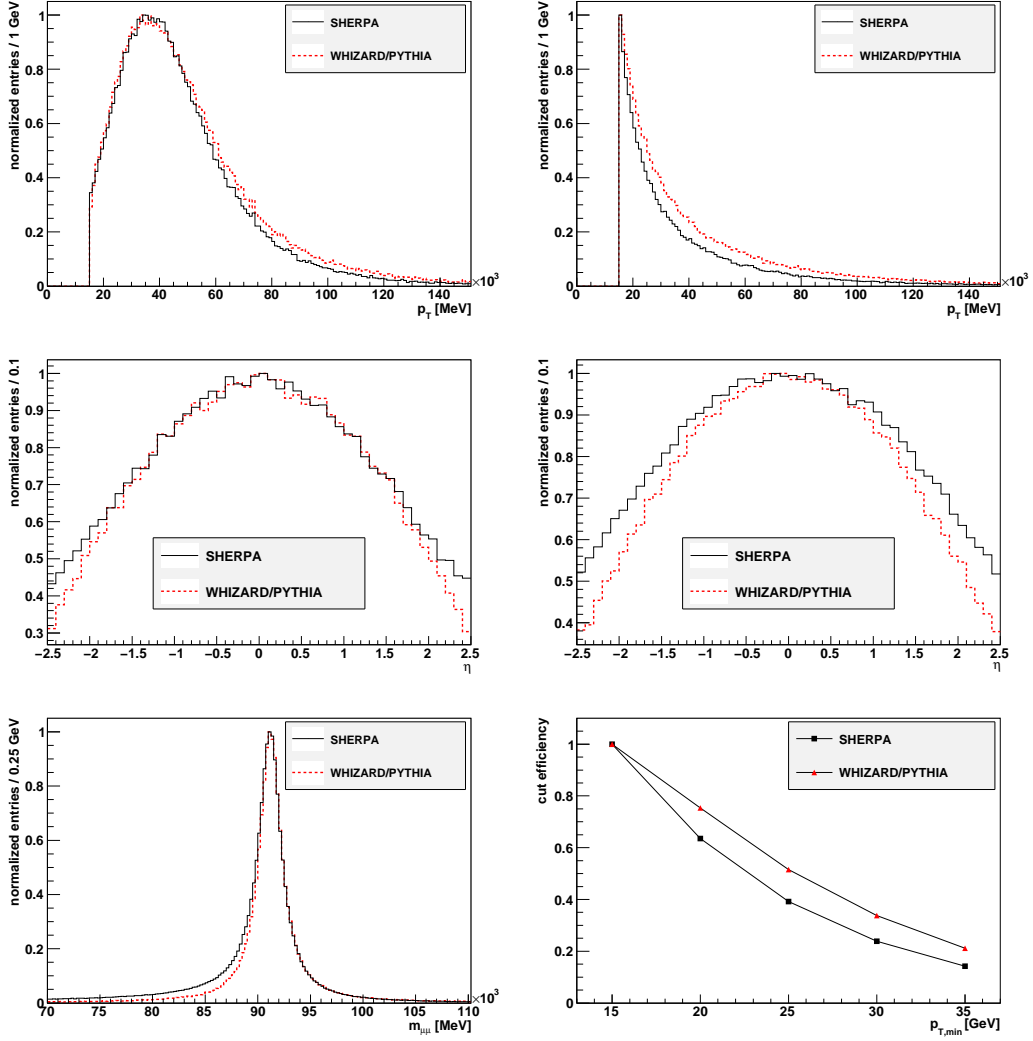


Figure 15: Comparison of kinematic distributions from SHERPA (black) and WHIZARD/PYTHIA (red): p_T of muons (top left) and jets (top right), η of muons (center left) and jets (center right), and the Z resonance in the di-muon mass (bottom left). The plot on the bottom right shows the event selection efficiencies for a varying p_T cut, normalized to the loosest cut $p_T > 15$ GeV.

4 Search for Heavy Gauge Bosons

4.1 Final State Reconstruction

4.1.1 Muons

Due to their relatively large mass, long lifetime and absence of color charge, muons majorly traverse all inner detector parts including the calorimeters without losing too much energy. With the muon spectrometer, cf. section 3.1.4, the ATLAS detector possesses a dedicated subdetector system to account for this particle type. As soon as a muon causes hits in all three MDT layers within $|\eta| < 2.7$, its track and p_T can be uniquely determined from muon spectrometer data exclusively. This is achieved by interpolating the three separate tracks through the individual MDT layers with regard to the toroidal magnetic field, where p_T is then obtained from the sagitta of the track curvature. The tracks and 4-momenta thus reconstructed exclusively from muon spectrometer data make up the contents of the standalone muon container. In addition, for $|\eta| < 2.5$ these standalone tracks may be matched with ID tracks, if available, to give rise to so-called combined-track muons which are filled into the staco muon container (cf. [4, 10] for the paragraph). Using only this container may lead to higher precision at the cost of decreasing efficiency, see below.

An intuitive quality check for the muon performance of the detector is the matching of kinematic observables on truth and reco level, where in this case the reducible background sample in the $\mu\nu jj$ channel is analyzed because it conveys the best statistics by far. Technically, the truth and reco muons are matched by computing the distribution of the enclosed angle between the truth particles and their respectively closest reco partners. The width of this distribution then defines an angular cone of fixed size $\Delta R = 5 \cdot 10^{-3}$ which is used to find the matching reco particle of each truth particle (cf. fig. 16), so that the differences of the kinematic variables η , φ and p_T can be evaluated. The resulting distributions and Gaussian resolutions are shown in fig. 16, where it must be noted that the p_T resolution scales with the absolute value of p_T due to the underlying measurement procedure which is based on the curvature in a magnetic field [2]. This scaling is accounted for by normalizing with the true norm of p_T . Note further that in general all resolutions of kinematic variables basically depend on the complete direction of the particle. However, due to the approximate rotational symmetry of the ATLAS detector around the beam axis the φ dependence is generally small and therefore averaged here for simplicity, whereas the η dependence is accounted for by averaging over defined η intervals which show approxi-

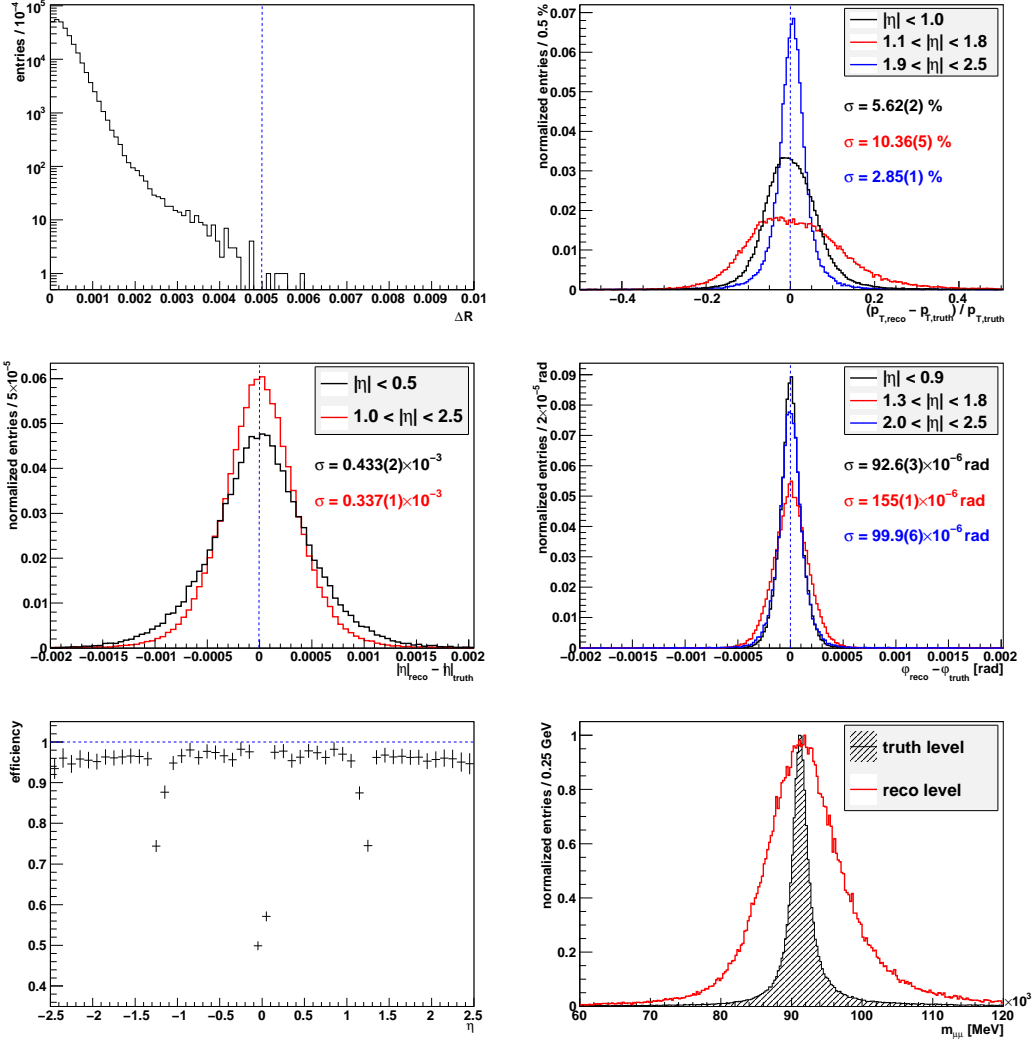


Figure 16: Comparison of muon data on truth and reco level: Angular matching (top left, with the cone size for truth/reco matching indicated with a dashed blue line), normalized p_T difference of matching pairs (top right), η difference (center left), φ difference (center right), and η -resolved efficiency (bottom left), as well as the Z resonance in the $\mu\mu jj$ channel (bottom right).

mately constant resolutions. For example, in fig. 16 the evaluation of the p_T resolution is split up into the barrel region with $|\eta| < 1.0$, the transition region with $1.1 < |\eta| < 1.8$ and the end-cap region with $1.9 < |\eta| < 2.5$. The corresponding resolutions for staco muons of 5.6%, 10% and 2.9% in the respective regions majorly reflect the local strength of the toroidal magnetic field, which drops severely in the transition region and adopts its largest value in the end-cap region [5]. The said values are comparable to those given in [5] for standalone muons (4%, 9% and 3% in the respective regions), although they cannot fully compare with the staco muon performance estimated in the said reference as 2.5%, 4% and 3%, respectively. However, it is pointed out in [5] that the p_T scale invariance of the fractional resolution only holds approximately, especially for staco muons, so that perfect agreement cannot be expected when comparing different samples with undefined p_T scales. The resolutions of the angular variables are roughly constant over the whole η range considered, with an η resolution getting slightly better from barrel to end-cap, and a φ resolution which is constant except for the transition region. Finally, the Z resonance in the invariant mass of two muons is computed on truth and reco level in the reducible background sample of the $\mu\mu jj$ channel, illustrating the increasing width on reco level due to the convolution of the intrinsic shape with the detector response (cf. fig. 16). Fitting the resonance with a numeric convolution of an intrinsic Breit-Wigner distribution of known width [37] and a Gaussian resolution function, the Z mass is found as $m_Z = 91.51(2)$ GeV with an experimental resolution $\sigma_Z = 5.18(2)$ GeV, which is right between the values given in [4] of 2.5 GeV for perfect alignment of the muon spectrometer and 8 GeV without alignment.

Apart from plainly comparing kinematic observables on truth and reco level, there are two standard benchmark quantities to quantify the muon reconstruction quality from truth data, namely fake rate and efficiency [5]. The fake rate is defined as the percentage of reconstructed muons which have no truth muon inside the angular matching cone mentioned above, whereas, on the other hand, the muon efficiency is the percentage of truth muons within a given cut region which have a matching reconstructed muon inside the said cone. In the high-energetic regime considered here, the fake rate and efficiency are practically independent of the applied p_T cut, while especially the efficiency reflects the ATLAS detector geometry and therefore depends on η (cf. fig. 16 for staco muons): It is symmetric to $\eta = 0$ as expected, showing a constant value over the entire cut region with three narrow drops at $\eta = 0$ and $|\eta| \approx 1.3$, where the central drop stems from the cabling of the inner detector parts and the two other drops are in the transition region between barrel and end-caps of the muon spectrometer [5]. Note that the fake rate and mean efficiency adopt slightly different values in the various reconstruction

modes: In the $\mu\nu jj$ channel, including all reconstructed muons the fake rate is 1.38 (2) % and the efficiency amounts to 95.8 (3) %, while restriction to staco muons delivers a roughly halved fake rate of 0.68 (2) % which is merely traded for a slightly worse efficiency of 93.1 (3) %, so that from here on data analysis is restricted to staco muons. All the numbers just given are practically the same in the other final states, and agree very well with the respective official numbers given in [5].

4.1.2 Electrons

The detector signature of electrons strongly differs from that of muons due to the much smaller mass, which leads to greatly increased multiple bremsstrahlung and consequent energy deposition especially inside the ECal. These energy clusters are generally reconstructed via jet algorithms, cf. section 4.1.3, while additional algorithms exist to explicitly identify low- p_T and high- p_T electrons [4, 10]: Low- p_T electrons are reconstructed by a track-based algorithm which is seeded by a charged track inside the ID, and high- p_T electrons are reconstructed by a cluster algorithm seeded by energy clusters inside the ECal, where the track-based algorithm matches the ID track to ECal jets, and vice versa for the cluster algorithm. The results of both electron finder algorithms are stored separately in ESDs and merged afterwards to make up the contents of the electron container of AODs.

In order to evaluate the quality of electron reconstruction at the ATLAS detector, the simulated data are compared to truth data analog to the procedure for muons in section 4.1.1, again based on the reducible background samples of the $e\nu jj$ channel for kinematics and the $lljj$ channel for the Z resonance (cf. fig. 17 for plots and Gaussian resolutions). Note that in general the resolutions of all kinematic variables of electrons scale with \sqrt{E} [2], which is taken into account by normalizing all differences of kinematic variables with the square root of the true energy. The energy resolution is $\sigma_E = 14\% \times \sqrt{E/\text{GeV}}$ for $|\eta| < 0.5$ and $\sigma_E = 20\% \times \sqrt{E/\text{GeV}}$ for $0.9 < |\eta| < 1.2$, which is slightly worse than the corresponding values given in [5] for electrons with defined energies of 100 GeV, namely 1.1 % at $|\eta| = 0.325$ and 1.7 % at $|\eta| = 1.075$. The η resolution is evaluated as $\sigma_\eta = 75 \cdot 10^{-6} / \sqrt{E/\text{GeV}}$ in the central barrel region with $|\eta| < 0.5$ and as $\sigma_\eta = 26 \cdot 10^{-6} / \sqrt{E/\text{GeV}}$ in the end-cap region with $|\eta| > 1.7$, in approximate agreement with the values $0.7 \cdot 10^{-3}$ and $0.4 \cdot 10^{-3}$ given in [5] for 100 GeV electrons in the respective detector regions. However, the φ resolution has a nearly constant value of $\sigma_\varphi = 23 \cdot 10^{-6} \text{rad} / \sqrt{E/\text{GeV}}$ over the whole η region considered, a result which is not fully covered in [5], where the corresponding values are given as $0.4 \cdot 10^{-3}$ in the barrel region and $1.5 \cdot 10^{-3}$ in the end-cap

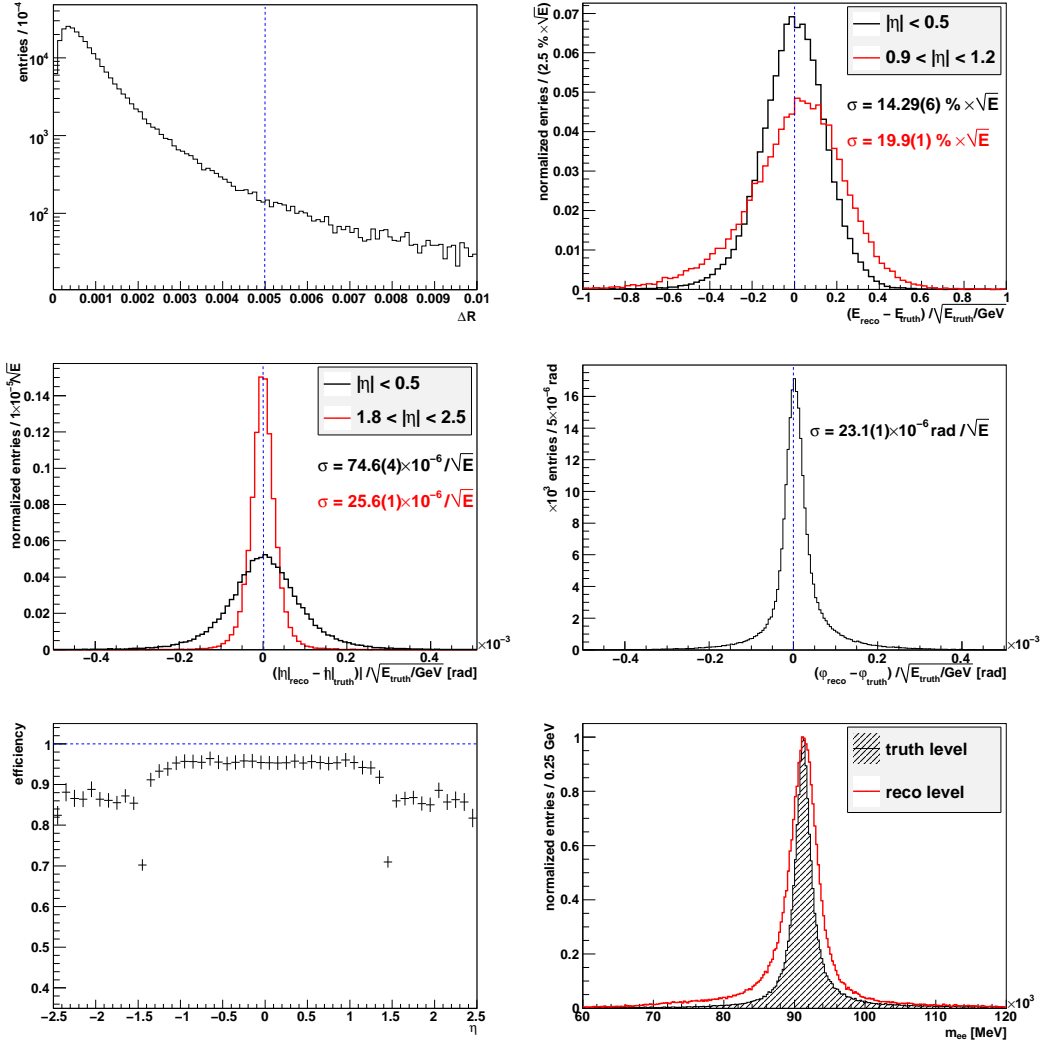


Figure 17: Comparison of electron data on truth and reco level: Angular matching (top left, fake/efficiency cone in blue), normalized difference of p_T (top right), η (center left), φ (center right), as well as the η dependence of the efficiency (bottom left) and the Z resonance in the $eejj$ channel (bottom right).

region for electrons with an energy of 100 GeV. It is stressed again that perfect agreement would rely on an exact scale invariance with respect to \sqrt{E} , which cannot be assumed here either. Finally, the Z mass is determined to $m_Z = 91.12(1)$ GeV with a Gaussian resolution of $\sigma_Z = 2.08(1)$ GeV, while it must be noted that the Z line shape itself is used to calibrate ECal signals [5] when comparing this result to the muon performance.

With a cone of size $\Delta R = 5 \cdot 10^{-3}$ fixed from angular matching (cf. fig. 17), the efficiencies and fake rates of electrons can be evaluated in the reducible background sample of the $e\nu jj$ channel. The η dependency of the efficiency (fig. 17) is again symmetric to $\eta = 0$, showing a pattern which is qualitatively the same as for muons (cf. fig. 16), namely a constant value in the barrel region within $|\eta| < 1.3$, while the two sharp drops at $|\eta| \approx 1.5$ correspond to the transition from barrel to end-cap of the ECal and those at $|\eta| \approx 2.5$ indicate the end of the ID. The mean efficiency of the electrons is 86.7(2) % in agreement with [5], and the fake rate amounts to 46.6(1) %, whereas the $eejj$ channel shows an equal efficiency of 86.8(2) % and a somewhat smaller fake rate of 29.7(1) %. Note that although both lepton flavors show roughly equal efficiencies, the electrons have much bigger fake rates than muons, cf. section 4.1.1, because fake electrons are produced in large numbers by all kinds of objects including the original electrons, e. g. via bremsstrahlung and pair production inside the calorimeters. This is also illustrated by the rate of truth electrons having more than one hard reconstructed electron inside their matching cone, which amounts to 0.60(1) % in the $e\nu jj$ channel, whereas for muons this number is only 0.023(3) % (all muons) respectively 0.0000(4) % (staco muons).

4.1.3 Hadron Jets

Jet-Finding Procedure Before pointing out the actual jet-finding algorithms in more detail, the attention is first directed onto the different types of preprocessed detector data [4, 5] which seed these jet algorithms and convey their input. The starting point are always energy depositions inside single cells of the calorimeters (cf. section 3.1.3), which are first clustered by a clustering algorithm: The tower algorithm produces so-called towers defined as the summed energy deposition in all calorimeter cells within a solid angle segment of the defined size $\Delta\eta \times \Delta\varphi = 0.1 \times 0.1$. The other available clustering algorithm produces topological clusters, which contain three-dimensional information about the energy deposition. This algorithm is seeded by a single calorimeter cell with an energy deposition of at least four times the cell noise, thus implying inherent noise suppression to some extent. The signal of this seed cell is then added up with those of all cells in the direct neigh-

borhood above a minimal signal threshold to build an energy topocluster. Since jet-finding algorithms need complete 4-momenta as input, each tower and topocluster is treated like a massless pseudo-particle in order to convert the measured energy E and direction (η, φ) into 4-momentum components by simple projection of the 3-momentum \vec{p} , with $\vec{p}^2 = E^2$:

$$p_x = E \frac{\cos \varphi}{\cosh \eta}, \quad p_y = E \frac{\sin \varphi}{\cosh \eta}, \quad p_z = E \tanh \eta. \quad (4.1)$$

Given these sets of 4-momenta corresponding to the pseudo-particles of calorimeter data, there are two jet-finder algorithms which are used by default at ATLAS [5] to compose jets with defined 4-momenta: the ATLAS seeded cone algorithm [4, 5] and the k_T algorithm [56, 57].

The cone algorithm is seeded by every tower or cluster which passes a cut on $p_T > 1$ GeV, where an angular cone of fixed size R (the only parameter of the algorithm) is put around the 4-momentum direction (η, φ) of the seed, and all 4-momenta inside this cone are then added. This is repeated several times, with new cone directions defined by the directions of the resulting 4-momentum sums of the old ones, until the direction eventually becomes stable, thus defining the final jet. This algorithm is collinear-safe, meaning that the splitting of an initial 4-momentum into two collinear ones does not change the resulting jets, but not infrared-safe, which means that adding a small 4-momentum to the initial set of 4-momenta may change the resulting jets.

In the general class of k_T -like algorithms [56, 57], an order parameter d_{ij} is defined on the set of initial 4-momenta p_i as

$$d_{ij} \equiv \begin{cases} \min(p_{T,i}^{2a}, p_{T,j}^{2a}) \frac{\Delta R_{ij}^2}{R^2} & , i \neq j \\ p_{T,i}^{2a} & , i = j \end{cases} \quad (4.2)$$

with parameters R and a , where $a = 1$ ($a > 0$ in general) is referred to as k_T algorithm and $a = -1$ ($a < 0$) is called anti- k_T algorithm. Among a given set of initial p_i , all possible d_{ij} are computed and sorted according to their value. If the smallest one corresponds to $i = j$, the associated momentum is removed from the set as a stable jet, otherwise the two momenta p_i and p_j are merged to form a new momentum $k = p_i + p_j$ in the set. This procedure is then repeated, always with updated sets of momenta, until no input momentum is left. Note that this class of algorithms is generally collinear-safe and also infrared-safe [57].

Finally, the jets emerging from these jet-finder algorithms must be calibrated [5]. To that end, it is first distinguished between electromagnetic

jets, which tend to show comparably high signal densities in the calorimeter cells and need no further calibration, and hadronic jets incorporating smaller signal densities, which must be calibrated due to the ambivalence between electrons and pions in the detector. This is done by separately reweighting each cell signal contributing to an individual jet with a weight factor that depends on the position and signal density of the cell and ranges from 1 for high density up to the e/π signal ratio of ~ 1.5 at ATLAS for low density. For the topoclusters, this cell weighting can also be done before the actual jet-finding, thus giving rise to so-called locally calibrated (LC) topoclusters as input to the jet algorithms, which are the default input for the reprocessing of jet algorithms on AOD.

Performance of Jet Algorithms and Inputs In order to quantify the reconstruction performance of the various jet algorithms and inputs available at ATLAS, $2 \cdot 10^4$ events of each SM gauge boson decaying hadronically were generated with WHIZARD and PYTHIA, simulated with ATLFast-2 (cf. section 3.2), and finally reconstructed with different jet algorithms, inputs and parameters. The reconstruction quality of the respective resonances in the invariant mass of the two best-fitting final-state jets is used as a benchmark to cross-check the performances of the different reconstruction setups (cf. fig. 18 for respective plots).

Firstly, the R parameter is varied from 0.3 to 0.5 (the ATLAS default is 0.4 for narrow jets) for the seeded cone algorithm on LC topoclusters, illustrating the fact that the reconstruction is very sensitive on the value of this parameter, and indeed works best with the default value 0.4. Now the jet algorithm itself is varied for $R = 0.4$ on LC topoclusters, which shows that the choice of the actual algorithm has no significant impact on the width or shape of the resonance, only the k_T algorithm leads to a slightly shifted absolute position compared to the other algorithms. Finally, the input data are varied for the seeded cone algorithm with $R = 0.4$, displaying a remarkable result: The AOD standard jet input formed by LC topoclusters actually shows the worst result, namely the largest resonance width, compared to ordinary topoclusters and towers, which have roughly the same performance. From fig. 18 it is now verified that the performance of the default setup for narrow jets at ATLAS, consisting of the seeded cone algorithm with $R = 0.4$ on topocluster input, is not exceeded significantly by any other setup for the analysis carried out here, so that it is generally adopted from here on for jet reconstruction.

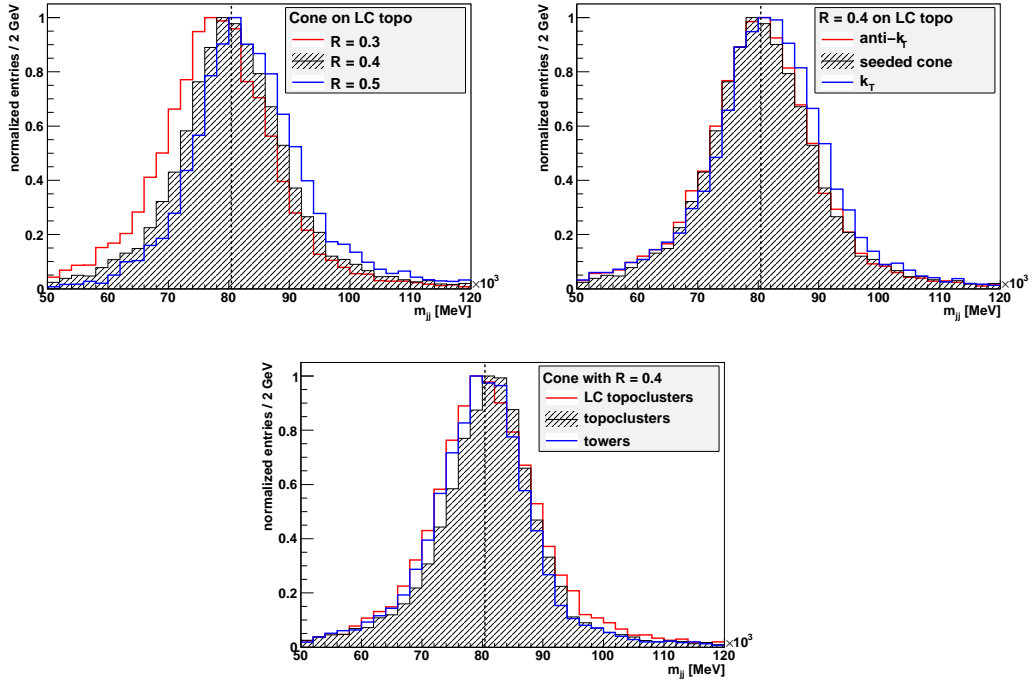


Figure 18: Normalized W resonance in the invariant mass of two reconstructed jets, with different reconstruction setups: Seeded cone algorithm on LC topoclusters with varied parameter R (upper left), different jet algorithms with $R = 0.4$ on LC topoclusters (upper right) and seeded cone algorithm with $R = 0.4$ on different input data (below). The correct W mass is indicated with a dashed line in each case.

Rejection of Electron Jets An important notion concerning the jet containers of reconstructed detector data is that they contain any object which has caused energy clusters inside one of the calorimeters and is hence reconstructed by a jet algorithm, i. e. no distinction is made whatsoever concerning the particle type producing a jet. This implies that although dedicated algorithms exist to explicitly identify low- p_T and high- p_T electrons from inner detector and calorimeter data, cf. section 4.1.2, the corresponding calorimeter jets will still be kept within the jet container. Therefore, it remains as a task to be carried out by hand during every analysis to apply an electron-veto on the contents of the jet container. This is done by default via ΔR matching combined with a cut on some minimal energy ratio of electrons from the electron container and jets from the jet container to exclude false

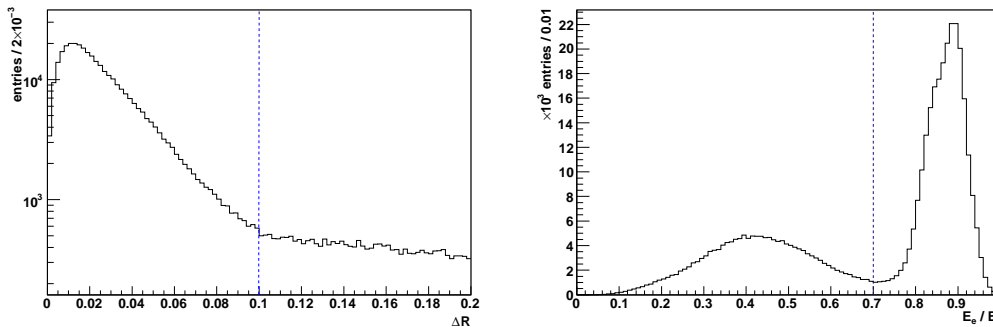


Figure 19: Essential quantities for the rejection of electrons in the hard jets: Enclosed angle of every hard jet and respective closest electron within one event (left) and the energy ratio of these pairs (right). The rejection cuts, eqn. (4.3), are marked with blue dashed lines.

matching of real hadron jets with collinear fake electrons (cf. fig. 19):

$$\begin{aligned} \Delta R(e, j) &< 0.1 \\ \text{and } E_e/E_j &> 0.7, \end{aligned} \quad (4.3)$$

where all jets passing these cuts for any electron in the electron container are discarded. Note that for correct matching the energy fraction peaks at $\lesssim 90\%$ rather than 100% due to the hadronic energy calibration of the container jets, which leads to larger energy values.

4.1.4 Neutrinos

Basic Idea As already mentioned several times, neutrinos generally escape detection because they exclusively interact weakly. Since all transverse momenta of an event must necessarily add up to zero due to momentum conservation, this circumstance gives rise to the occurrence of missing transverse energy \cancel{E}_T , which can be associated with the transverse projection of the original neutrino momentum p_ν . However, the information obtained from \cancel{E}_T in the form of two scalar quantities, such as φ and the absolute of \cancel{E}_T , is exactly one scalar too short to reconstruct the full 4-momentum when the mass shell condition is included.

A standard approach to cope with this drawback is to set the W boson which originally decayed leptonically into the neutrino and the respective charged lepton on the mass shell and use the fully known 4-momentum p_l of

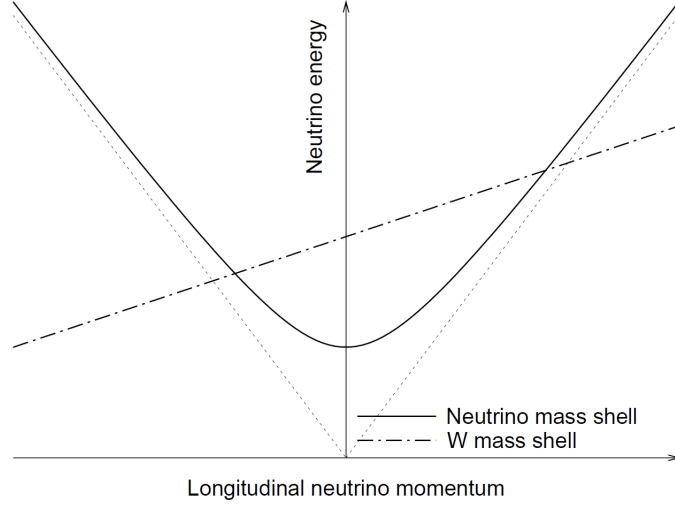


Figure 20: The mass shell conditions of the neutrino and a W boson decaying leptonically, plotted in the plane of the two remaining unknowns, namely the energy and the longitudinal or z component of the neutrino 4-momentum [6]. The intersections of the two curves give rise to possible solutions for these quantities.

the charged lepton to compute the missing information [6]. The two mass shell conditions read, with $p_\nu \equiv p$ and $p_l \equiv q$:

$$p^2 = 0, \quad (4.4)$$

$$(p + q)^2 \simeq 2p \cdot q = m^2, \quad (4.5)$$

where the lepton mass was set to zero in the mass shell condition of the W in the second line. While the neutrino mass shell condition, eqn. (4.4), describes a hyperbola in the plane of the two remaining unknowns, namely the neutrino energy p_0 and the z component p_z of its 3-momentum, the W mass shell condition, eqn. (4.5), imposes a linear dependency between the two unknowns. In general, these two curves will intersect twice (cf. fig. 20), leading to two independent solutions for p_ν none of which is preferred by kinematic arguments [6]:

$$p_0 = \frac{q_0^2 (m^2 + 2\vec{p}_T \cdot \vec{q}_T) \pm q_L A}{2q_0 (q_0^2 - q_z^2)}, \quad (4.6)$$

$$p_z = \frac{q_z (m^2 + 2\vec{p}_T \cdot \vec{q}_T) \pm A}{2(q_0^2 - q_z^2)} \quad (4.7)$$

$$\text{with } A \equiv q_0 \sqrt{(m^2 + 2\vec{p}_T \cdot \vec{q}_T)^2 + 4p_T^2 (q_z^2 - q_0^2)},$$

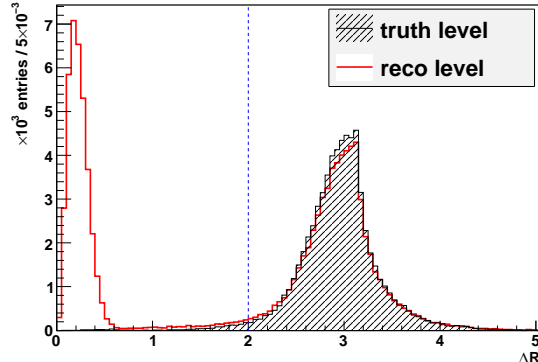


Figure 21: Enclosed angle between a di-jet resonance with an invariant mass inside the cut window of the SM gauge bosons and all reconstructed electrons in the same event, both on truth level and on reco level. The rejection cut for fake electrons in the vicinity of the jet resonances is indicated with the blue dashed line.

where p_T is identified with \cancel{E}_T in the analysis of detector data. There are two ways now to proceed with this result: One could either put in the mass of the heavy gauge boson m' and choose the “better” solution in the sense that it gives an invariant mass of the whole final state which is closer to m' , or one could simply incorporate both solutions into the analysis, thus effectively doubling the background [6], where the second approach is completely unbiased with respect to the observable m' and therefore pursued in the analysis of the $l\nu jj$ channel.

Note that the electron samples may contain more than one hard electron per event due to the ECal showers, cf. section 4.1.2 and fig. 38 in appendix C, so that some choice must be met about the electron momentum to be used for neutrino reconstruction. The easiest way to account for this is an angular isolation cut against the direction of the SM gauge boson reconstructed from two jets, i. e. demanding exactly one electron with $\Delta R(e, W/Z) > 2.0$, which is then assumed to be the right one (cf. fig. 21).

Reconstructed 4-Momenta When performing this momentum reconstruction with simulated data, it turns out that a certain amount of events in the samples give complex solutions for p_0 and p_z , i. e. the quantity A in eqns. (4.6) and (4.7) becomes imaginary due to a negative radicand, which happens in $\sim 10\%$ of all events on truth level and in $\sim 25\%$ of the reco level events. Noting that these percentages are very sensitive on the actual value of m inserted into eqns. (4.6) and (4.7), this can be interpreted as an

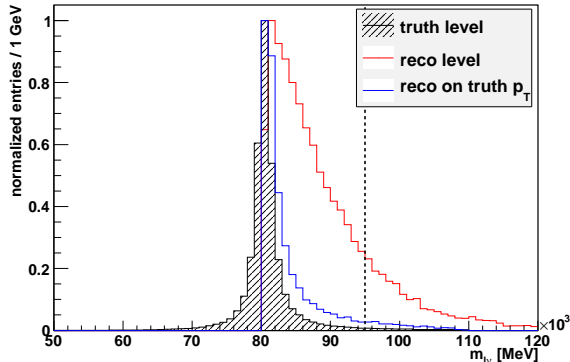


Figure 22: Distribution of the W mass, both on truth level and as computed from eqn. (4.11) using \cancel{E}_T on reco level as well as the true p_T on truth level as a consistency check, where the black dashed line indicates the mass cut applied on reco level.

artifact of the wrong assumption that the original W boson be on-shell, eqn. (4.5): From this point of view it is also clear that the number of events with complex solutions must increase from truth to reco level, since the width of the underlying W resonance grows due to the convolution with the detector response.

In order to increase the statistics in the data analysis, one can now attempt to reconstruct meaningful solutions for p_0 and p_z also in the said events with complex solutions of eqns. (4.6) and (4.7). To that end, one could solve for the distance between the two mass shells in the p_0 - p_z plane, take the endpoint on the neutrino mass shell to compose p_ν , and use the actual value of the distance as a cut variable. On the other hand, being serious about the notion above relating to finite widths of the W resonance, one could also impose the extra condition of one degenerate solution,

$$A \stackrel{!}{=} 0, \quad (4.8)$$

in all events with complex momentum solutions and solve for m in addition to p_0 and p_z , which delivers a physically more natural cut variable together with the full p_ν . The physically sensible solutions of this equation system

are:

$$p_0 = q_0 \frac{p_T}{\sqrt{q_0^2 - q_z^2}}, \quad (4.9)$$

$$p_z = q_z \frac{p_T}{\sqrt{q_0^2 - q_z^2}}, \quad (4.10)$$

$$m^2 = 2 \left(p_T \sqrt{q_0^2 - q_z^2} - \vec{p}_T \cdot \vec{q}_T \right). \quad (4.11)$$

These equations are applied during the following analysis of the $l\nu jj$ channel to compute the missing components of p_ν in all events where eqns. (4.6) and (4.7) fail to give real results. The solutions for m are plotted in fig. 22 for the reducible background sample of the said channel on truth and reco level as well as on truth level with p_ν computed from the true p_T of the neutrino for a cross-check, illustrating the fact that just those events with a positively off-shell W tend to produce complex solutions in the ordinary reconstruction procedure described before.

Finally, in order to check the quality of the momentum reconstruction, the kinematic observables of the reconstructed momenta are compared with the true values corresponding to the neutrino momenta on truth level, analog to the procedure for charged leptons, cf. sections 4.1.1 and 4.1.2. It must be distinguished between those variables which emerge directly from measurement, i. e. the norm of \cancel{E}_T and its direction φ in the transverse plane, and the pseudorapidity η which essentially results from the equations for p_0 and p_z introduced above. It is further distinguished between the lepton flavors of the samples, because due to the reconstruction principle the neutrino results depend on the reconstructed momenta of the charged leptons. With all the involved problems and shortcomings, neutrino reconstruction can by no means be called a precision measurement, so that it is dispensed here with an explicit examination of energy scale and η dependences; the \cancel{E}_T distribution is just normalized to the true p_T of the neutrino for convenience (cf. fig. 23 for results). Note that the said \cancel{E}_T matching does not only have a comparably large width but also shows a systematic shift to smaller values: The relative loss amounts to 8.74 (4) % in the electron samples and 9.73 (4) % in the muon samples. However, this is no surprise given the fact that \cancel{E}_T is defined as the missing piece of transverse momentum which complements all measured contributions to give zero overall, so that every loss of transverse energy during the measurement of the visible transverse momenta automatically leads to an underestimation of \cancel{E}_T .

The determination of η depends on the computation scheme and is therefore examined separately for neutrinos which were reconstructed using eqns.

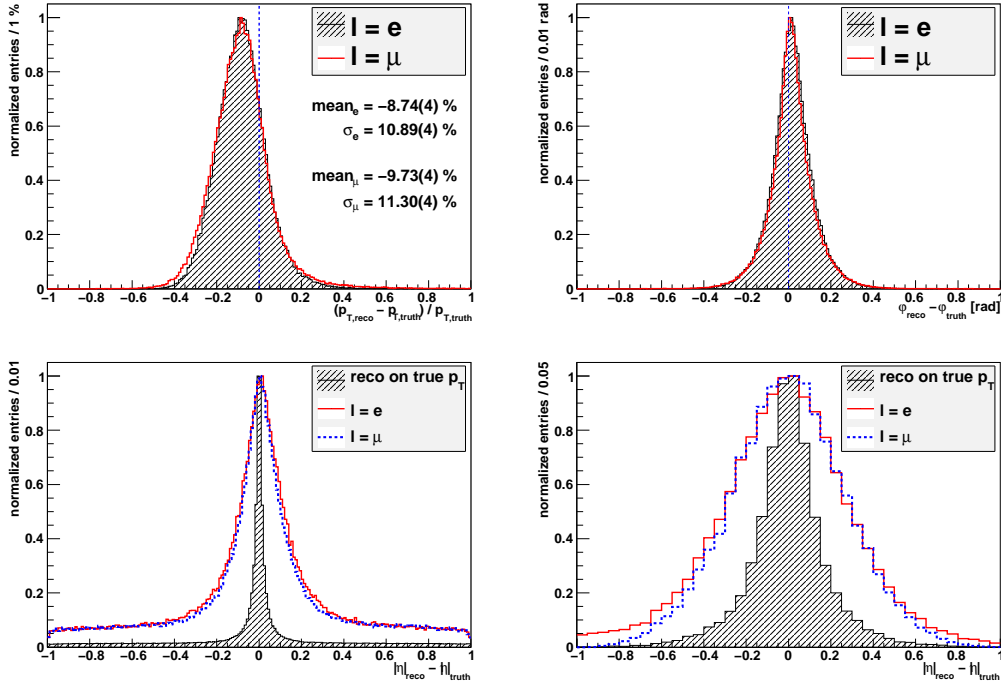


Figure 23: Matching of true and reconstructed neutrino momenta: Comparison of the norm (top left) and direction (top right) of \cancel{E}_T with the true p_T , as well as the η matching of \pm neutrinos (bottom left, both solutions added) and c neutrinos (bottom right), where in each case the results are shown for both lepton flavors on reco level, and for η additionally on truth level using the true p_T of the neutrino and the true charged lepton as a cross-check.

(4.6) and (4.7) (“ \pm ” neutrinos, both solutions added), and for those from eqns. (4.9) and (4.10) (complex or “ c ” neutrinos). As shown in fig. 23, even the reconstruction using the true charged lepton and p_T of the neutrino has a small but finite width, which is but another consequence of forcing the W onto its mass shell. Naturally this width further grows on reco level because of the rather inaccurate p_T measurement via \cancel{E}_T , whereas the constant offset both on truth and reco level in the \pm neutrino data stems from matching the true neutrino with the wrong of the two available reconstructed solutions. Nonetheless, the matching of the correct \pm neutrinos with true data is much better in general than for the c neutrinos. Yet the final decision whether to include them in the analysis or not will be met upon the examination of their actual contribution to the heavy gauge bosons signal, which is addressed in the following section.

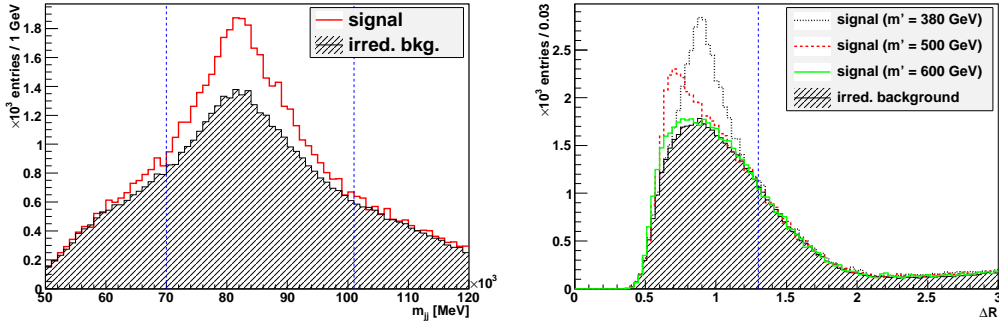


Figure 24: Kinematic cuts (dashed blue lines) on the jet pairs in the $lvjj$ final state: The requirements are an invariant mass in the range of the SM gauge bosons (left, $m' = 500$ GeV) and a maximal value of the enclosed angle (right).

4.2 $lvjj$ Channel

4.2.1 Basic Analysis

In order to isolate potential decay events of the heavy gauge bosons at the ATLAS detector, their respective final state signatures in terms of reconstructed detector objects must first be determined. For the $lvjj$ channel the loosest event selection criteria would be to demand exactly one isolated charged lepton and at least two hadron jets, all passing the kinematic cuts in eqn. (3.10), as well as missing transverse energy which also passes the p_T cut of eqn. (3.10). In order to further reduce QCD background, additional kinematic cuts are applied to the hadron jets, which restrict the allowed phase space to the topology associated with the decay of a strongly boosted SM gauge boson. The corresponding requirements are to find at least one jet pair with an invariant mass within a cut window around the SM gauge bosons and a relatively small enclosed angle (cf. fig. 24),

$$70 \text{ GeV} < m_{jj} < 101 \text{ GeV} \quad \text{and} \quad \Delta R(j, j) < 1.3, \quad (4.12)$$

where the mass interval corresponds roughly to the di-jet mass resolution of the bosons (cf. section 4.2.3). However, the separation of W and Z in these di-jet resonances cannot be achieved by a simple mass cut because the resonance widths are of the same size as the mass difference of W and Z : The problem of disentangling the SM gauge bosons will be addressed in section 4.2.3.

Fig. 24 also illustrates that the size of the angular jet separation in the W'/Z' signal depends inversely on the actual value of m' , because an

increased mass of the heavy gauge bosons naturally induces a stronger boost of the resulting SM bosons and their decay products, i. e. the parton pair and the lepton pair. This leads to a severe reduction of the signal for $m' > 500$ GeV (cf. fig. 26 and numerical results below), because the lessening angular parton separation eventually runs into the di-jet resolution of the detector which is bounded by the parameter $R = 0.4$ of the jet algorithms (cf. section 4.1.3). On the other hand, the collinearity cut in eqn. (4.12) is chosen loose enough to account for the whole range allowed by experimental data, down to $m' = 380$ GeV.

The last requirement for event selection is to reconstruct at least one neutrino momentum from the charged lepton and \cancel{E}_T which also passes all kinematic cuts (together with a cut on the W mass for c neutrinos, as pointed out in the previous section). If both \pm neutrinos pass all cuts, the corresponding event is evaluated with each of them, thus being factually doubled in the analysis. With the two lepton momenta and the momenta of the di-jet resonance, a rather loose back-to-back cut is applied on the reconstructed gauge boson momenta associated with the lepton pair and the jet pair,

$$2.0 < \Delta R(W, W/Z) < 4.0, \quad (4.13)$$

whereas the signal observable to be analyzed is defined as the invariant mass $m_{l\nu jj}$ of these four final state momenta, which should have a resonance around the mass m' of the heavy gauge bosons W' and Z' . Since electrons and muons convey nearly identical signal reconstruction performances, they are summed in the whole analysis in order to increase statistics.

Before proceeding, it is sensible to compare the signal contributions of the \pm neutrinos and the c neutrinos (cf. section 4.1.4) in order to ultimately decide whether to include the c neutrinos in the analysis. Fig. 25 shows the signal observable $m_{l\nu jj}$ computed with either of the two different types of reconstructed neutrino momenta in samples containing the heavy gauge boson signal and irreducible background. It turns out that the c neutrinos produce some more low-energy background than the \pm neutrinos but otherwise have roughly the same signal-to-background ratio around m' despite their poor matching performance with the true neutrinos, and are therefore included in the further analysis.

In order to quantify the signal resonance, it has to be compared with the total amount of background in the signal observable. To that end, all kinds of reducible backgrounds are added to both the signal sample and the irreducible background sample (cf. fig. 26). As it turns out it is feasible to further adapt the event selection such as to demand not at least but exactly two hadron jets per event, which represents a very effective suppression of the

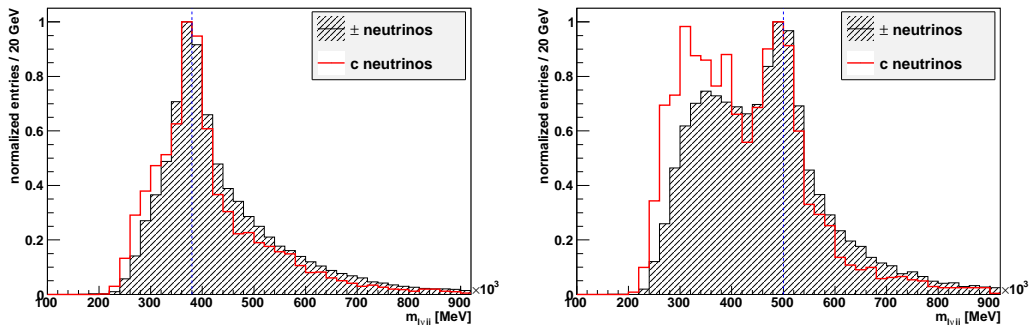


Figure 25: Invariant mass of the di-jet resonance, the charged lepton and one reconstructed neutrino momentum in the 100 fb^{-1} signal samples of the $l\nu jj$ channel with $m' = 380 \text{ GeV}$ (left) and 500 GeV (right). The two different neutrino reconstruction methods (\pm neutrinos summed up) are plotted separately in order to compare their signal performance.

multi-jet backgrounds emerging from more than two hard partons on matrix element level, like the $t\bar{t}$ background considered here. With this additional cut, the heavy gauge boson resonance is now isolated by subtracting the irreducible background sample from the signal sample, so that the resulting shape can be fitted in order to get a hold of the resonance position and width for different mass parameters m' (cf. fig. 27). Note that the intrinsic Breit-Wigner width of the heavy gauge bosons is around 1% of m' [6] and thus roughly an order of magnitude smaller than the detector resolution in the theoretically allowed region, so that it is neglected for the fits in fig. 27.

With a given mass interval around m' (roughly $\pm 30 \text{ GeV}$ from fig. 27), the number of W'/Z' signal events N is obtained by subtracting the number of background events N_b from the total number of events N_t inside the said mass interval [6],

$$N = N_t - N_b . \quad (4.14)$$

It is crucial to note that a large fraction of original background events N'_b , namely all with two \pm neutrinos within the kinematic cuts, is double-counted in N_b due to the adopted neutrino reconstruction method, so that the standard deviation of N_b is not simply given by Poisson statistics but must be scaled accordingly. In a conservative approach, assuming an exact factor 2 despite the fact that not all \pm neutrinos enter the analysis and the events with c neutrinos are not double-counted at all, this leads to [6]

$$\sigma_{N_b} = 2\sigma_{N'_b} = 2\sqrt{N'_b} = \sqrt{2N_b} , \quad (4.15)$$

which gives the significance s of the signal, defined as the number of signal

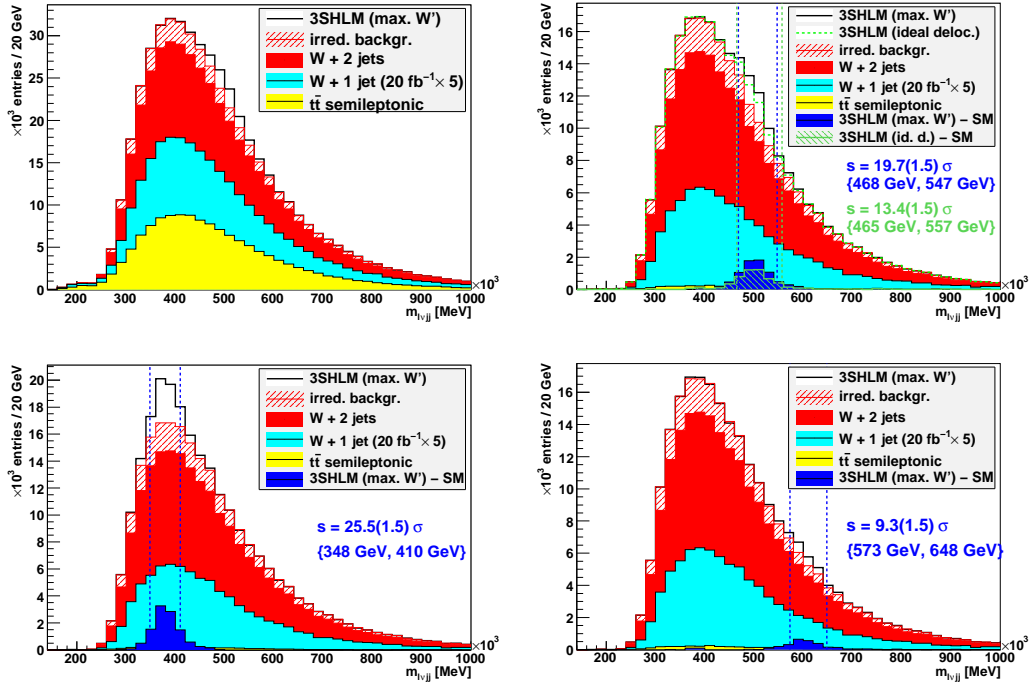


Figure 26: Signal and all backgrounds covering 100 fb^{-1} in the $lvjj$ final state. The top row displays the signal sample for $m' = 500 \text{ GeV}$ with the requirement of at least (left) and exactly (right) two hadron jets per event on detector level. The bottom row shows $m' = 380$ (left) and 600 GeV (right) with exactly two jets per event. Note that $g_{W'ff}$ was generally set to its maximal value allowed in [43], but the pure Z' signal in ideal delocalization is also shown for $m' = 500 \text{ GeV}$ (top right). The significances s given in the plots are computed according to eqn. (4.16) inside mass intervals which were obtained from the optimization method explained in the text (given in numbers and indicated with the dashed lines). The dramatic significance drop for $m' = 600 \text{ GeV}$ stems from the finite angular resolution of jet pairs on detector level due to the splitting parameter of the jet algorithms (see text, cf. fig. 24 and section 4.1.3).

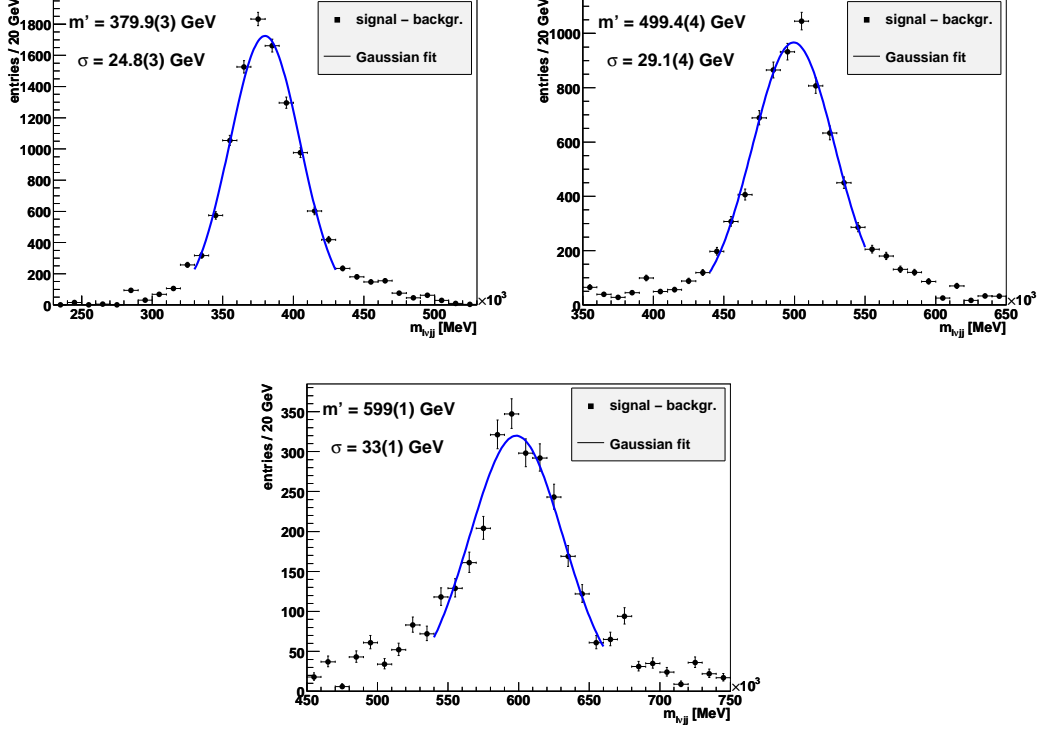


Figure 27: Gaussian fits on the W'/Z' resonance for different mass values $m' = 380, 500$ and 600 GeV in the $lvjj$ final state, with maximal W' coupling to SM fermions allowed by [43].

events over the standard deviation of the background, in the form

$$s \equiv \frac{N}{\sigma_{N_b}} = \frac{N_t - N_b}{\sqrt{2N_b}} \quad (4.16)$$

with the statistical uncertainty

$$\begin{aligned} \sigma_s &= \sqrt{\left(\frac{\partial s}{\partial N_t}\right)^2 \sigma_{N_t}^2 + \left(\frac{\partial s}{\partial N_b}\right)^2 \sigma_{N_b}^2} \\ &= \sqrt{\frac{N_t + N_b}{2N_b} + \left(\frac{N_t + N_b}{2N_b}\right)^2}, \end{aligned} \quad (4.17)$$

where the standard deviation of the total number of events σ_{N_t} has also been scaled according to the doubled background [6]:

$$\sigma_{N_t} = \sqrt{N + 2N_b} = \sqrt{N_t + N_b}. \quad (4.18)$$

The optimal mass interval in which to compute the significance is determined in the following way: The whole mass range $100 \text{ GeV} < m_{l\nu jj} < 1 \text{ TeV}$ is scanned with mass windows of all possible positions and sizes, whereas the window size is formally restricted to a minimal value of 60 GeV in rough correspondence to the resonance widths of the heavy gauge bosons (cf. fig. 27). For each allowed mass window, the significance is then computed according to eqn. (4.16) so that eventually the optimal mass window is defined as the one which conveys the largest value for significance minus statistical error. In the data covering an integrated luminosity of 100 fb^{-1} one finds the numerical results

$$s(m' = 380 \text{ GeV}) = 25.5 (1.5)_{\text{stat}} \sigma \quad \text{within } \{348 \text{ GeV}, 410 \text{ GeV}\} , \quad (4.19)$$

$$s(m' = 500 \text{ GeV}) = 19.7 (1.5)_{\text{stat}} \sigma \quad \text{within } \{468 \text{ GeV}, 547 \text{ GeV}\} , \quad (4.20)$$

$$s(m' = 600 \text{ GeV}) = 9.3 (1.5)_{\text{stat}} \sigma \quad \text{within } \{573 \text{ GeV}, 648 \text{ GeV}\} \quad (4.21)$$

for the combined W'/Z' signal with maximal allowed $g_{W'ff}$, which is way beyond the 5σ discovery threshold at least for the Z' dominating the superposed resonance because of its relatively high production rate, whereas the disproportional significance drop for $m' = 600 \text{ GeV}$ is a direct consequence of the finite angular di-jet resolution at detector level, as explained above in this section. In the ideally delocalized scenario, the significance of the pure Z' signal is

$$s(m' = 500 \text{ GeV}) = 13.4 (1.5)_{\text{stat}} \sigma \quad \text{within } \{465 \text{ GeV}, 557 \text{ GeV}\} . \quad (4.22)$$

In general, the mass windows which are found with the described optimization method have sizes between 2σ and 4σ of the resonance widths as expected, whereas the asymmetry of the position with respect to m' is specific to the region $m' \gtrsim 500 \text{ GeV}$, where the slope of the background is steepest. A detailed summary of the estimated discovery thresholds of both heavy gauge bosons with different mass values and integrated luminosities in the various final states is postponed to section 4.5.

4.2.2 Systematic Uncertainties

Apart from statistical fluctuations, the significances computed in the previous section are in general also afflicted with systematic uncertainties. There are different sources for systematics, which come from the data analysis itself and in case of simulated data also from the data production chain, beginning with the dependency of the production cross sections on the chosen PDF set. With the simplified assumption of a universal scaling $|\varepsilon| \lesssim 10\%$ for signal

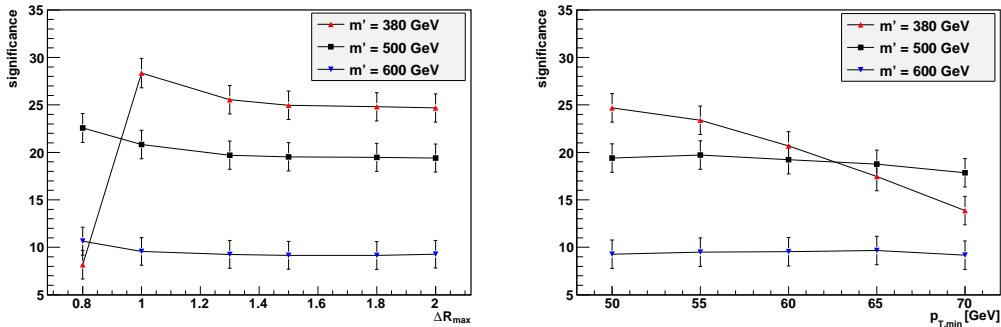


Figure 28: Dependence of the signal significance on the ΔR cut on jet pairs (left) and on the p_T cut (right) for different heavy gauge boson masses. The error bars refer to statistical uncertainties.

and background (cf. table 1 in section 3.2.1), and from the definition of the significance, eqn. (4.16), this uncertainty leads to a scaling of s with the square root of the scale factor,

$$s \rightarrow s\sqrt{1 + \varepsilon} \approx s \left(1 + \frac{\varepsilon}{2}\right), \quad (4.23)$$

corresponding to an effect $\lesssim 5\%$ on the significance. Although this is formally only valid in a fixed mass interval for the computation of s , which is not generally given with the method described above of optimizing the mass interval with respect to s , it turns out that the optimal mass window found by this procedure is perfectly stable against rescaling, so that the scaling behaviour of s given in eqn. (4.23) also applies here. However, it is not at all clear that the signal will scale to the same extent as the background when going to higher orders in the perturbation expansion of the matrix elements. Furthermore, it was already pointed out in section 3.2.1 that the estimation of QCD background contributions may depend strongly on details of the jet simulation procedure such as the specific parton showering scheme applied. Hence, in order to get solid lower bounds of the significances, the background is assumed to scale up with a factor $\lesssim 1.2$ at most while the signal is left constant, which corresponds to a scaling of s with $1/\sqrt{1 + \varepsilon}$, leading to a relative downsizing of the significance by maximally 10% from data production and simulation uncertainties.

Apart from the generation of simulated data, large systematic variations of the significance may also arise from the data analysis itself, e. g. when isolating very small phase space regions with cuts. However, since no critical or extremely restrictive cuts have been applied in this analysis, systematic dependencies of this kind should be generally small, i. e. the signal is assumed

not to vary disproportionately with specific cuts of the analysis. Nonetheless, the robustness of the significance is checked against the two most restrictive cuts, namely the p_T cut and the ΔR cut on jet pairs, cf. eqn. (4.12), to verify this assumption. To this end, the p_T threshold is varied between 50 GeV and 70 GeV with a loose jet separation cut $\Delta R(j, j) < 2.0$, followed by a comparison of the resulting significances. As shown in fig. 28, the significance varies only slightly with the applied p_T cut up to a scale depending on m' where the phase space region of the heavy resonance itself is affected, so that the signal starts to drain and its significance drops. In the cut range considered here this is exactly the case for $m' = 380$ GeV, whereas the significances remain stable for larger masses. Hence the loosest cut $p_T > 50$ GeV is applied in the data analysis to cover the entire range of m' with optimal signal contributions. Finally, the ΔR cut on jets is varied between 1.3 and 2.0 with $p_T > 50$ GeV (fig. 28). As could be expected from fig. 24, this cut is also rather sensitive on the heavy mass m' : The tightening cut first runs into the signal peak for $m' = 380$ GeV, whereas the impact on the signal for $m' = 600$ GeV is only visible with $\Delta R < 1.0$, where the light signal is already lost almost completely.

4.2.3 Disentanglement of Jet Resonances

An important feature of the $l\nu jj$ final state is that it encompasses the decay of both heavy gauge bosons with the same signature, so that the only means of signal discrimination is the disentanglement of the two SM gauge bosons in the di-jet resonance (cf. section 3.2.1). On reco level these resonances have widths which are of the order of the mass splitting itself (cf. fig. 29), which makes it almost impossible to separate them merely by invariant mass cuts. This problem was addressed on parton level in [6], proposing a statistical method to numerically separate the two SM resonances and hence the two heavy resonances: The true gauge boson counts N_W and N_Z within a given sample are smeared over a certain invariant mass range according to the underlying probability functions $p_i(m)$, which can be approximated by a convolution of the intrinsic Lorentz distribution with an experimental detector response function described by a Gaussian distribution. If these $p_i(m)$ are known on reco level, the signal entanglement in the invariant mass range can be thought of as multiplication of the true counts with a statistical transfer matrix T :

$$\begin{pmatrix} \tilde{N}_W \\ \tilde{N}_Z \end{pmatrix} = \begin{pmatrix} T_{WW} & T_{WZ} \\ T_{ZW} & T_{ZZ} \end{pmatrix} \begin{pmatrix} N_W \\ N_Z \end{pmatrix} \quad (4.24)$$

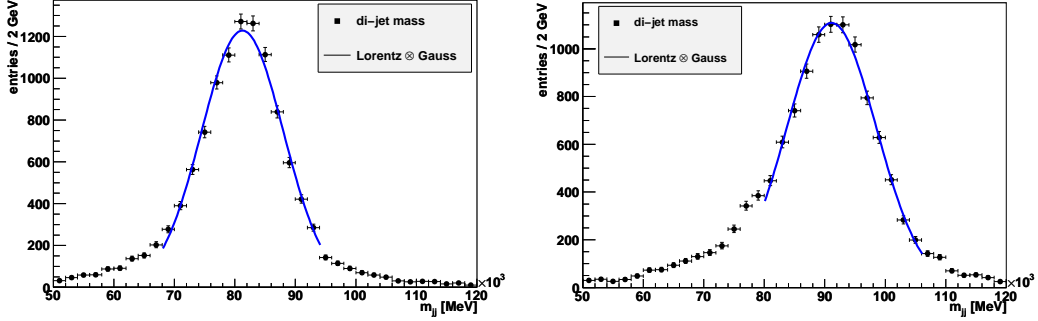


Figure 29: Invariant mass distribution of two jets emerging from the decay of SM gauge bosons (W left, Z right). The jets were reconstructed on reco level with the seeded cone algorithm ($R = 0.4$) on topoclusters, cf. section 4.1.3. The fit function is a convolution of the intrinsic Lorentzian with a Gaussian for experimental resolution.

$$\text{with } T_{ij} \equiv \int_{L_i}^{U_i} dm p_j(m), \quad i, j = W, Z,$$

where the entangled signal counts \tilde{N}_i are to be understood as measured hit counts within an invariant mass cut ranging from L_i to U_i , with contributions from both true signals due to the mass spreading. With the knowledge of the T_{ij} from the $p_i(m)$ and fixed mass windows, the entanglement matrix can be inverted numerically and used to compute the true resonance counts from the measured ones:

$$N_i = \sum_j (T^{-1})_{ij} \tilde{N}_j. \quad (4.25)$$

While in [6] the experimental smearing was roughly accounted for on parton level by a Gaussian distribution with a width of 10 GeV, the approach pursued here on reco level is to use the samples with reconstructed hadronic decays of SM gauge bosons from section 4.1.3 in order to fit the resonances with a convolution of the intrinsic Lorentzian with known width (e. g. from [37]) and the experimental Gaussian with unknown width σ_i . This is done separately for each SM boson to get to know the factual smearings as exactly as possible (cf. fig. 29). From the fit results,

$$\begin{aligned} m_W &= 81.26(8) \text{ GeV}, & m_Z &= 91.2(1) \text{ GeV}, \\ \sigma_W &= 6.76(8) \text{ GeV}, & \sigma_Z &= 7.3(1) \text{ GeV}, \end{aligned} \quad (4.26)$$

and the cut windows chosen as

$$L_W = 60 \text{ GeV}, \quad U_W = L_Z = \frac{m_W + m_Z}{2}, \quad U_Z = 111 \text{ GeV}, \quad (4.27)$$

the T matrix and its inversion can be computed numerically:

$$T \approx \begin{pmatrix} 0.72 & 0.27 \\ 0.24 & 0.69 \end{pmatrix} \quad \text{giving} \quad T^{-1} \approx \begin{pmatrix} 1.6 & -0.62 \\ -0.55 & 1.7 \end{pmatrix}. \quad (4.28)$$

The uncertainty of T^{-1} is estimated by inserting the extremal values allowed from the uncertainties of the fit parameters, i. e. smallest mass separation with largest widths for maximal entanglement and largest mass separation with smallest widths for minimal entanglement, which results in absolute uncertainties for all matrix elements of roughly $\sigma_{T^{-1}} \approx 0.04$.

In order to evaluate the significance of each disentangled signal, the standard deviation of the N_i is now computed from eqn. 4.25, giving

$$\begin{aligned} \sigma_{N_i} &= \sqrt{\sum_j (T_{ij}^{-1})^2 \sigma_{N_j}^2 + \sigma_{T^{-1}}^2 \sum_j \tilde{N}_j^2} \\ &= \sqrt{\sum_j (T_{ij}^{-1})^2 (N_{t,j} + 3N_{b,j}) + \sigma_{T^{-1}}^2 \sum_j (N_{t,j} - N_{b,j})^2} \\ &\simeq \sqrt{\sum_j (T_{ij}^{-1})^2 (N_{t,j} + 3N_{b,j})}, \end{aligned} \quad (4.29)$$

where the definition $\tilde{N}_i = N_{t,i} - N_{b,i}$ has been plugged in analog to eqn. (4.14) together with the doubled background counting for the errors on $N_{t,i}$ and $N_{b,i}$ as described in section 4.2.1. The uncertainty of the T^{-1} matrix elements gives a numerically small contribution compared to the statistical uncertainty of \tilde{N}_i and has therefore been neglected in the last line of eqn. (4.29).

The relevant signal events are now isolated by cutting on the invariant mass $m_{\nu jj}$ within a region of ± 30 GeV around the heavy resonance, where $m' = 500$ GeV was chosen here for an upper benchmark of the method, because a medium value of m' allows for the largest absolute values of $g_{W'ff}$ (cf. fig. 6 and [43]) and hence possesses the highest discovery potential [6]. After this cut, the SM gauge boson resonances are examined in the invariant mass distributions m_{jj} of the corresponding jet pairs (cf. fig. 30). From

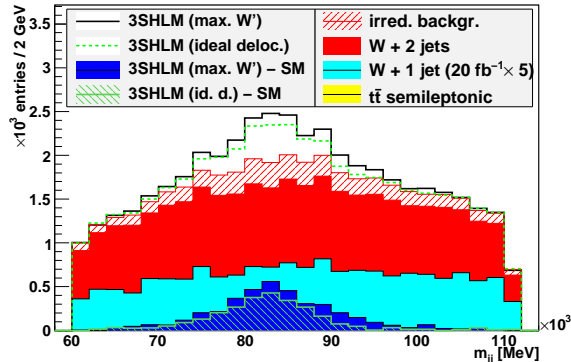


Figure 30: Invariant mass distribution of the jet pairs in events contributing to the heavy gauge boson resonance with $m' = 500$ GeV.

eqns. (4.25) and (4.29), the significances of the W and Z signals are in this case defined as

$$\tilde{s}_i \equiv \frac{\tilde{N}_i}{\sigma_{\tilde{N}_i}} \quad \text{and} \quad s_i \equiv \frac{N_i}{\sigma_{N_i}}, \quad (4.30)$$

to be evaluated from the total hits $N_{t,i}$ and the background hits $N_{b,i}$ inside the respective mass windows given in eqn. (4.27). The whole procedure is carried out with maximal $g_{W'ff}$ as well as in ideal delocalization for a cross-check. As detailed in table 3, the Z significance, implying the decay of a W' , does indeed drop to nearly zero in ideal delocalization, while a significance

$$s_Z(m' = 500 \text{ GeV}) = 1.4 (1.0)_{\text{stat}} \sigma \quad (4.31)$$

remains with maximal $g_{W'ff}$. In the parton level analysis of [6] a significance of $\sim 2\sigma$ was found for the disentangled Z signal, whereas the basic differences between their analysis and this one are that the detector width of SM bosons in jet pairs was somewhat overestimated with 10 GeV, while, on the other hand, the considerably large background contributions of inclusive jet production at the detector could not be incorporated on parton level. In any case, this result is still far away from a liable discovery threshold for an integrated luminosity of 100 fb^{-1} considered here, so that at least a factor 2 or 3 in the statistics and hence ATLAS run time would be necessary to get the disentangled W' signal significant in the $l\nu jj$ channel. It therefore suggests itself to analyze other channels with a clean W' signal in order to improve its overall discovery chances.

ideal delocalization					maximal $g_{W'ff}$				
i	\tilde{N}_i	\tilde{s}_i	N_i	s_i	i	\tilde{N}_i	\tilde{s}_i	N_i	s_i
W	1992	6.8	2771	5.6	W	2585	8.8	3334	6.7
Z	693	2.4	1	0.001	Z	1336	4.6	717	1.4

Table 3: Signal events and significances as computed from eqn. (4.30) before and after the signal disentanglement described in the text, in ideal delocalization (left) and with maximal W' coupling to SM fermions (right). The significance also drops for the W signals because the error generally becomes larger in the disentanglement procedure [6].

4.3 $lljj$ Channel

The $lljj$ channel is somewhat easier to handle than the $l\nu jj$ channel of the previous section, because all final state objects are visible in the detector, so that their momenta can in principle be uniquely determined from detector data. Moreover, this channel contains a pure W' signal, thus conveying an additional possibility to discriminate the one-loop results of [43] from the ideal delocalization scenario of [1], where the W' resonance should vanish completely.

The event selection criteria are similar to those of the $l\nu jj$ final state: Basically two oppositely charged boosted leptons passing all kinematic cuts of eqn. (3.10) are demanded in this case instead of just one, together with a cut on the invariant di-lepton mass within $\sim 2\sigma$ around the Z mass (cf. sections 4.1.1 and 4.1.2),

$$\begin{aligned}
81 \text{ GeV} &< m_{\mu\mu} < 101 \text{ GeV} , \\
86 \text{ GeV} &< m_{ee} < 96 \text{ GeV} .
\end{aligned}
\tag{4.32}$$

Moreover, since two measured lepton momenta are available in this case, the effect of a tight collinearity cut on the lepton pairs similar to the one on jet pairs is probed, in order to further suppress irreducible background. However, fig. 31 illustrates that the situation is by far not as unambiguous for the leptons as for the jet pairs in the $l\nu jj$ channel, majorly because of the bad statistics combined with a relatively small signal in the $lljj$ channel, so that the corresponding cut is left loose in this case,

$$\Delta R(l, l) < 2.0 .
\tag{4.33}$$

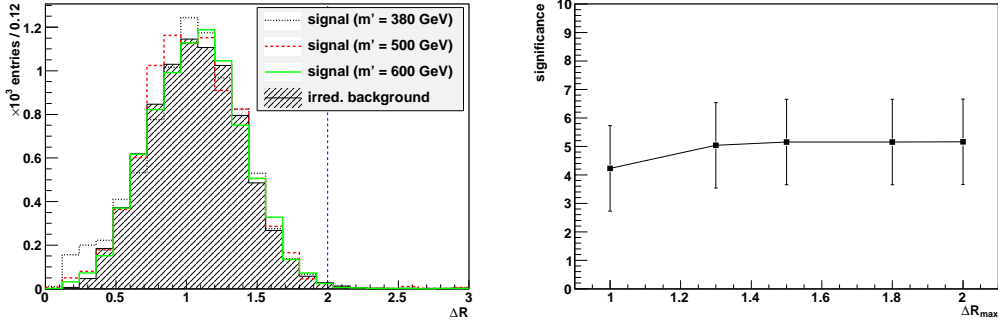


Figure 31: Distribution of the enclosed angle of two muons for different values of m' with maximal $g_{W'ff}$ in the $lljj$ channel (left) and dependence of the signal significance on the applied ΔR cut for $m' = 500 \text{ GeV}$ (right, statistical uncertainty marked with error bars). For the other two values of m' the signal is not significant in this channel.

The requirements on hadron jets are left the same except for the cut window on the di-jet mass, which is adapted to

$$70 \text{ GeV} < m_{jj} < 90 \text{ GeV} , \quad (4.34)$$

because the di-jet resonance in the $lljj$ signal stems exclusively from W bosons (cf. fig. 12). Finally, the sum of the lepton momenta and the sum of the jet momenta should also pass the back-to-back cut of eqn. (4.13).

When analyzing the distribution of the invariant mass m_{lljj} of the four final state momenta in order to isolate the W' signal, two serious drawbacks of this channel become obvious: The cross sections of this final state are in general roughly five times smaller than for $l\nu jj$, which leads to a significant lack of statistics in the 100 fb^{-1} samples, so that the suppression of background fluctuations is far worse than in the $l\nu jj$ channel. Secondly, the signal itself is also very small, if existent at all, because of the strong experimental constraints on $g_{W'ff}$. In summary, it must be coped with a tiny signal superposed with a comparably large but still strongly fluctuating background. In order to somewhat improve the results without giving up on the basic condition to perform this analysis with an integrated luminosity of 100 fb^{-1} , the following approach is pursued: The signal and irreducible background sample, covering 100 fb^{-1} , is summed with reducible background samples which also strictly cover 100 fb^{-1} only. On the other hand, when summing the reducible backgrounds with the irreducible background from generated SM data to account for the SM expectation of the analysis, the corresponding m_{lljj} distributions are smoothed by generating higher luminosities and scaling them down to

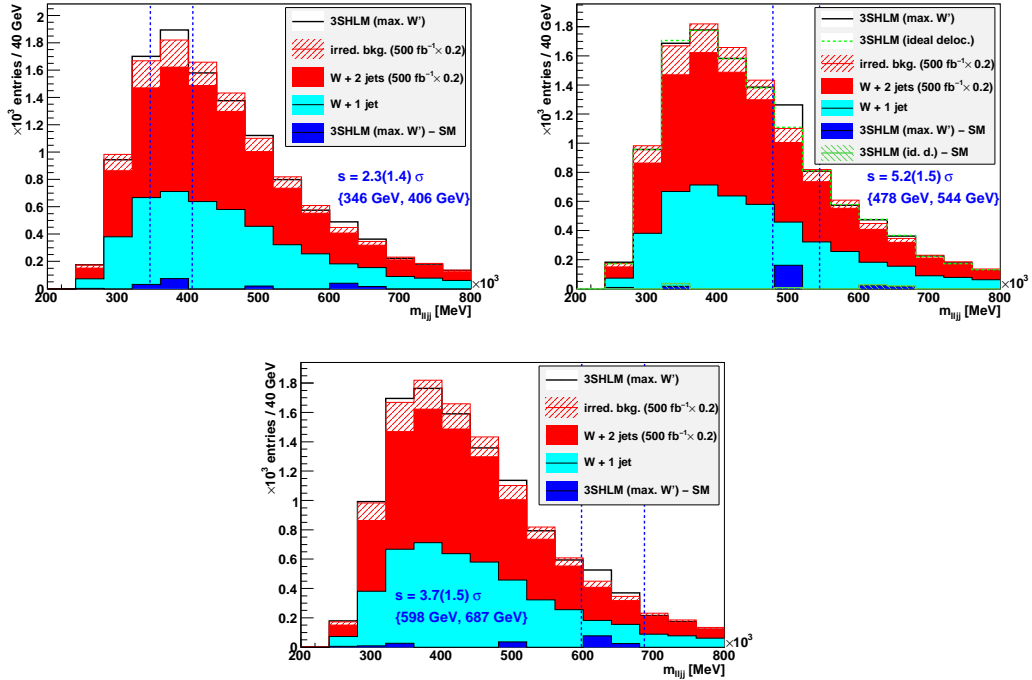


Figure 32: W' signal and background samples corresponding to 100 fb^{-1} in the $lljj$ channel with maximal $g_{W'ff}$, for heavy gauge boson masses $m' = 380 \text{ GeV}$ (top left), 500 GeV (top right) and 600 GeV (bottom). For $m' = 500 \text{ GeV}$, which is the only sample to convey a significant signal, the vanishing of the W' signal in the ideally delocalized scenario is also shown.

100 fb^{-1} whenever necessary, i. e. the irreducible and reducible two-parton backgrounds are produced in samples covering 500 fb^{-1} while the reducible one-parton background is already more or less smooth for 100 fb^{-1} . Now the strongly fluctuating signal/background distribution of m_{lljj} is compared with a rather smooth SM expectation to isolate the W' resonance, if existent, and compute corresponding significances (cf. fig. 32).

Since no neutrino reconstruction and hence no double-counting of the background occurs in this final state, the standard deviation of the number of total and background events simply follows from Poisson statistics, so that the significance of the W' signal is in this case just given by [6]

$$s = \frac{N}{\sigma_{N_b}} = \frac{N_t - N_b}{\sqrt{N_b}} \quad (4.35)$$

with a statistical uncertainty analog to eqn. (4.17),

$$\sigma_s = \sqrt{\frac{N_t}{N_b} + \left(\frac{N_t + N_b}{2N_b}\right)^2}, \quad (4.36)$$

whereas the mass window in which to collect the hit numbers N_t and N_b and evaluate s is again optimized with the method described in section 4.2.1. As shown in fig. 32, the W' signal with $m' = 500$ GeV acquires a significance

$$s(m' = 500 \text{ GeV}) = 5.2 (1.5)_{\text{stat}} \sigma \quad \text{within } \{478 \text{ GeV}, 544 \text{ GeV}\}. \quad (4.37)$$

in the one-loop scenario of [43] with maximal allowed $g_{W'ff}$, which just about corresponds to a 3σ discovery with the systematic uncertainty taken into account, while in the ideally delocalized scenario the signal expectedly vanishes. For the other two values of m' examined here $g_{W'ff}$ is even more restricted, which results in the perishing of the according signals among the large background fluctuations in the 100 fb^{-1} samples. It can be concluded that even in this channel, which conveys a clean W' signal, it is rather critical even to make a 3σ discovery of the W' within the first 100 fb^{-1} of ATLAS data due to the poor signal-to-background ratio in combination with small overall cross sections, and may depend on the actual mass of the W' .

4.4 $l\nu ll$ Channel

Another chance for a discriminative search for the heavy W' is the purely leptonic final state $l\nu ll$, which possesses by far the smallest cross section but at the same time a very clean detector signature compared to the semi-leptonic channels considered above. The event selection requirements are in this case exactly three isolated charged leptons passing the kinematic cuts in eqn. (3.10) as well as missing transverse momentum passing the p_T cut. The further procedure simply is to combine the treatments of one or two charged leptons discussed in the previous sections: With mixed flavors, the lepton pair of equal flavor is required to have opposite charge signs and the kinematic topology corresponding to the decay of a boosted gauge boson, i. e. pass the invariant mass and collinearity cuts pointed out in eqns. (4.32) and (4.33), while the third lepton of different flavor is demanded to reconstruct at least one neutrino momentum together with \cancel{E}_T (cf. section 4.1.4) which also passes the kinematic cuts (and the W mass cut in case of a c neutrino). With three leptons of equal flavor, the procedure is to demand mixed charges and pick from the two possible pairs of oppositely charged leptons the one which passes the said Z mass and collinearity cuts, whereas

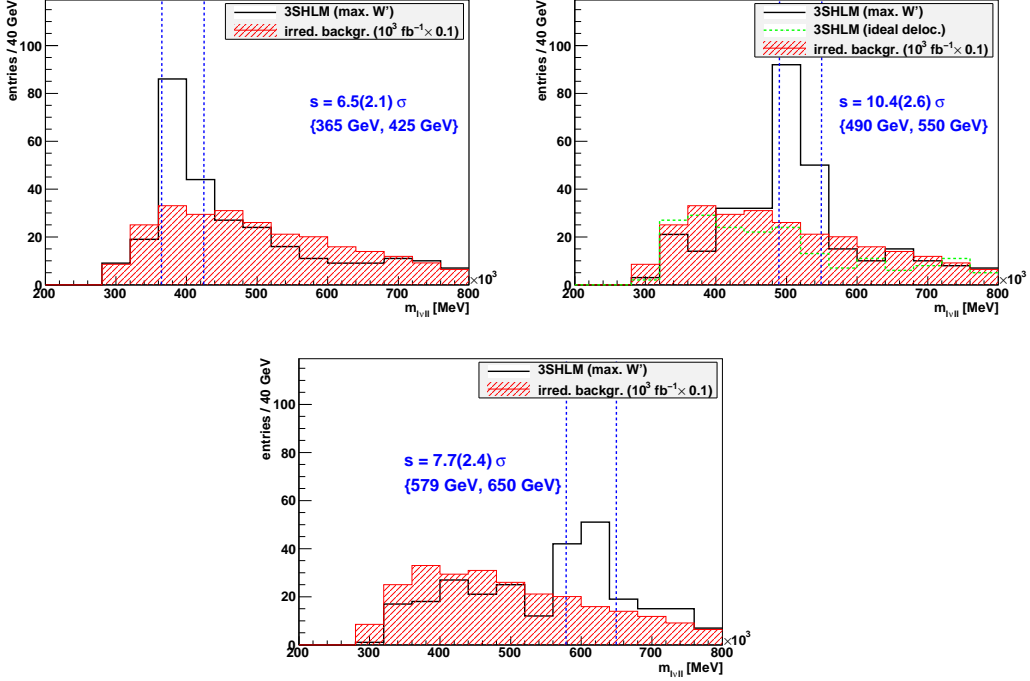


Figure 33: W' signal and SM expectation in the $l\nu ll$ final state, for $m' = 380$ GeV (top left), 500 GeV (top right) and 600 GeV (bottom), in each case with maximal $g_{W'ff}$. The vanishing of the signal in ideal delocalization is also shown for $m' = 500$ GeV (top right).

the remaining lepton is then required to produce at least one reasonable neutrino momentum together with \cancel{E}_T . As usual, the reconstructed SM gauge boson momenta should in any case also pass the back-to-back cut of eqn. (4.13).

When matching the signal expectation in the 3SHLM with the SM expectation in order to evaluate significances, the situation turns out to be quite simple here: When dealing with electrons and muons exclusively, it is basically possible to identify the final states on matrix element level at the detector, so that the potential background is greatly dominated by irreducible contributions. For example, in this case the only reducible backgrounds would come from the loss of a lepton in a four-lepton final state or from a two-lepton final state with another isolated fake lepton. All of these processes are orders of magnitude smaller than the irreducible background of the $l\nu ll$ final state, either because of small cross sections or detector performance, so that they can be readily neglected here. However, the problem of statistical fluctuations is even worse here than for $lljj$ due to the tiny cross

section of this final state, which requires a smoothing of the irreducible background analog to the procedure in the previous section. In this case, 10^3 fb^{-1} of data have been generated, simulated and scaled down to be compared with the signal sample covering 100 fb^{-1} (cf. fig. 33), where the significances are computed in the same way as for $l\nu jj$, using eqn. (4.16) together with an optimized mass interval. The corresponding numerical results are

$$s(m' = 380 \text{ GeV}) = 6.5 (2.1)_{\text{stat}} \sigma \quad \text{within } \{365 \text{ GeV}, 425 \text{ GeV}\} , \quad (4.38)$$

$$s(m' = 500 \text{ GeV}) = 10.4 (2.6)_{\text{stat}} \sigma \quad \text{within } \{490 \text{ GeV}, 550 \text{ GeV}\} , \quad (4.39)$$

$$s(m' = 600 \text{ GeV}) = 7.7 (2.4)_{\text{stat}} \sigma \quad \text{within } \{579 \text{ GeV}, 650 \text{ GeV}\} , \quad (4.40)$$

hence all reaching the region just between the 3σ and 5σ discovery threshold when systematic and statistical uncertainties are taken into account. In fact, the different significances show the expected relative pattern for the various values of the heavy mass parameter, with the best discovery prospects for a medium value around $m' \sim 500 \text{ GeV}$, which allows for the largest $g_{W'ff}$ values, and somewhat smaller significances for the light and the heavy W' . Finally, it is noteworthy that in the purely leptonic final state the signal remains stable for $m' \gtrsim 500 \text{ GeV}$ in contrast to the semi-leptonic channels, because the resolution of the angular di-lepton separation is by far not limited as strongly as for jet pairs.

4.5 Significances and Discovery Thresholds

This section is intended to summarize and generalize the results of the heavy gauge boson searches in the different final states discussed in sections 4.2 – 4.4. For all signal significances, the statistical uncertainties are combined quadratically with the estimation of the systematic uncertainty described in section 4.2.2 in order to get a solid lower threshold of the significance values. Furthermore, it is distinguished between the ideal delocalization scenario introduced in [1] on tree level and the one-loop scenario of [43] with maximal allowed W' coupling to SM fermions.

Ideal Delocalization With a strictly fermiophobic W' in the ideally delocalized scenario, all W' signals naturally vanish in the different final states. This is of course no surprise in the $lljj$ and $l\nu ll$ channels with pure W' resonances, whereas in the $l\nu jj$ channel the dropping of the W' significance into the $\ll 1\sigma$ region after the disentanglement procedure introduced in section 4.2.3 can be seen as an argument for the general liability of the procedure itself. The remaining signal in the $l\nu jj$ channel stems from the Z' boson, conveying a significance of $13.4 (1.5)_{\text{stat}} \sigma$ for $m' = 500 \text{ GeV}$ with an integrated

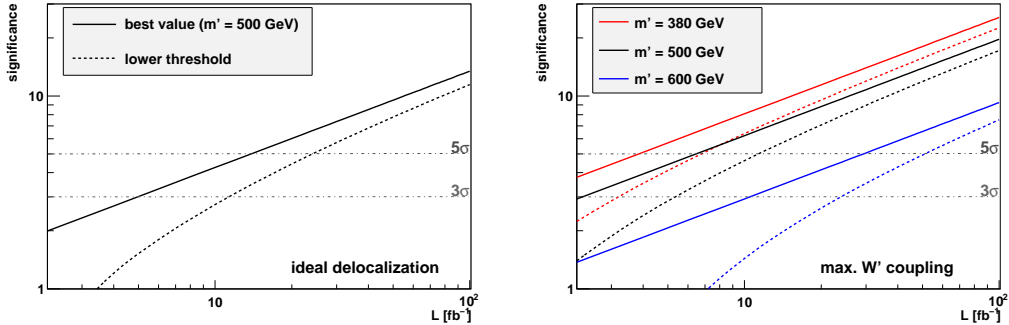


Figure 34: Signal discovery thresholds in the $l\nu jj$ channel, for ideal delocalization, i. e. pure Z' signal (left) and maximal W' coupling to SM fermions (right), as extrapolated from 100 fb^{-1} of simulated data. The continuous lines indicate the significances computed from data in each case, whereas the dashed lines denote the lower significance limits with statistical and systematic uncertainties taken into account.

luminosity of 100 fb^{-1} , which is way beyond the 5σ discovery threshold. The high statistics in this channel allows for the usage of the scaling law in eqn. (4.23) to extrapolate the significance to smaller integrated luminosities and thus estimate the luminosity necessary for the Z' signal to just pass the discovery threshold. Note that the systematic uncertainty is assumed as 10% relative to s and hence scales down along with s , whereas the absolute statistical uncertainty remains constant in this procedure, cf. eqn. (4.17). As illustrated in fig. 34, an integrated luminosity of $15\text{--}20 \text{ fb}^{-1}$ could suffice to discover a relatively light Z' ($m' \lesssim 500 \text{ GeV}$) in the ideally delocalized scenario with 5σ confidence at the ATLAS detector, in agreement with the worst-case results of the parton level analysis carried out in [6]. For higher mass values, however, the discovery prospects of this analysis begin to suffer severely from the fundamental problem of separating highly collinear hadron jets with a finite angular resolution (cf. section 4.2.1 and fig. 24 as well as the next paragraph).

Almost Fermiophobic W' In the one-loop scenario introduced in [43], where a vanishing coupling of the W' to SM fermions is excluded from experimental precision data, the finite W' contribution to the signal in the $l\nu jj$ final state further increases the observed significances. With the maximal $g_{W'ff}$ allowed by precision data, the 5σ discovery threshold for the signal in the $l\nu jj$ channel may drop below 10 fb^{-1} , even down to 5 fb^{-1} , as long as the heavy gauge bosons are comparably light ($m' \lesssim 500 \text{ GeV}$), cf. fig.

34. However, the picture is rather different for $m' = 600 \text{ GeV}$, showing a 5σ discovery threshold of at least $40\text{--}50 \text{ fb}^{-1}$. This result illustrates the general notion that above $m' \sim 500 \text{ GeV}$ the discovery threshold starts to grow disproportionately with increasing mass parameter, at least in the approach pursued in this analysis, because it is more and more problematic to separately reconstruct the two parton momenta of the semi-leptonic channels on detector level: The angular separation of the original partons simply becomes too small for the jet algorithms with splitting parameter $R = 0.4$ to split the calorimeter signals of the partons into two separate hadron jets, so that the signal is majorly lost when requiring two hard jets for event selection. A possible loophole for this problem—which is not addressed any further in this thesis—would be to downsize the splitting parameter of the jet algorithms. However, this is a highly non-trivial step because the general jet calibration seems to depend on this parameter, as indicated by the results in section 4.1.3 and fig. 18. Another approach, pointed out in [3], is to entirely give up on the ambition to resolve the detector signal of the two strongly boosted partons into two individual jets and rather treat it as one compound jet with an invariant mass close to the W mass and an angular size corresponding to the original separation of the partons.

In any case, once the Z' is discovered in the $l\nu jj$ channel, the pure W' channels $lljj$ and $l\nu ll$ as well as the disentanglement procedure in the $l\nu jj$ channel can be used to discriminate the different scenarios that may be present in nature, i. e. ideal delocalization or finite couplings of the SM fermions to the charged heavy gauge bosons. However, considering the respective results of this analysis, it may take quite some time before the integrated luminosity required for a solid 5σ discovery of the W' is collected at the ATLAS detector. On the grounds of this thesis, it can be stated that the disentanglement procedure in the $l\nu jj$ channel certainly offers the worst discovery prospects: The 100 fb^{-1} data samples examined here turn out to be way too small for a reliable W' discovery, irrespective of the actual point in the parameter space of the 3SHLM. In the $lljj$ channel, even a 3σ discovery of the W' within the first 100 fb^{-1} of data can only be expected for a medium value of m' around 500 GeV . It may be concluded that the leptonic channel $l\nu ll$ presents the only alternative which offers a realistic chance for a 5σ discovery of the W' with an integrated luminosity $\lesssim 100 \text{ fb}^{-1}$. Systematic uncertainties taken into account, it is the only of all examined W' channels where the signal significance robustly passes the 3σ threshold in the entire m' range considered, while for medium values of m' even the 5σ threshold may be reached within the first $70\text{--}80 \text{ fb}^{-1}$ of ATLAS data.

Conclusions

This thesis encompasses theoretical, phenomenological and experimental aspects of the “Three-Site Higgsless Model” (3SHLM) introduced in [1]. The model represents a minimal effective approach to extend the Standard Model (SM), conveying a dynamic mechanism for the spontaneous breaking of the electroweak gauge symmetry of the SM, which is experimentally confirmed by the existence of the massive gauge bosons W and Z , via the insertion of one additional $SU(2)$ gauge factor into the electroweak gauge group. Hence it represents the minimal deconstructed limit of a general class of compactified five-dimensional gauge theories, which all share the phenomenological prediction of additional Kaluza-Klein modes of the SM fields. In the special case of the maximally deconstructed 3SHLM considered here, only one set of additional modes remains in the spectrum, whereas the new set of gauge bosons W' and Z' will deliver the dominant signatures of the model at LHC energies.

The theoretical upper bound for the validity of the SM without any yet undiscovered physics contributions is given by the energy scale of unitarity violation in scattering amplitudes involving the longitudinal gauge boson modes which come along with the spontaneous breaking of local symmetries [23, 24]. Any extension of the SM, such as the 3SHLM, should not only address the symmetry-breaking mechanism itself but also the impact of the new physics on these unitarity-violating amplitudes. In this thesis, the basic mechanism leading to unitarity violation in the SM is extensively reviewed, verifying the linear divergence of top pair annihilation into gauge bosons as well as the quadratic divergence of elastic and quasi-elastic $2 \rightarrow 2$ gauge boson scattering with respect to the CMS energy, which fixes the upper validity bound of the SM to 1.2 TeV. On the grounds of these considerations, the leading-order effect of the new gauge bosons of the 3SHLM on the $2 \rightarrow 2$ scattering amplitudes of SM gauge bosons is computed explicitly, resulting in a delay of unitarity violation by a factor 2 at most. On principle, the factual amount of this delay largely depends on the mass parameter m' of the new, practically degenerate gauge bosons, so that the requirement of delaying unitarity violation within the 3SHLM automatically sets a theoretical upper bound to the said mass parameter m' in the region of the SM consistency limit mentioned above.

The lower bounds of any new physics generally come from experimental results. In the case of the 3SHLM, the new degrees of freedom associated with the extended electroweak gauge group are severely constrained by experimental bounds on electroweak precision observables as determined at the electron-positron collider LEP [38]. These electroweak precision tests

basically have two immediate consequences for the phenomenology of the 3SHLM: Firstly, the masses of all new particles are bounded from below, with $m' > 380$ GeV for the heavy gauge bosons and $M > 3$ TeV for the heavy fermions [1]. Secondly, the coupling of the heavy charged gauge boson W' to the SM fermions must vanish on tree level [1] or at least be very small, $\sim 1\%$ of the coupling of the SM W , according to a one-loop analysis in [43].

With the parameter space bounded this way, the 3SHLM offers a rather unique signature of exclusively one neutral and possibly one charged vector resonance in the energy range of the new proton-proton collider LHC at CERN, which is just about to be launched for data taking. This gave rise to the implementation of the model into the parton level Monte Carlo generator WHIZARD [7] in order to perform a parton level analysis addressing the discovery potential of the heavy gauge bosons at LHC experiments, whereas s channel production and subsequent semi-leptonic decay via the greatly dominant intermediate states $Z' \rightarrow WW$ and $W' \rightarrow WZ$ was considered most promising [6]. The parton level analysis is verified in this thesis with simulated detector data of the ATLAS detector [2, 4, 5], whereas the semi-leptonic final states νjj and $lljj$ considered in [6] are complemented by the purely leptonic final state νll . To that end, WHIZARD was used to generate signal and background samples covering an integrated luminosity of 100 fb^{-1} for $m' = 380, 500$ and 600 GeV with maximal $g_{W'ff}$ allowed in the one-loop scenario [43] as well as in the ideally delocalized scenario [1] for $m' = 500$ GeV as a cross-check. The parton level samples were hadronized with PYTHIA [30] and simulated with the ATLAS detector simulation ATLFast-2 [10], whereas the heavy resonances in the invariant mass distributions of the four final-state objects on detector level are examined in order to quantify the discovery potential.

The only promising final state with a Z' contribution is νjj , where the superposed Z'/W' signal is estimated to cross the 5σ threshold after the first $5\text{--}20 \text{ fb}^{-1}$ of ATLAS data, depending on the actual value of $g_{W'ff}$. Once the robustly coupling Z' is discovered in the νjj channel, several alternatives exist to discriminate the ideally delocalized scenario from the one-loop scenario with a finite $g_{W'ff}$. The method proposed in [6] of statistically disentangling the superposed signal in the νjj channel turns out to be the least feasible for this task, conveying significances far below the discovery thresholds for the disentangled W' signal in the 100 fb^{-1} samples. The other semi-leptonic channel $lljj$ already leads the W' signal very close to the 3σ threshold, at least for a medium $m' \sim 500$ GeV. Finally, the purely leptonic channel νll has the best prospects of discovering the W' with no more than 100 fb^{-1} of data: The significance exceeds 3σ for all values of m' considered, and a 5σ discovery may even be possible with $70\text{--}80 \text{ fb}^{-1}$ when $m' \sim 500$ GeV.

References

- [1] R. S. Chivukula et al.: *Phys. Rev. D* **74**, 075011 (2006).
- [2] ATLAS Collaboration (G. Aad et al.): *ATLAS Technical Design Report – Volume I*, CERN/LHCC 99-14 (1999).
- [3] ATLAS Collaboration (G. Aad et al.): *ATLAS Technical Design Report – Volume II*, CERN/LHCC 99-15 (1999).
- [4] ATLAS Collaboration (G. Aad et al.): *JINST* **3**, S08003 (2008).
- [5] ATLAS Collaboration (G. Aad et al.): *Expected Performance of the ATLAS Experiment – Detector, Trigger and Physics*, arXiv:0901.0512v4 [hep-ex] (2009).
- [6] T. Ohl, C. Speckner: *Phys. Rev. D* **78**, 095008 (2008).
- [7] W. Kilian, T. Ohl, J. Reuter: arXiv:0708.4233 [hep-ph] (2007).
- [8] Z. Marshall (for the ATLAS Collaboration): ATL-SOFT-PROC-2008-001 (2008); K. Assamagan et al.: ATL-COM-SOFT-2008-024 (2008).
- [9] E. Barberio et al.: ATL-SOFT-CONF-2007-002 (2007); ATLFast-II benchmark group (D. Adams et al.): ATL-COM-PHYS-2009-554 (2009).
- [10] twiki.cern.ch/twiki/bin/view/Atlas.
- [11] E. Fermi: *Z. Physik* **88**, 161 (1934).
- [12] S. L. Glashow: *Nucl. Phys.* **22**, 579 (1961).
- [13] Gargamelle Collaboration (F. J. Hasert et al.): *Phys. Lett. B* **46**, 138 (1973).
- [14] UA1 Collaboration (G. Arnison et al.): *Phys. Lett. B* **126**, 398 (1983).
- [15] S. Weinberg: *Phys. Rev. Lett.* **19**, 1264 (1967).
- [16] A. Salam: *Weak and Electromagnetic Interactions*, in *Elementary Particle Theory (Nobel Symposium No. 8)*, edited by N. Svartholm (Almquist and Wiksell, Stockholm, 1968), p. 367.
- [17] S. Weinberg: *Phys. Rev. Lett.* **17**, 616 (1966).
- [18] M. Chanowitz, M. Golden, H. Georgi: *Phys. Rev. D* **36**, 1490 (1987).

- [19] J. M. Cornwall, D. N. Levin, G. Tiktopoulos: *Phys. Rev. D* **10**, 1490 (1974).
- [20] C. E. Vayonakis: *Lett. Nuov. Cim.* **17**, 383 (1976).
- [21] P. W. Higgs: *Phys. Rev. Letters* **12**, 132 (1964).
- [22] P. W. Higgs: *Phys. Rev. Letters* **13**, 508 (1964).
- [23] B. W. Lee, C. Quigg, H. B. Thacker: *Phys. Rev. Lett.* **38**, 883 (1977).
- [24] B. W. Lee, C. Quigg, H. B. Thacker: *Phys. Rev. D* **16**, 1519 (1977).
- [25] S. Weinberg: *Phys. Rev. D* **13**, 974 (1976).
- [26] S. Dimopoulos, L. Susskind: *Nucl. Phys. B* **155**, 237 (1979).
- [27] L. Randall, R. Sundrum: *Phys. Rev. Letters* **83**, 3370 (1999).
- [28] J. M. Maldacena: *Adv. Theor. Math. Phys.* **2**, 231 (1998), *Int. J. Theor. Phys.* **38**, 1113 (1999).
- [29] CMS Collaboration (G. L. Bayatian et al.): *J. Phys. G* **34**, 995 (2007).
- [30] T. Sjöstrand, S. Mrenna, P. Skands: *JHEP* **05**, 026 (2006).
- [31] M. E. Peskin, D. V. Schroeder: *An Introduction to Quantum Field Theory*, Reading (MA), Addison-Wesley, 5th (corr.) printing (1997).
- [32] W. Kilian: *Electroweak Symmetry Breaking – The Bottom-Up Approach*, New York (NY), Springer, 1st edition (2003).
- [33] J. J. Sakurai: *Modern Quantum Mechanics*, Reading (MA), Addison-Wesley, revised edition (1994).
- [34] E. Boos et al.: *Phys. Rev. D* **57**, 1553 (1998).
- [35] R. Foadi, C. Schmidt: *Phys. Rev. D* **73**, 075011 (2006).
- [36] R. S. Chivukula et al.: *Phys. Rev. D* **75**, 075012 (2007).
- [37] Particle Data Group (C. Amsler et al.): *Phys. Lett. B* **667**, 1 (2008).
- [38] The LEP Collaborations (ALEPH, DELPHI, L3, OPAL, the LEP Electroweak Working Group, the SLD Electroweak, Heavy Flavour Groups): arXiv:0312023v2 [hep-ex] (2004).

- [39] M. E. Peskin, T. Takeuchi: *Phys. Rev. D* **46**, 381 (1992).
- [40] R. Barbieri et al.: *Nucl. Phys. B* **703**, 127 (2004).
- [41] R. S. Chivukula et al.: *Phys. Rev. D* **72**, 015008 (2005).
- [42] R. S. Chivukula et al.: *Phys. Rev. D* **72**, 095013 (2005).
- [43] T. Abe, S. Matsuzaki, M. Tanabashi: *Phys. Rev. D* **78**, 055020 (2008).
- [44] D. H. Perkins: *Introduction to High Energy Physics*, Cambridge, Cambridge Univ. Press, 4th edition (2000).
- [45] J. v.Loeben: *Diplomarbeit* “Test und Kalibrierung der Präzisionsdriftrohrkammern des ATLAS-Myonspektrometers”, MPP München (2006).
- [46] S. Gieseke, T. Ohl, W. Kilian: *Lectures at the 2nd Terascale Monte Carlo School*, April 20–23 2009, DESY Hamburg (2009); slides on indico.desy.de/conferenceDisplay.py?confId=1583.
- [47] M. Moretti, T. Ohl, J. Reuter: arXiv:0102195v1 [hep-ph] (2001).
- [48] Jon Pumplin et.al.: arXiv:0512167 [hep-ph] (2005).
- [49] A. D. Martin et al.: *Phys. Lett. B* **604**, 61 (2004).
- [50] G. Corcella et al.: *JHEP* **01**, 010 (2001); arXiv:0210213 [hep-ph] (2002).
- [51] E. Boos et al.: arXiv:0109068 [hep-ph] (2001).
- [52] GEANT4 Collaboration (S. Agostinelli et al.): *Nuclear Instruments and Methods in Physics Research A* **506**, 250 (2003).
- [53] root.cern.ch.
- [54] [twiki.cern.ch/twiki/bin/view/AtlasProtected/MSSMHiggsToTauTauToLH-14TeV](http://twiki.cern.ch/twiki/bin/view/AtlasProtected/MSSMHiggsToTauTauToLH14TeV).
- [55] T. Gleisberg et al.: *JHEP* **04**, 056 (2004).
- [56] M. Cacciari, G. P. Salam: *Phys. Lett. B* **641**, 57 (2006).
- [57] M. Cacciari, G. P. Salam, G. Soyez: *JHEP* **08**, 063 (2008).

List of Figures

1	Feynman diagrams for the self-coupling vertices of gauge bosons in non-Abelian gauge theories. The arrows indicate the 4-momentum flows chosen to derive the Feynman rules, and the numbers enumerate all relevant properties of the gauge bosons (4-momentum, Lorentz index and gauge index), as consistent with the conventions pointed out in appendix A.	12
2	Potentially divergent $t\bar{t}$ annihilation diagrams. The contributions depend on the initial chiralities: s -channel gauge boson propagation works only with mixed initial chirality (left), t -channel b exchange is possible only for left-handed initial particles (right).	32
3	Field content and gauge structure of the 3SHLM as a moose diagram [6]. The dashed lines depict the invariant terms of the Yukawa sector (cf. section 2.2), the dotted line hints at the non-trivial $U(1)_2$ charges carried by all fermion fields. . . .	39
4	Divergent high energy behavior of the partial wave coefficients corresponding to the lowest contributing angular momenta in the 3SHLM, for the three isospin channels $I = 0, 1, 2$ (from top to bottom). The functions $ a_L (\sqrt{s})$ are plotted on the left for different values of m' , where the limit $m' \rightarrow 0$ illustrates an upper limit for the possible cancellation in the 3SHLM and the limit $m' \rightarrow \infty$ corresponds to the SM result. The right side displays the corresponding functions $\sqrt{s}_c(m')$, with the red dashed lines illustrating the constraints m' , i. e. that it be heavier than 380 GeV (cf. section 2.3.2) but also lighter than its own unitarity-violating energy scale \sqrt{s}_c . The black dotted lines show the limits described above, i. e. the SM threshold as well as twice that value. Note that in the $I = 1$ channel the gauge boson resonance contributing to the lowest angular momentum $L = 1$ (center left) runs into the critical energy range above $m' \gtrsim 1.5$ TeV (center right).	53
5	New contribution to αT in the 3SHLM due to the heavy isospin-violating fermion doublet (T, B) coupling to the charged SM gauge bosons W^\pm . Double fermion lines and capital letters indicate heavy mass eigenstates.	56

6	Allowed range of values for the W' coupling to SM fermions according to the one-loop analysis in [43]. The values were normalized to the SM coupling of W to fermions and plotted in dependence on the heavy fermion mass scale M for different gauge boson masses m' ($\equiv M_{W'}$) of 380, 500 and 600 GeV. Λ denotes the momentum cutoff taken for the loop calculations.	58
7	Three-dimensional view of the ATLAS detector [4].	59
8	3D view of the inner detector [5].	61
9	3D view of the calorimeter system, including ECal (electromagnetic barrel and end-cap) and HCal (tile barrels and HEC) [5].	62
10	The ATLAS muon spectrometer [5].	63
11	Cross section of a single MDT drift tube (left, [4]) and of an entire MDT consisting of two multilayers enclosing a central support structure (right, [45]). Furthermore, the principle of track reconstruction based on the determination of minimal radii in several drift tubes is illustrated.	64
12	Dominating class of diagrams for the production and subsequent decay of the Z' (left) and the W' (right) at the LHC. For the resulting four-fermion state, the various possible detector signatures are listed, to be read in columns with each column denoting a separate final-state signature. The label j stands for quarks on parton level, which will hadronize to form physical hadron jets in the detector, and the label l denotes the light charged leptons e and μ , where the explicit distinction of anti-particles is suppressed in the notation.	66
13	$t\bar{t}$ production via gluon-gluon scattering, which is dominant ($\sim 90\%$) at the LHC [5], and subsequent semi-leptonic decay via W bosons.	70
14	Comparison of observables which depend on calorimeter data in fully simulated and ATLFAST-2 samples. The left side shows the deposition of transverse energy inside an angular cone of size $\Delta R = 0.2$ around the muons, while the missing transverse momentum is displayed on the right. The upper histogram shows absolute distributions (with ATLFAST-2 data normalized to full sim. data with fewer statistics) and the lower one shows the bin ratios. Generally, the results are in good agreement.	73

15	Comparison of kinematic distributions from SHERPA (black) and WHIZARD/PYTHIA (red): p_T of muons (top left) and jets (top right), η of muons (center left) and jets (center right), and the Z resonance in the di-muon mass (bottom left). The plot on the bottom right shows the event selection efficiencies for a varying p_T cut, normalized to the loosest cut $p_T > 15$ GeV.	77
16	Comparison of muon data on truth and reco level: Angular matching (top left, with the cone size for truth/reco matching indicated with a dashed blue line), normalized p_T difference of matching pairs (top right), η difference (center left), φ difference (center right), and η -resolved efficiency (bottom left), as well as the Z resonance in the $\mu\mu jj$ channel (bottom right).	79
17	Comparison of electron data on truth and reco level: Angular matching (top left, fake/efficiency cone in blue), normalized difference of p_T (top right), η (center left), φ (center right), as well as the η dependence of the efficiency (bottom left) and the Z resonance in the $eejj$ channel (bottom right).	82
18	Normalized W resonance in the invariant mass of two reconstructed jets, with different reconstruction setups: Seeded cone algorithm on LC topoclusters with varied parameter R (upper left), different jet algorithms with $R = 0.4$ on LC topoclusters (upper right) and seeded cone algorithm with $R = 0.4$ on different input data (below). The correct W mass is indicated with a dashed line in each case.	86
19	Essential quantities for the rejection of electrons in the hard jets: Enclosed angle of every hard jet and respective closest electron within one event (left) and the energy ratio of these pairs (right). The rejection cuts, eqn. (4.3), are marked with blue dashed lines.	87
20	The mass shell conditions of the neutrino and a W boson decaying leptonically, plotted in the plane of the two remaining unknowns, namely the energy and the longitudinal or z component of the neutrino 4-momentum [6]. The intersections of the two curves give rise to possible solutions for these quantities.	88
21	Enclosed angle between a di-jet resonance with an invariant mass inside the cut window of the SM gauge bosons and all reconstructed electrons in the same event, both on truth level and on reco level. The rejection cut for fake electrons in the vicinity of the jet resonances is indicated with the blue dashed line.	89

22	Distribution of the W mass, both on truth level and as computed from eqn. (4.11) using \cancel{E}_T on reco level as well as the true p_T on truth level as a consistency check, where the black dashed line indicates the mass cut applied on reco level.	90
23	Matching of true and reconstructed neutrino momenta: Comparison of the norm (top left) and direction (top right) of \cancel{E}_T with the true p_T , as well as the η matching of \pm neutrinos (bottom left, both solutions added) and c neutrinos (bottom right), where in each case the results are shown for both lepton flavors on reco level, and for η additionally on truth level using the true p_T of the neutrino and the true charged lepton as a cross-check.	92
24	Kinematic cuts (dashed blue lines) on the jet pairs in the $l\nu jj$ final state: The requirements are an invariant mass in the range of the SM gauge bosons (left, $m' = 500$ GeV) and a maximal value of the enclosed angle (right).	93
25	Invariant mass of the di-jet resonance, the charged lepton and one reconstructed neutrino momentum in the 100 fb^{-1} signal samples of the $l\nu jj$ channel with $m' = 380$ GeV (left) and 500 GeV (right). The two different neutrino reconstruction methods (\pm neutrinos summed up) are plotted separately in order to compare their signal performance.	95
26	Signal and all backgrounds covering 100 fb^{-1} in the $l\nu jj$ final state. The top row displays the signal sample for $m' = 500$ GeV with the requirement of at least (left) and exactly (right) two hadron jets per event on detector level. The bottom row shows $m' = 380$ (left) and 600 GeV (right) with exactly two jets per event. Note that $g_{W'ff}$ was generally set to its maximal value allowed in [43], but the pure Z' signal in ideal delocalization is also shown for $m' = 500$ GeV (top right). The significances s given in the plots are computed according to eqn. (4.16) inside mass intervals which were obtained from the optimization method explained in the text (given in numbers and indicated with the dashed lines). The dramatic significance drop for $m' = 600$ GeV stems from the finite angular resolution of jet pairs on detector level due to the splitting parameter of the jet algorithms (see text, cf. fig. 24 and section 4.1.3).	96
27	Gaussian fits on the W'/Z' resonance for different mass values $m' = 380, 500$ and 600 GeV in the $l\nu jj$ final state, with maximal W' coupling to SM fermions allowed by [43].	97

28	Dependence of the signal significance on the ΔR cut on jet pairs (left) and on the p_T cut (right) for different heavy gauge boson masses. The error bars refer to statistical uncertainties.	99
29	Invariant mass distribution of two jets emerging from the decay of SM gauge bosons (W left, Z right). The jets were reconstructed on reco level with the seeded cone algorithm ($R = 0.4$) on topoclusters, cf. section 4.1.3. The fit function is a convolution of the intrinsic Lorentzian with a Gaussian for experimental resolution.	101
30	Invariant mass distribution of the jet pairs in events contributing to the heavy gauge boson resonance with $m' = 500$ GeV.	103
31	Distribution of the enclosed angle of two muons for different values of m' with maximal $g_{W'ff}$ in the $lljj$ channel (left) and dependence of the signal significance on the applied ΔR cut for $m' = 500$ GeV (right, statistical uncertainty marked with error bars). For the other two values of m' the signal is not significant in this channel.	105
32	W' signal and background samples corresponding to 100 fb^{-1} in the $lljj$ channel with maximal $g_{W'ff}$, for heavy gauge boson masses $m' = 380$ GeV (top left), 500 GeV (top right) and 600 GeV (bottom). For $m' = 500$ GeV, which is the only sample to convey a significant signal, the vanishing of the W' signal in the ideally delocalized scenario is also shown.	106
33	W' signal and SM expectation in the $l\nu ll$ final state, for $m' = 380$ GeV (top left), 500 GeV (top right) and 600 GeV (bottom), in each case with maximal $g_{W'ff}$. The vanishing of the signal in ideal delocalization is also shown for $m' = 500$ GeV (top right).	108
34	Signal discovery thresholds in the $l\nu jj$ channel, for ideal delocalization, i. e. pure Z' signal (left) and maximal W' coupling to SM fermions (right), as extrapolated from 100 fb^{-1} of simulated data. The continuous lines indicate the significances computed from data in each case, whereas the dashed lines denote the lower significance limits with statistical and systematic uncertainties taken into account.	110
35	The 4-momentum flow convention and cyclic enumeration chosen for all $2 \rightarrow 2$ processes considered in the course of this thesis. The resulting momentum combinations for the Mandelstam variables are indicated in blue (s), green (t) and red (u).	123

36	Comparison of transverse momentum p_T (left) and the number per event (right) of reconstructed hard jets (cone algorithm with $R = 0.4$ on topoclusters, cf. section 4.1.3), from fully simulated and ATLFAST-2 calorimeter data, analog to the procedure of fig. 14 in section 3.2.3. Although the data seem to show some small systematic deviations, i. e. in ATLFAST-2 data p_T is slightly shifted to larger values and also the jet numbers are somewhat larger in average, the overall agreement is still solid enough to justify the usage of ATLFAST-2.	127
37	Comparison of the angular variables (η, φ) of reconstructed jets from fully simulated and ATLFAST-2 data, analog to the procedure in section 3.2.3. These distributions are in very good agreement.	128
38	Comparison of transverse momentum p_T (left) and the number per event (right) of reconstructed electrons from fully simulated and ATLFAST-2 calorimeter data, analog to fig. 36 for jets.	129
39	Comparison of the angular variables (η, φ) of reconstructed electrons from fully simulated and ATLFAST-2 data. While the distributions of the azimuth angle φ are non-surprisingly in good agreement, the pseudorapidity η is slightly but significantly shifted to larger transversality in the ATLFAST-2 sample.	130

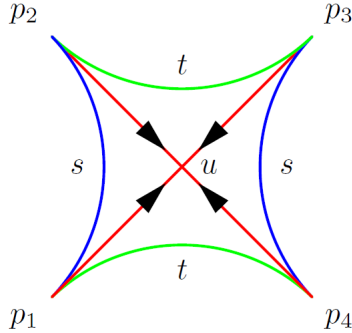


Figure 35: The 4-momentum flow convention and cyclic enumeration chosen for all $2 \rightarrow 2$ processes considered in the course of this thesis. The resulting momentum combinations for the Mandelstam variables are indicated in blue (s), green (t) and red (u).

Appendix

A 4-Momentum Conventions

In order to make all expressions occurring in $2 \rightarrow 2$ scattering which depend on the external 4-momenta—especially the Feynman amplitudes—as symmetric as possible, a symmetric 4-momentum flow convention is adopted with all momenta pointing inward (fig. 35), which imposes energy-momentum conservation in the form

$$p_1 + p_2 + p_3 + p_4 = 0 . \quad (\text{A.1})$$

Together with a charge-conjugation of the final state particles, this corresponds to swapping the entire final state into the initial state so that the resulting Feynman amplitudes describe an annihilation of four particles into the vacuum. Although essentially unphysical, the amplitude of such a process remains unchanged with respect to the original one due to crossing symmetries. The Mandelstam variables are then given by squaring all possible combinations of summing two of the four 4-momenta:

$$\begin{aligned} s &\equiv (p_1 + p_2)^2 = (p_3 + p_4)^2 \simeq 2p_{1(3)} \cdot p_{2(4)} , \\ t &\equiv (p_1 + p_4)^2 = (p_2 + p_3)^2 \simeq 2p_{1(2)} \cdot p_{4(3)} , \\ u &\equiv (p_1 + p_3)^2 = (p_2 + p_4)^2 \simeq 2p_{1(2)} \cdot p_{3(4)} . \end{aligned} \quad (\text{A.2})$$

Here t and u were defined in crossed order, so that the enumeration of external momenta in \mathcal{M} becomes cyclic (fig. 35). These definitions imply a relation

between the Mandelstam variables and the occurring masses m_i of all external particles involved:

$$s + t + u = \sum_{i=1}^4 m_i^2 \simeq 0, \quad (\text{A.3})$$

so that only two of the variables may be chosen independently. The approximations given in (A.2) and (A.3) are valid in a regime where $m_i \ll \sqrt{s}$. In this limit t and u can be expressed by s and the scattering angle θ only:

$$\begin{aligned} t &= \left(-\frac{s}{2} + \sum m_i^2 + \mathcal{O}\left(\frac{m_i^4}{s}\right) \right) (1 - \cos \theta) \simeq -\frac{s}{2} (1 - \cos \theta), \\ u &= \left(-\frac{s}{2} + \sum m_i^2 + \mathcal{O}\left(\frac{m_i^4}{s}\right) \right) (1 + \cos \theta) \simeq -\frac{s}{2} (1 + \cos \theta). \end{aligned} \quad (\text{A.4})$$

Note that in the special case of identical external masses m the terms of $\mathcal{O}(m_i^4/s)$ vanish and the left equal signs hold exactly without corrections, with $\sum m_i^2 \rightarrow 2m^2$.

B Contractions of Longitudinal Polarization Vectors

B.1 $W^{1/2}$ Scattering

As pointed out in section (1.1), the contractions of external longitudinal gauge bosons with each other or with external 4-momenta in $2 \rightarrow 2$ scattering amplitudes potentially deliver factors which violate partial-wave unitarity in the high-energy limit. In order to evaluate all kinematically different types of these contractions, and to express them in terms of the Mandelstam variables, an explicit choice of the four external 4-momenta defined in appendix A is made in the CMS frame:

$$\begin{aligned} -p_{1/2} &\equiv (E, \pm \vec{p}), \\ p_{3/4} &\equiv (E, \pm \vec{p}') \end{aligned} \quad (\text{B.1})$$

$$\text{with } |\vec{p}| = |\vec{p}'| \equiv p \quad \text{and} \quad \angle(\vec{p}, \vec{p}') = \theta,$$

where $p_i^2 = m^2 \forall i$, see below for external Z . The general result of contracting two longitudinal polarization vectors in the CMS is then given from eqn. (1.8):

$$\begin{aligned} \varepsilon_L(p_i) \cdot \varepsilon_L(p_j) &= \frac{p^2}{m} - \frac{E^2}{m} \cos \varphi \quad \text{with} \quad \varphi = \angle(\vec{p}_i, \vec{p}_j) \\ &= \frac{E^2}{m} (1 - \cos \varphi) - 1, \end{aligned} \quad (\text{B.2})$$

where the mass shell condition $p^2 = E^2 - m^2$ was used in the second line. Evaluation of this expression in the s channel, with $\varphi = \pi$ and $s = 4E^2$, gives

$$\varepsilon_L(p_{1(3)}) \cdot \varepsilon_L(p_{2(4)}) \equiv [\varepsilon_L \cdot \varepsilon_L]_s = \frac{s}{2m^2} - 1, \quad (\text{B.3})$$

whereas in the t channel, collecting a global sign from the definition (B.1) and setting $\varphi = \theta$, one arrives at

$$\begin{aligned} [\varepsilon_L \cdot \varepsilon_L]_t &= \frac{t}{2m^2} + \frac{t-u}{s-4m^2} \\ &= \frac{t}{2m^2} + \frac{t-u}{s} + \mathcal{O}(x^{-1}) \end{aligned} \quad (\text{B.4})$$

with the large parameter $x \equiv s/m^2$. The result for the u channel, $\varphi = \pi - \theta$, can be easily obtained from (B.4) using the crossing symmetry $t \leftrightarrow u$:

$$\begin{aligned} [\varepsilon_L \cdot \varepsilon_L]_u &= \frac{u}{2m^2} + \frac{u-t}{s-4m^2} \\ &= \frac{u}{2m^2} + \frac{u-t}{s} + \mathcal{O}(x^{-1}). \end{aligned} \quad (\text{B.5})$$

Note that the dimensionless quantities t/m^2 and u/m^2 merge two orders of x , cf. eqn. (A.4), therefore the exact relations for t and u have to be plugged into all terms of the x expansions in (B.4) and (B.5) except for the last one each.

Now the results of contracting a polarization vector with an external 4-momentum are given for each kinematic channel. The general result of such a contraction in the CMS is, from eqn. (1.8),

$$\begin{aligned} \varepsilon_L(p_i) \cdot \frac{p_j}{m} &= \frac{E p_j}{m^2} (1 - \cos \varphi) \\ &= \left(\frac{1}{4}x - \frac{1}{2} + \mathcal{O}(x^{-1})\right) (1 - \cos \varphi), \end{aligned} \quad (\text{B.6})$$

where the mass shell condition has been expanded in m/E ,

$$p = E\sqrt{1 - \frac{m^2}{E^2}} = E \left[1 - \frac{1}{2} \left(\frac{m}{E}\right)^2 - \frac{1}{8} \left(\frac{m}{E}\right)^4 + \mathcal{O}\left(\left(\frac{m}{E}\right)^6\right)\right], \quad (\text{B.7})$$

and plugged in to give the second line of (B.6). In the s channel, this leads to

$$[\varepsilon_L \cdot \frac{p}{m}]_s = \frac{s}{2m^2} - 1 + \mathcal{O}(x^{-1}), \quad (\text{B.8})$$

while inserting the 4-momenta corresponding to the t and u channels gives

$$[\varepsilon_L \cdot \frac{p}{m}]_t = \frac{t}{2m^2} + \frac{t}{s} + \mathcal{O}(x^{-1}) \quad (\text{B.9})$$

$$\text{and } [\varepsilon_L \cdot \frac{p}{m}]_u = \frac{u}{2m^2} + \frac{u}{s} + \mathcal{O}(x^{-1}). \quad (\text{B.10})$$

Note that the x expansions for the contractions of polarizations among each other, eqns. (B.3) – (B.5), differ from the contractions between polarizations and momenta just given in eqns. (B.8) – (B.10) only in the subleading order (for the s channel even in the sub-subleading order), as could be expected from eqn. (1.9). For completeness, and to make things easier in the course of section 1.3, the differences of these contractions are also given here for each kinematic channel:

$$[\varepsilon_L \cdot (\frac{p}{m} - \varepsilon_L)]_s = 0 + \mathcal{O}(x^{-1}), \quad (\text{B.11})$$

$$[\varepsilon_L \cdot (\frac{p}{m} - \varepsilon_L)]_t = \frac{u}{s} + \mathcal{O}(x^{-1}), \quad (\text{B.12})$$

$$[\varepsilon_L \cdot (\frac{p}{m} - \varepsilon_L)]_u = \frac{t}{s} + \mathcal{O}(x^{-1}). \quad (\text{B.13})$$

B.2 External Z^0 Bosons

As soon as external Z^0 occur in the asymptotic states, the results of the previous paragraph must be somewhat modified to account for the mass splitting between W^\pm and Z^0 . For scattering processes with altogether two Z and two W , which are the only possible ones on tree level, the various kinds of mixed Lorentz contractions of polarization vectors and 4-momenta with respect to external W and Z can be found easily using the proper mass shell conditions, $p_i(W)^2 = m^2$ and $p_i(Z)^2 = m_Z^2$, the definition of the longitudinal polarization vector, eqn. (1.8), and the mass-shell expansion, eqn. (B.7). The polarization contractions give:

$$[\varepsilon_L(W) \cdot \varepsilon_L(Z)]_s = \frac{s}{2mm_Z} - \alpha + \mathcal{O}(x^{-1}), \quad (\text{B.14})$$

$$[\varepsilon_L(W) \cdot \varepsilon_L(Z)]_t = \frac{t}{2mm_Z} + \frac{t-u}{s}\alpha + \mathcal{O}(x^{-1}) \quad (\text{B.15})$$

$$\text{with } \alpha \equiv \frac{m_Z^2 + m^2}{2mm_Z} = \frac{1}{2} \left(\cos \theta_\omega + \frac{1}{\cos \theta_\omega} \right),$$

and the usual exchange $t \leftrightarrow u$ for the u channel. The contractions of longitudinal polarizations and 4-momenta result in:

$$\left[\varepsilon_L(W) \cdot \frac{p(Z)}{m_Z} \right]_s = \left[\varepsilon_L(Z) \cdot \frac{p(W)}{m} \right]_s = \frac{s}{2mm_Z} - \alpha + \mathcal{O}(x^{-1}), \quad (\text{B.16})$$

$$\left[\varepsilon_L(W) \cdot \frac{p(Z)}{m_Z} \right]_t = \frac{t}{2mm_Z} + \frac{t}{s}\alpha + \frac{u}{s}\beta + \mathcal{O}(x^{-1}), \quad (\text{B.17})$$

$$\left[\varepsilon_L(Z) \cdot \frac{p(W)}{m} \right]_t = \frac{t}{2mm_Z} + \frac{t}{s}\alpha - \frac{u}{s}\beta + \mathcal{O}(x^{-1}), \quad (\text{B.18})$$

$$\text{with } \beta \equiv \frac{m_Z^2 - m^2}{2mm_Z} = \frac{1}{2} \sin \theta_\omega \tan \theta_\omega,$$

and $t \leftrightarrow u$ for the u channel.

C Comparison of ATLFAST-2 and Full Simulation

C.1 Jet Variables

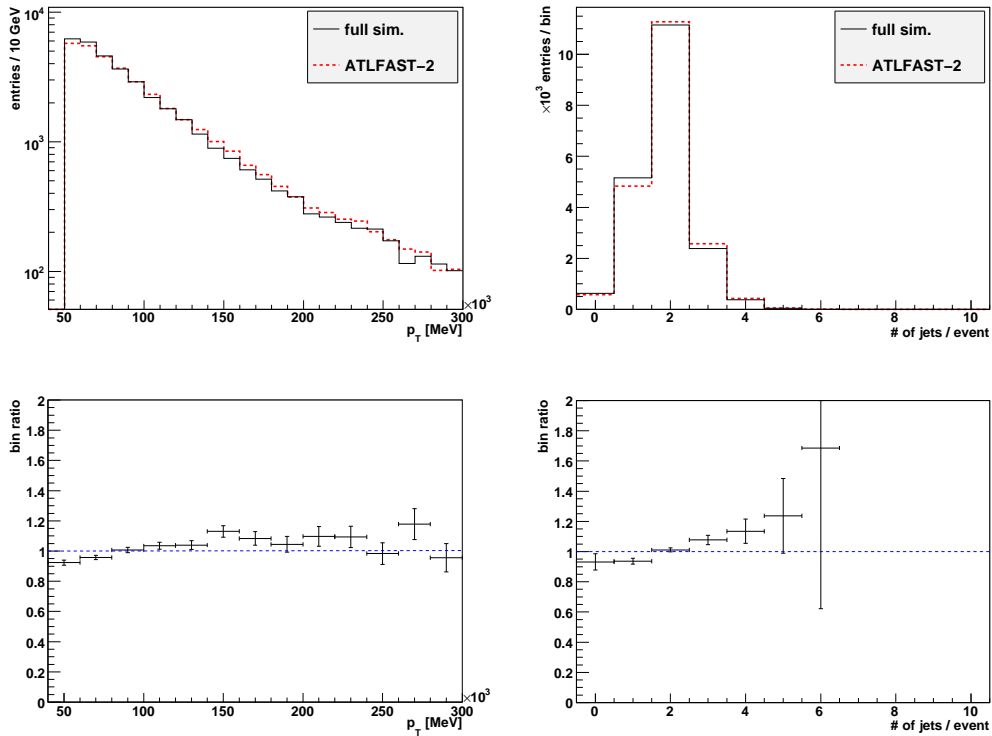


Figure 36: Comparison of transverse momentum p_T (left) and the number per event (right) of reconstructed hard jets (cone algorithm with $R = 0.4$ on topoclusters, cf. section 4.1.3), from fully simulated and ATLFAST-2 calorimeter data, analog to the procedure of fig. 14 in section 3.2.3. Although the data seem to show some small systematic deviations, i. e. in ATLFAST-2 data p_T is slightly shifted to larger values and also the jet numbers are somewhat larger in average, the overall agreement is still solid enough to justify the usage of ATLFAST-2.

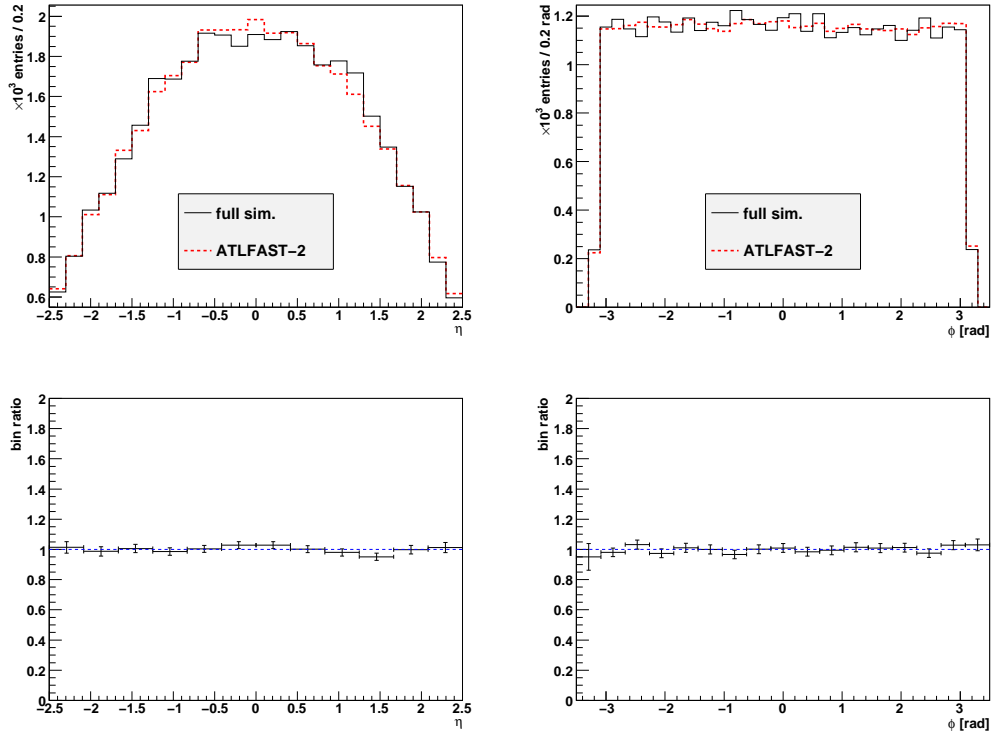


Figure 37: Comparison of the angular variables (η, φ) of reconstructed jets from fully simulated and ATLFAST-2 data, analog to the procedure in section 3.2.3. These distributions are in very good agreement.

C.2 Electron Variables

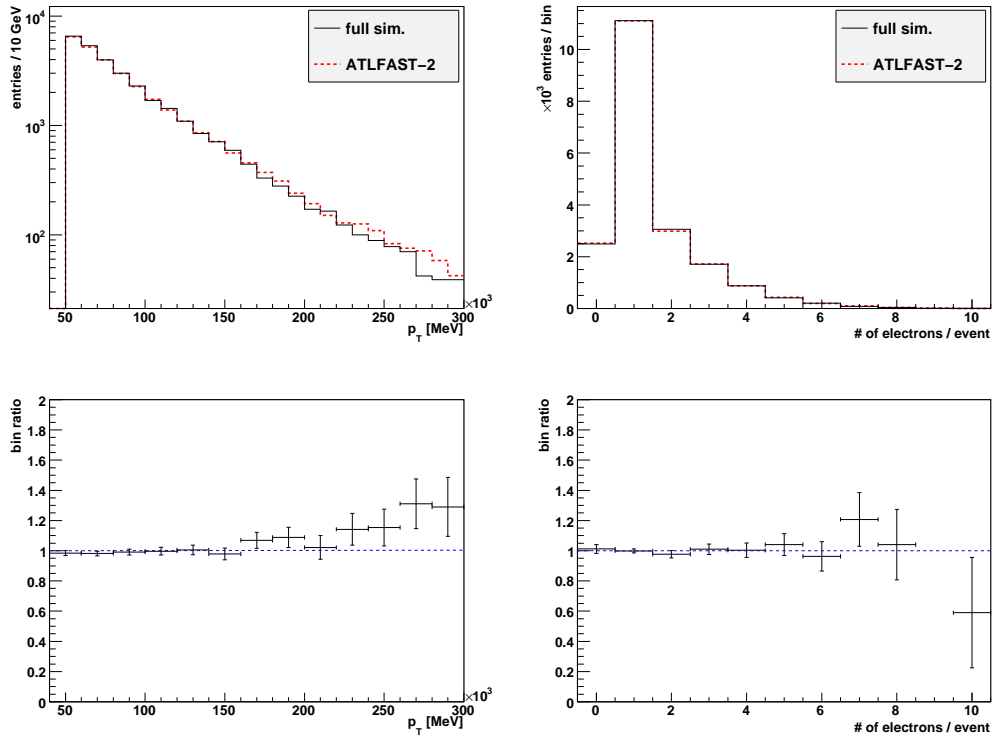


Figure 38: Comparison of transverse momentum p_T (left) and the number per event (right) of reconstructed electrons from fully simulated and ATLFAST-2 calorimeter data, analog to fig. 36 for jets.

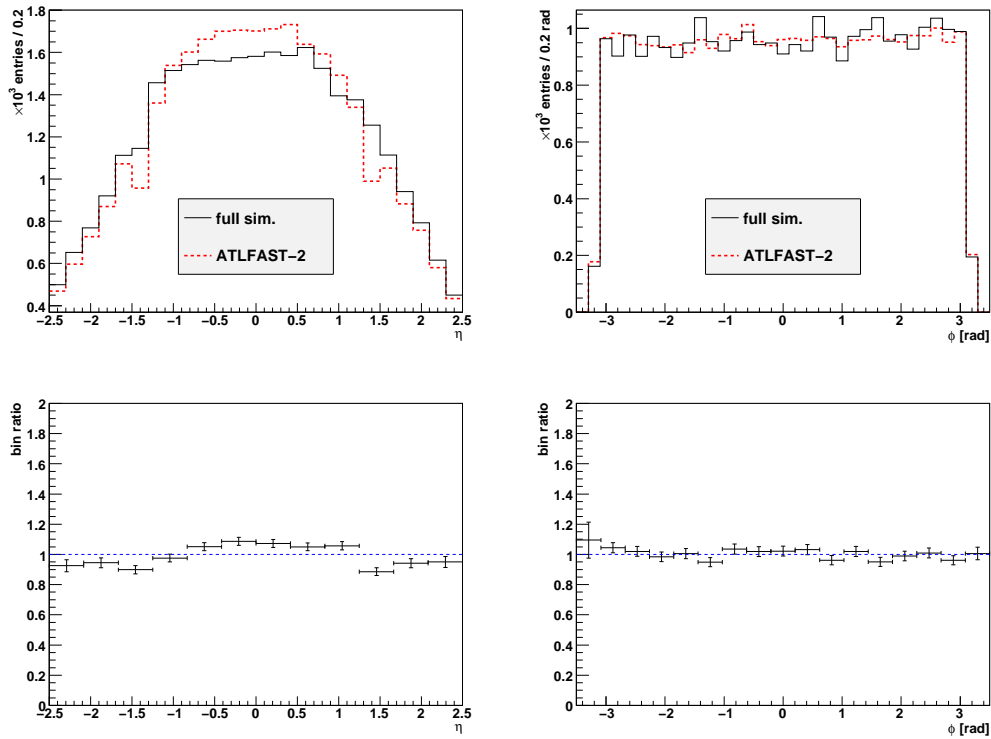


Figure 39: Comparison of the angular variables (η, φ) of reconstructed electrons from fully simulated and ATLFAST-2 data. While the distributions of the azimuth angle φ are non-surprisingly in good agreement, the pseudo-rapidity η is slightly but significantly shifted to larger transversality in the ATLFAST-2 sample.

Danksagung

An diesem Punkt verbleibt mir nur noch, einigen Menschen, ohne die ein erfolgreicher Abschluss der vorliegenden Arbeit sicherlich nicht möglich gewesen wäre, meinen aufrichtigen Dank auszudrücken: Zuallererst möchte ich meinen beiden Betreuern danken, Prof. Dr. Thorsten Ohl vom Lehrstuhl für Theoretische Physik II und Prof. Dr. Thomas Trefzger, Inhaber des Lehrstuhls für Physik und ihre Didaktik an der Universität Würzburg, die es mir ermöglicht haben in dieser Arbeit sowohl theoretische als auch experimentelle Aspekte auf dem Gebiet der Elementarteilchenphysik zu kombinieren, und mich während des vergangenen Jahres in zahllosen Fällen mit Fachgesprächen und Ratschlägen unterstützt haben. Außerdem sollen hier Christian Speckner und Dr. Andreas Redelbach dankbare Erwähnung finden, die auch in den meisten Fällen in die sich stets häufenden Fragen und Unklarheiten während meiner Arbeit involviert waren und nicht selten zu deren Lösung beigetragen haben. Schließlich möchte ich meinen Eltern, Ralf und Gundela Bach, sowie meiner Schwester Romy und meinen engen Freunden danken, die immer versucht haben mich zu motivieren und mir meine gerade während der letzten zwei Monate rar gesäte Freizeit so angenehm und erholsam zu gestalten wie ich sie auch empfunden habe.

Erklärung zur Anfertigung der Masterarbeit

Ich, Fabian Bach, erkläre hiermit, dass ich diese Masterarbeit in allen Teilen selbstständig angefertigt und nur die angegebenen Quellen und Hilfsmittel verwendet habe.

Würzburg, 16. Oktober 2009

Unterschrift